FACULDADE DE ENGENHARIA DA UNIVERSIDADE DO PORTO

# Experimental characterization of hybrid polymer gears

**João Miguel Antunes Pinto**

Mestrado Integrado em Engenharia Mecânica

Supervisor: Doutor Carlos M. C. G. Fernandes

Co-Supervisor: Doutor David Gonçalves

October 29, 2022

# Experimental characterization of hybrid polymer gears

**João Miguel Antunes Pinto**

Mestrado Integrado em Engenharia Mecânica

October 29, 2022

# Abstract

Over the years, polymer gears have increasingly become a subject of interest to the industry. The main reasons are related to the cheaper mass production and lower density than metallic gears, or even the dry running capability among other advantages. However, they have a major limitation related to their very low thermal conductivity and its mechanical properties are highly influenced by the operating temperatures. Therefore, in this dissertation, it will be developed a concept to improve the thermal behaviour of polymer gears, which are the hybrid polymer gears.

The objective is to experimentally test hybrid polymer gears, which are polymer gears with an impregnated insert in their matrix. The insert geometry chosen was based on previous studies already made on this topic. To perform the experimental tests, a heating and loading system was developed with the goal to emulate the operating conditions of the gears meshing. The final results analysis was focused on the thermal and thermo-mechanical behaviour of the specimen tested. So the thermal tests were prepared to measure the surface temperature using a thermal camera, and the thermo-mechanical tests were set to measure the surface displacements using a digital image correlation technique (DIC). Finite element method (FEM) models were developed to predict the hybrid polymer gears tests.

At the end, the experimental results were analysed and compared with FEM models. The final values showed that the hybrid polymer gear with aluminium insert improved the heat evacuation and the temperatures registered at the tooth meshing region were lower than the standard polymer specimen. Besides that, the displacements registered did not negatively impact the proper geometry of the specimen, and the FEM models were validated.

**Keywords**: Polymer Gears, Hybrid Polymer Gears, Thermal Model, Thermo-mechanicam model, DIC, Finite Element Method (FEM)

# Resumo

Ao longo dos anos, as engrenagens poliméricas tornaram-se cada vez mais um assunto de interesse para a indústria. Os principais motivos estão relacionados com a produção em massa mais barata e a densidade inferior comparativamente às engrenagens metálicas, ou ainda a capacidade de funcionamento sem lubrificação, entre outra vantagens. Contudo, têm uma grande limitação relacionada com a sua muito baixa condutividade térmica e as suas propriedades mecânicas são altamente influenciadas pelas temperaturas de funcionamento. Deste modo, nesta dissertação será estudado um conceito para melhorar o comportamento térmico das engrenagens poliméricas, que são as engrenagens poliméricas híbridas.

O objetivo é testar experimentalmente engrenagens poliméricas híbridas, que são engrenagens poliméricas com um inserto de alumíno impregnado na sua matriz, para o caso deste projeto. A geometria escolhida para o inserto foi baseada em estudos anteriores já realizados sobre este tópico. Para realizar os testes experimentais foi desenvolvido um sistema de aquecimento e de carga com o objectivo de simular as condições de engrenamento durante o período de operação das engrenagens. A análise dos resultados finais foi centrada no comportamento térmico e termo-mecânico do espécime testado. Assim, os ensaios térmicos foram preparados para medir a temperatura da superfície utilizando uma câmara térmica, e os ensaios termo-mecânicos foram definidos para medir os deslocamentos da superfície utilizando uma técnica de correlação digital de imagem (DIC). Os modelos utilizando o método dos elementos finitos (MEF) foram desenvolvidos para simular os testes de engrenagens híbridas de polímeros, quando as condições de aquecimento são as mais extremas registadas.

No final, os resultados experimentais foram analisados e comparados com os modelos MEF. Os valores finais mostraram que a engrenagem polimérica híbrida com inserto de alumínio melhorou a evacuação do calor e as temperaturas registadas na região de engrenamento eram inferiores às da engrenagem polimérica padrão. Além disso, os deslocamentos registados não tiveram um impacto negativo na geometria pretendida para o espécime, e os modelos MEF foram validados.

**Keywords**: Engrenagens Poliméricas, Engrenagens Poliméricas Híbridas, Modelo Térmico, Modelo Termo-mecânico, DIC, Método dos Elementos Finitos (MEF)

# Acknowledgements

I would like to start by thanking, both my supervisor Carlos Fernandes and my co-supervisor David Gonçalves, for all the advice, all their time spent with me and for their constant openness during the project.

Also, my sincere gratitude to all the staff working at CETRIB for their receptivity and help whenever needed.

Finally, to my family and friends, my thanks for all the support and for making me a happy and ambitious person. A special mention to my parents, brother, grandparents and my girlfriend. With them by my side is impossible to give up.

*“The greatest glory in living lies not in never falling, but in rising every time we fall.”*

Nelson Mandela

# Contents

# List of Figures

# List of Tables

# List of Symbols

| | | |
|---|---|---|
| $a$ | Hertzian semi-width of contact | mm |
| $\alpha$ | Thermal expansion coefficient | 1/°C |
| $\alpha_n$ | Gear pressure angle | ° |
| $a_c$ | Center distance | mm |
| $b$ | Gear face width | mm |
| $E$ | Elastic Young's Modulus | GPa |
| $E^*$ | Equivalent Elastic Young's Modulus | GPa |
| $\varepsilon$ | Emissivity coefficient | |
| $F_n$ | Normal force | N |
| $F_r$ | Radial force | N |
| $F_t$ | Tangential force | N |
| $g$ | Gravity acceleration | m/s$^2$ |
| $h_{aP}$ | Gear addendum coefficient | |
| $h_{fP}$ | Gear deddendum coefficient | |
| $h_{rack}$ | Total height of the rack | mm |
| $h_{rack,b}$ | Rack body height | mm |
| $h_s$ | Heat transfer coefficient | W/(m$^2$· K) |
| $\kappa$ | Thermal conductivity | W/(m· K) |
| $L$ | Horizontal length of the T plate profile | mm |
| $l_{insert}$ | Insert length | mm |
| $l_{rack}$ | Rack length | mm |
| $m$ | Module | mm |
| $m_{total}$ | Theoretical total mass applied in the tooth flank | kg |
| $m_w$ | Theoretical mass of the weights | kg |
| $m_{w,a}$ | Measured mass of the weights | kg |
| $\overline{Nu}_L$ | Nusselt number | |
| $\nu$ | Poisson's ratio | |
| $\nu_1$ | Aluminium Poisson's ratio | |
| $\nu_2$ | POM Poisson's ratio | |
| $p$ | Gear pitch | mm |
| $Pr$ | Prandtl number | |
| $\rho$ | Density | kg/m$^3$ |
| $\rho^*$ | Equivalent curvature radius | mm |
| $\rho_1$ | Curvature radius of the load and heat application tool | mm |
| $\rho_2$ | Curvature radius of the tooth flank | mm |
| $\rho_r$ | Root radius coefficient | mm |
| $Ra_L$ | Rayleigh number | |

| | | |
|---|---|---|
| $r_d$ | Pinion root radius | mm |
| $r_f$ | Gear fillet radius | mm |
| $r_{shaft}$ | Shaft radius | mm |
| $\sigma$ | Stefan Boltzmann constant | |
| $\sigma_b$ | Tooth root bending stress | MPa |
| $\sigma_f$ | Tooth root bending stress with ISO 6336-3 | MPa |
| $\sigma_{f,FEM}$ | Tooth root bending stress using FEM software | MPa |
| $\sigma_H$ | Hertzian contact pressure | MPa |
| $\sigma_r$ | Radial stress | MPa |
| $s_b$ | Tooth base thickness | |
| $T_b$ | Temperature of the rack bottom surface | °C |
| $T_f$ | Melt temperature | °C |
| $T_{fc}$ | Contact temperature | °C |
| $T_{Heater}$ | Temperature of the cartridge heater | °C |
| $T_{ss}$ | Temperature of the supported side of the tooth rack | °C |
| $T_{t1}$ | Temperature of the tooth rack surface close to the heater | °C |
| $t$ | Length from the tooth tip to the insert | |
| $w$ | Insert width | mm |
| $x_1$ | Profile shift coefficient of the pinion | |
| $x_2$ | Profile shift coefficient of the wheel | |
| $Y_F$ | Form factor | |
| $z_1$ | Number of teeth of the pinion | |

# Abbreviations

| | |
|---|---|
| APS | Aminopropyltrimethoxysilane |
| CAD | Computer-Aided Design |
| DIC | Digital Image Correlation |
| FEM | Finite Element Model |
| HDPE | High-density polyethylene |
| HT | Hybrid tooth rack |
| PA | Polyamide |
| PBT | Polybutylene terephthalate |
| PDMS | Polydimethylsiloxane |
| PEEK | Polyether ether ketone |
| PET | Polyethylene terephthalate |
| PGMA | Polyglycidyl methacrylate |
| PI | Polyimide |
| PMMA | Polymethyl methacrylate |
| POM | Polyacetal |
| STD | Standard tooth rack |

# Chapter 1

# Introduction

## 1.1 Thesis Purpose

Polymer gears have been under several studies for the past decades since they have interesting advantages over metallic ones. Some of those advantages which attract the attention of the industry are the lower density, the dry running capability and the cheaper manufacturing cost when mass production is applied. However, important limitations are associated to these gears as its mechanical properties are significantly influenced by the operating temperatures and they have low thermal conductivity.

Given its potential, the studies around them are now focused to decrease the impact of the disadvantages mentioned before. Different approaches were tried with final improvements in wear, friction and thermal behaviour. Some of those methods consisted of modifying the tooth geometry, drilling cooling holes or even a hybrid polymer gear concept.

The hybrid polymer gear concept consists of improving the heat conduction by using metallic inserts impregnated in the polymer matrix, or any other material with adequate mechanical properties and a good thermal conductivity. Recent studies were performed on this topic [1, 2] and experimental validation was obtained [2].

In the present work, the main purpose is to experimentally validate the hybrid gear concept, but this time trying to approximate even more the experiment conditions to what happens during the gear meshing. In order to accomplish that, a new heating system will be designed and manufactured to test the hybrid gears. The temperature and displacement data will be collected to analyse the thermo-mechanical results. Also a FEM model was developed according to the conditions of the experiments. At the end, the impact of the hybrid tooth will be presented and the FEM model will be validated.

## 1.2 Thesis Outline

Chapter 2, entitled **Literature Review on Polymer Gears** addresses several polymer gear details. It goes since the polymer materials applied to gears, going through the manufacturing processes, advantages, disadvantages and presenting the most common failure modes. Also, previous studies are presented, and based on them, the definition of the hybrid polymer gear used in this project.

Chapter 3, called **Design and Manufacturing of a Gear Tooth Heating and Loading System**, describes the heating system purposes and design.

Chapter 4, named **Thermal and Thermo-Mechanical Finite Element Models**, covers the development of the FEM model of the hybrid gear tooth and goes from the mesh generation to the definition of the conditions simulated.

Chapter 5, denominated **Experimental Procedure**, addresses the variables definition, as well as the objectives and methods to proceed with the thermal and DIC experiments.

Chapter 6, entitled **Experimental and Numerical Results**, both the thermal and DIC experimental results are presented and analysed. Then, the FEM model validation is covered according to those results.

Chapter 7, named **Conclusions and Future Work**, describes the final conclusions of the dissertation and suggests future works.

# Chapter 2

# Literature Review on Polymer Gears

## 2.1 Introduction

Polymer gears have been increasingly introduced during the past years, in engineering applications due to their potential technical and economic advantages over metallic gears. The immediate advantages polymer gears present are the cheaper mass production, they are much lighter comparing with the steel ones and can operate without lubrication, which makes them appealing for the industries which need non lubricated applications, such as the food industry [3, 4, 5].

However, there is a critical drawback of polymer materials, which is their low thermal conductivity and the strong dependence of their mechanical properties on operating temperature. These parameters limit the applications to a low maximum running temperature and a low load transmission [3, 5].

During this first chapter, all the main topics related to polymer gears are presented, starting with the most typical polymer materials used in gears and their manufacturing processes. Next, addressing the advantages and disadvantages of polymer gears over metallic ones. Finally, the failure mechanisms and methods to improve these types of gears performance will also be introduced.

## 2.2 Polymer Materials Applied to Gears

The combination of polymers with other materials has been in continuous development with great advances achieved each year. Regarding the tribological behaviour of polymer composites, it depends on the chain structure of macromolecules of the polymeric matrix and the effect of fillers [6].

Polymer materials are also used as coatings applied to a variety of surfaces having a great impact in their properties. With a very proper and unique architecture, polymer layer molecules are able to modify interfaces at the nanolevel. This straight interaction between the coating and the surface modifies physical, chemical, mechanical, and tribological properties of the surfaces. Surface energy, corrosion, friction, wear and adhesion are only examples of properties directly influenced by the polymer coatings. In Table 2.1 are presented tribological properties of some thin polymeric coatings [6].

Table 2.1: Tribological properties for some thin polymeric coatings [6].

| Coating material | Thickness, nm | Testing equipment and test conditions | Coefficient of friction | Wear life, cycles |
|---|---|---|---|---|
| Polydimethylsiloxane (PDMS) | 180 | Ball-on-plate tribometer, steel ball, 0.5 N, 30–100 mm/min | <0.1 | $\leq$1200 |
| Aminopropyltrimethoxysilane (APS)/ poly(glycidyl methacrylate) (PGMA)/polyimide (PI) | 50-80 | Ball-on-disk tribometer, steel ball, 0.5 N, 20 mm/s | 0.08 | >25000 |
| Polyimide (PI) | 20 | Reciprocating abrasion test apparatus, sapphire slider of 40 mm diam, 0.49 N, 80 mm/s | 0.21 | $\leq$6500 |
| Polymethyl methacrylate(PMMA)/ $SiO_2/TiO_2$ | $\sim$120 | Ball-on-disk tribometer, GCr15 steel ball of 3mm diam, 3 N, 1.5 mm/s | 0.09-0.11 | >8000 |

Focusing on the gears topic, it is of interest to take a closer look to the polymer materials that are used nowadays for plastic gears. The most common polymers used for gears are polybutylene terephthalate (PBT), polyamides (PA46, PA66, PA12, and PA6), polyoxymethylene (POM), polyethylene terephthalate (PET), and high-density polyethylene (HDPE). There are also some high-performance, heat resistant and high temperature stable materials such as polyether ether ketone (PEEK), and polyimides (PI) [6, 7]. Among these polymers, the most frequently used in gears are PA and POM. Mechanical and thermal properties for some of the thermoplastics mentioned before are shown in Table 2.2. It is important to mention that the mechanical properties of plastics suffer significant changes with the operating conditions, such as temperature variation. A temperature rise causes a faster reduction in stiffness than what happens for the common metallic gear materials. For this reason, comparing different polymer gear materials requires common standard regarding the test conditions and test specimens selected. That also explains the fact that mechanical properties are presented for a very specific temperature for all the polymer materials exposed. All the properties were obtained from VDI 2736 Part 1 [8]. In Figure 2.1, a representation of wear and friction coefficients for different pairing polymer materials is shown, while keeping other conditions unchanged.

Table 2.2: Most important mechanical an thermal properties of polymer gear materials [8].

| | PA 6 | PA 12 | PA 46 | PA 66 | POM | PEEK |
|---|---|---|---|---|---|---|
| Young's Modulus, E / GPa, at 23 °C | 2.8 | 1.1 | 3.3 | 3.0 | 2.6-3.2 | 3.5-3.7 |
| Poisson's ratio, $\nu$, at 23 °C | 0.38-0.42 | 0.38-0.42 | 0.37 | 0.38-0.42 | 0.42-0.45 | 0.4 |
| Density, $\rho$ / kg·m$^{-3}$ | 1120-1150 | 1010 | 1180-1210 | 1130-1160 | 1390-1430 | 1260-1300 |
| Thermal conductivity, $\kappa$ / W·m$^{-1}$·K$^{-1}$ | 0.29 | 0.23 | - | 0.23 | 0.25-0.3 | 0.29 |
| Working thermal limits, short term, | 140-160 | 140 | 180 | 140-170 | 110-140 | 300 |
| Working thermal limits, continuous, °C | 80-100 | 70-80 | 140 | 80-100 | 90-100 | 250 |
| Price range, € / kg | 2.6-3.1 | 8-12 | 7-12 | 3.1-3.6 | 1.8-3.0 | 80-100 |

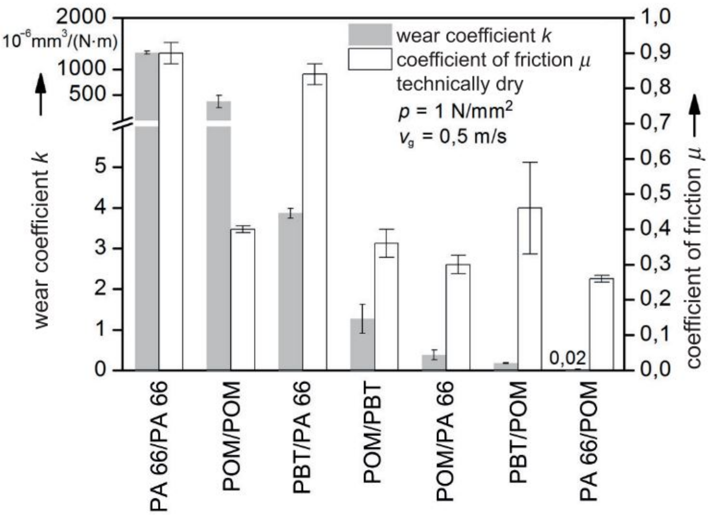

Figure 2.1: Wear coefficients and coefficients of friction for different pairing polymers [8].

As mentioned at the beginning of this section, fillers and reinforcing materials are an option for the function of polymer materials, and they can also be applied in polymer gears themselves. They are used to improve some properties, although they can also have a negative impact in others. The influence of some fillers and reinforcing materials in tribological, mechanical, and thermal properties is presented in Table 2.3.

Table 2.3: Influence of using filler and reinforcing materials in polymer gears[8].

| **Filler or reinforcing material** | **Positive influence** | **Negative influence** |
|---|---|---|
| glass, carbon or aramid fibres | increase in stiffness, tensile strength, flexural fatigue strength and heat distortion resistance | reduction in impact strength |
| PTFE | reduction in friction and wear | reduction in impact strength and flexural fatigue strength |
| PE | reduction in friction | reduction in impact strength |
| graphite, boron nitride | reduction in friction and wear,<br>increase in thermal conductivity | reduction in impact strength |
| silicone oil | reduction in friction and wear,<br>increase in toughness | - |
| mineral fillers | increase in heat distortion resistance | - |

## 2.3 Manufacturing Processes

Polymer gears can be manufactured by three methods, injection moulding, casting and machining. The choice between one of them requires to know the gear material, the surface quality needed, the quantity, form and size of the gear wheels [8].

Starting with injection moulding, it is the most common method and the typical one used in thermoplastic gear wheels. It consists of melting thermoplastic pellets and injecting them at high pressure into a mould. There the melt solidifies and gets the mould shape. The main advantages are the capability to manufacture different and complex geometries, as well as to do it in a very economic way, as long as the production quantities are high enough. When the surface quality needs to be more precise, a secondary finishing by machining may be necessary, being a disadvantage of this method [8].

Casting is mostly used for gears with large dimensions and weighing at least 1 kg. The mould material depends on the production quantities, being made of plastic or sand for lower quantities, and made of metal for larger scale productions. Usually, the final tooth shape is finished by machining because of the moulding shrinkage effect. However, centrifugal casting reduces this problem giving a better mould filling and allowing to avoid the final machining. This last method is only better to apply than pressureless casting for larger production quantities due to the manufacturing cost [8].

Machining is a third method that frequently comes along with the other methods mentioned before. When applied alone should be used to a maximum of medium scale production, given the lower tooling costs than in injection moulding. To produce polymer gears the method is the same as for metal ones. In this case, it is common to use a single cutting operation due to the low forces in the cutting tool [8].

## 2.4 Advantages and Disadvantages

It was already mentioned at the introduction of this chapter that polymer gears have important advantages over metallic gears, but also some considerable limitations.

In the next list, the advantages which explain why this type of gears is being more explored over the years are presented [5, 7]:

- Dry running capability;
- Lower weight and inertia;
- Improved noise levels in operation, since they have higher internal damping capacity and high resilience;
- Economic manufacturing processes, especially for mass production and capability to manufacture complex geometries (revisit section 2.3);
- Lower friction and superior resistance to corrosion.

On the other hand, the next list follow the topics that show why polymers gears are still not convincing to replace the majority of the functions of metallic gears [3, 5, 9]:

- Low thermal conductivity;
- Mechanical properties are significantly influenced by the operating temperatures;

- Polymer gears meshing has an extension of the contact between the teeth outside the line of action. This happens since plastics have an elastic modulus approximately one hundred times lower than those of most steels;
- Dimensional instability.

## 2.5 Gear Failures Mechanisms

When operating, gears are subjected to wear and damage conditions which may lead to gear failure mechanisms, if not controlled or predicted. Regarding polymer gears, the failure modes are more varied and there are some different ones, comparing to metal gears. This is a reason why it keeps being difficult to build a prediction model for each one these limiting situations [5, 8].

The gears conditions of use must be well defined, since for a certain material-specific load, material melting can start to occur, especially when operating under dry-running conditions. The poor heating conduction properties and low temperature limits make temperature being frequently related as the main reason of failures [8, 9].

### 2.5.1 Failure Modes

The most common polymer gears failure mechanisms are the gear tooth wear, severe shape deformation, tooth root cracking and tooth flank fracture, which are represented in Figure 2.2, for polymer cylindrical gears [8, 9].

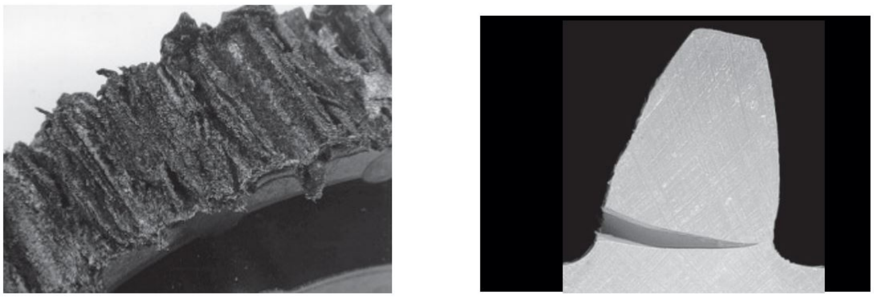

(a) Melting (b) Tooth Root Fracture

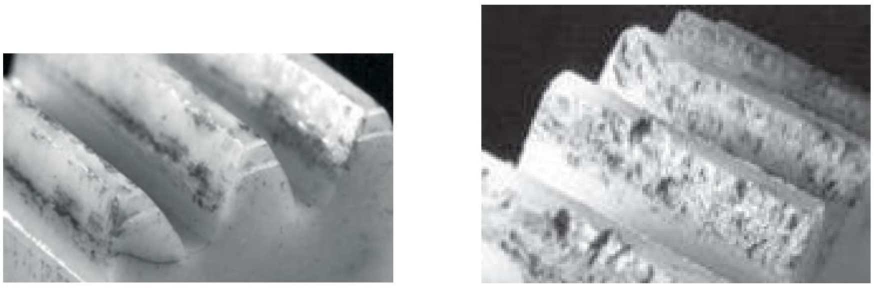

(c) Tooth Flank Fracture (d) Pitting

(e) Tooth Wear (f) Deformation

Figure 2.2: Polymer gear failure mechanisms [8].

The melting problem (Figure 2.2a) happens once the melting temperatures are reached, leading to irreversible tooth geometry changes [5, 8].

As it is shown in Figures 2.2b and 2.2c, fracture mostly occurs at the tooth root and pitch. For the first case, the cause is the excessive bending stress, while for the second case the same effect together with shear stress and excessive Hertzian stress are responsible for the pitch fracture. Cracks can appear from the active flank and outside face of the same flank, and grow until the fracture phenomena occurs. Reinforcing the polymer gear tooth using fibre direction parallel to the tooth surface can delay the fracture problem [5, 8].

The pitting causes are similar to the fracture ones, happening with excessive Hertzian stress together with shear and bending stresses at the same time. Close micro cracks appear and propagate until they meet at a certain point, promoting the fracture and material removal, as seen in Figure 2.2d. In order to avoid pitting, it is recommended to control the pressure variations along the tooth, using face width changes from the root to the tip [5, 8]. Both tooth fractures and pitting frequently occur when operating with external lubrication [8].

The tooth wear shown in Figure 2.2e, consists of layers of material removal. It mainly results from the applied force and relative sliding speed, which are usually promoted by the intense abrasive action of the frictional partner or by the poor wear resistance from the own polymer material. A way to control this phenomena is by fibre reinforcing the polymer gear [5, 8, 9].

Finally, deformation comes from the excessive surface stress when it reaches the deformation limits, causing unchangeable involute profile distortions, including the pressure angle variation, Figure 2.2f. To avoid deformations, flexurally rigid and hard materials are recommended, such as again the fibre-reinforced materials [8, 9].

### 2.5.2 Temperature Influence on Operating Conditions

It is essential to understand the influence of temperature in the behaviour of polymer gears in order to minimize its impact during the service. The temperature field of meshing gears can be separated in two fundamental parts: the bulk temperature and the transient temperature of gear surface, also known as flash temperature. Both temperature parameters are indispensable for polymers selection as their load-carrying capacity are much lower than the ones allowed for steel and are strongly dependent on the operating conditions [3]. The heat generation essentially comes from the friction between meshing gear teeth. As previously mentioned, polymers have low critical temperatures for material state transitions and once these limits are reached, tooth shapes deform and suffer irreversible changes in the initial operating geometry [5].

Nevertheless, temperature can lead to failure modes indirectly, since its increase tends to worsen polymer's mechanical and tribological properties, such as stiffness. The tooth loss of mechanical properties under the effect of heat hysterisis and friction causes temperature distribution with spikes in specific regions. The pitch point temperature tends to be higher where rolling contact occurs, while the tip and root of the tooth, where maximum sliding occurs, can release the heat faster and do not reach as higher values. The contact together with the low thermal conductivity promote this thermal degradation, a gear failure exclusive from polymer gears [9, 10].

### 2.5.3 Tooth Deflection

Tooth deflection happens when a load is applied on polymer gears during its operation time, where the tooth deflects a certain distance. This deflection disappears once the load is removed. However, when operating under large loads for a long time, plastic deformation occurs and so the tooth does not recover the initial position.

Deflection is mainly related with the material stiffness and applied loads, so with lower material stiffness, comes higher tooth deflections. For those reasons, tooth deflections are smaller in metallic gears and become very relevant for polymer gears, which deform severely [9]. It is of interest to compare different polymer materials, so in Figure 2.3 are presented PA and POM deflection curves. POM has a slightly lower rigidity than PA, so when the load is applied, POM undergoes greater deflections. Although, it only happens at the initial instants, because POM has lower fluidity index than PA, which allows POM to exhibit smaller tooth deflections in the subsequent instants, and also to reach the unloaded position faster [10].

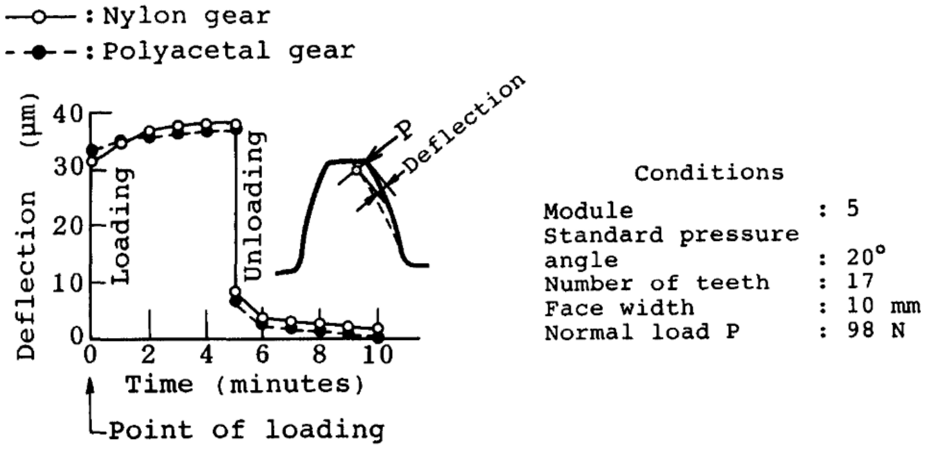

Figure 2.3: PA and POM deflection behaviour [10].

### 2.5.4 Wear on Plastic Gears

Wear mechanism consists of material removal on tooth surface and can be evaluated by the wear rate, which corresponds to the amount of the tooth thickness reduction per rolling cycle [5].

Wear is very influenced by the combination of materials used for the pinion and wheel and so, Mao *et al.* [11] tested combinations using POM, PA and steel gears. Spur gears were tested and their specifications are presented in Table 2.4.

Table 2.4: Specifications of the spur gears tested by Mao *et al.* [11].

| Property | Spur Gears |
|---|---|
| Module | 2 mm |
| Number of teeth | 30 |
| Pressure angle | 20 ° |
| Face width | 17 mm |
| Nominal backlash | 0.18 mm |
| Tooth thickness | 3.14 mm |
| Contact ratio | 1.65 |

The results shown that for POM/POM and PA/PA, the wear behaviour could be divided into three phases, a "running-in", a "nearly linear" and a "final fracture" phases. For POM/POM case, this division was more noticeable for medium loads (torques between 8.5 and 9 Nm), while for PA/PA at high loading conditions (torques above 10 Nm), both cases using running speeds of 1000 rpm. The first "running-in" phase covers a high amount of wear during a short period of time. Next, in the "nearly linear" phase, wear progressively increases with a linear behaviour and with a low wear rate, by comparison with the previous stage. Finally, in the "final fracture" phase, wear rapidly increases until failure occurs.

During the same work, polyacetal against nylon was also tested and the wear performance results were very different from PA/PA and POM/POM tests. When nylon was used as the driver, the polyacetal gear failed due to the thermal wear, similar to what happened in the POM/POM case. However, when polyacetal was used as the driver, the best wear performance was achieved, comparing with the previous combinations, with a significant increase. Mao *et al.* [11] testing, proved wear to not only be very dependent on the material combination, but also on the drive/-driven combination.

## 2.6 Methods to Improve Polymer Gears Performance

Polymer gears performance and durability are very important topics, mainly when focusing on polymer gears disadvantages which lead to the previously mentioned failure mechanisms. To not only avoid these problems, but also improve the most critical aspect, i.e, the thermal behaviour, three methods will be shown next. The first one presents gear geometry modifications, the second one uses cooling holes, and the last one are the hybrid polymers gears, where inserts will be employed.

### 2.6.1 Gear Tooth Geometry Modification

This first method consists of modifying the polymer gear tooth geometry. In order to do that, Imrek [12] studied the effects of the tooth width modification, by performing tests on three different types of gears: two gears made of Nylon 6, where one of them had a modified tooth width, while the other was unmodified, and another AISI 1045 steel alloy unmodified gear. The modified gear tooth geometry is shown in Figure 2.4 [12].

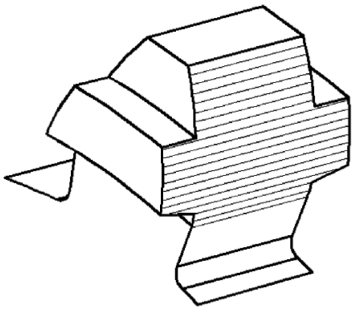

Figure 2.4: Modified gear tooth geometry [12].

Ideally, for gears to be continuously in mesh, two teeth pairs should be in contact simultaneously, allowing the tooth load to be shared among the two contact pairs. However, alternate double tooth and single tooth contacts are what happen in the real cases. In Figure 2.5a, the tooth contact areas are represented, and in Figure 2.5b the load distribution and sliding velocity distribution along the path of contact. It is of interest to notice that there are studies which explain that tooth load do not change instantaneously, as Figure 2.5b disregards the gear tooth elastic effects, but depending on the gear material, this change can be approximated as linear [12]. In order to maintain a constant load sharing ratio, Imrek increased the tooth width in the single tooth contact zone.

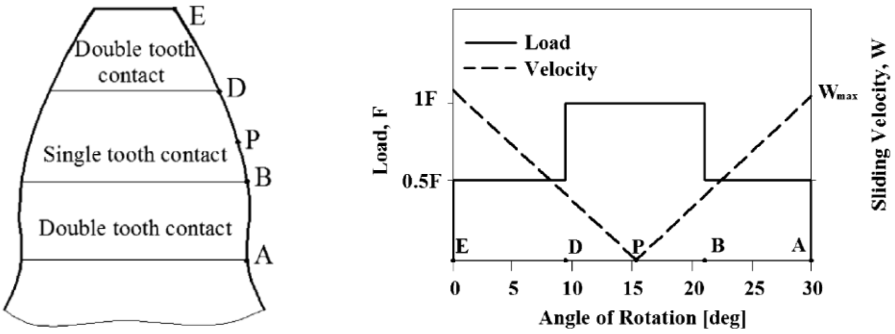

(a) Tooth contact areas (b) Load and sliding velocity distributions

Figure 2.5: Load and sliding behaviour during gear meshing [12].

The author had also performed fatigue testing of the gear pairs on the FZG test machine. The results showed that the average surface temperatures of unmodified gears are higher than in the modified ones. For the different Nylon 6 gears, the modified gear was able to reach surface temperatures 10 °C to 15 °C lower than the unmodified one. Regarding wear and performance, the tooth width modification proved to decrease the wear rates on the tooth profiles. Imrek [12] concluded that the increase of the heat dissipation and the smaller heat generation using modified gears, promoted the extension of the life performance of the gears, as well as prevented premature failures.

### 2.6.2 Drilling of cooling holes

In this method, the goal is to decrease the thermal damage by drilling cooling holes in the gear tooth. For that purpose, a configuration with a hole located at a specific radial position and two other holes along the radial direction of the tooth body was used, and represented in Figure 2.6 [13].

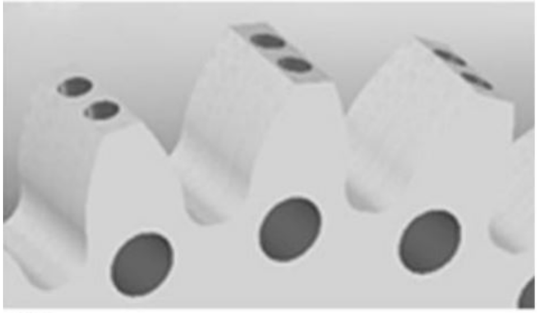

Figure 2.6: Cooling holes configuration [13].

Polymer gears were tested on an FZG machine and the results showed that this tooth configuration resulted in less thermal damage than in the standard gear tooth. It was proved that cooling holes allowed a better heat transfer, lowering the tooth body temperature. However for higher tooth loads the pitch region of some gear teeth started to suffer thermal damage [13].

### 2.6.3 Hybrid Polymer Gears

The hybrid polymer gear concept improves the heat conduction by using metallic inserts impregnated in the polymer matrix, or any other candidate material with good thermal conductivity and adequate mechanical properties [4]. Several studies have been performed in the past years, regarding the hybrid gears concept and recent research will be presented in more detail in the next chapters. This section will introduce the concept of hybrid polymer gears, as well as some solutions proposed by other authors.

Fernandes *et al.* [4] implemented a numerical model that allowed to study the influence of materials and insert geometry on a gear contact. The authors started by studying the influence of inserts in a polymer gear, where the POM was used as the polymer material and three different insert materials were tested, to conclude which one of them would be the most advantageous to use. Aluminium, copper and steel inserts were tested. At the beginning of the work, a simple insert in the shape of a rectangular block in the middle of the teeth (Figure 2.7) was applied, and the influence of the material on the tooth mass, and the influence of the contact pressure between polymer and metallic insert were under analysis. Regarding the insert material, the aluminium insert was the one which presented the best compromise between mass, heat conduction, manufacturing possibilities and cost. Even though the copper insert reached a lower maximum temperature than aluminium, the values are quite close and aluminium has the advantage of reducing the mass increment. The conclusions about contact pressure were translated to a higher heat flux with increased interface pressure, so the maximum temperature decreased. However, for contact pressures above 10 MPa, the heat transfer coefficient did not change significantly the maximum and minimum temperatures and so the authors decided to focus on the influence of the insert geometry instead [4].

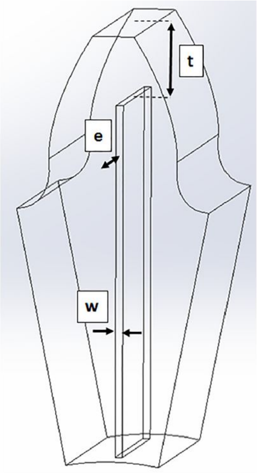

Figure 2.7: POM gear tooth with a rectangular block shape insert [4].

After Fernandes *et al.* [4] concluded that an aluminium insert was the most adequate for further testing, four different new insert designs were compared and represented here in Figure 2.8. The geometrical dimensions were optimized and the the influence on tooth temperature was studied. The results showed double T-profile (c) and involute profile (d) to have the best maximum temperature reduction, around 28 % comparing to the standard POM gear. However, both profiles also had the highest increase in the minimum temperature. For the T-profile (b) and plate profile (a), the maximum temperature reduction was 17 % and 11 %, respectively. The involute profile (d) was the best solution because it reaches the closest location to the path of contact allowing the most efficient heating evacuation among the four geometries. At the end, all the different inserts were able to reduce the maximum temperature, but all of them increased the minimum temperature as well. The final conclusions linked the direct impact of the contact area between the polymer and the insert and the position of the insert with the heat evacuation capacity. No correlation between mass and maximum operating temperature was found [4].

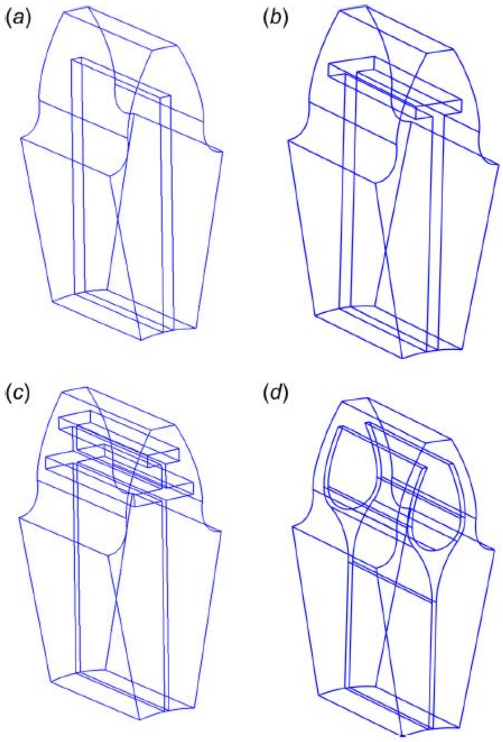

Figure 2.8: Four different insert geometries: (a) plate, (b) T-profile, (c) double T-profile and (d) involute [4].

.

Summarizing, even though the idea of an insert in a polymer matrix looks promising, its implementation is challenging concerning the thermal contact between the different bodies with different materials, the mechanical adhesion between them, and the manufacturing challenges that emerge [4].

## 2.7 Hybrid Polymer Gear Concept

In these next sections, the main works that will be used as foundation for this thesis purpose will be presented in more detail.

Previous works done by Moutinho [1] regarding different metallic inserts and their results will be analysed and a posterior validation of the hybrid polymer gear concept performed by Hooton [2] will also be exposed. In Moutinho's project [1], the goal was to accomplish the best compromise among the insert geometry, its dimensions, the material to use and its position in the polymer body. Hooton's work [2] is developed around a specific insert model where tests are performed using his own heating system to validate the hybrid gear tooth model.

### 2.7.1 Moutinho's Work

In his work, Moutinho [1] studied different geometries of metallic inserts, evaluating for each one stress and temperature and comparing solutions. The main goal was to achieve the best compromise among different insert materials and geometries, describing the influence of each of them on the temperatures and tooth root stresses and loading obtained. The author finally concluded which insert model provided the best improvement in the thermo-mechanical behaviour of the polymer hybrid gear.

For the metallic inserts, four different geometric variants were under analysis. Starting with the plate type, it could be simple or T plate. After, the type of insert, fixed when the insert is attached to a fixed ring around the bore hole, or floating, when simply inserted in the matrix of the gear. Also, the type of corners, filleted or not. Finally, the insert thickness. An example of some insert models are represented in Figure 2.9.

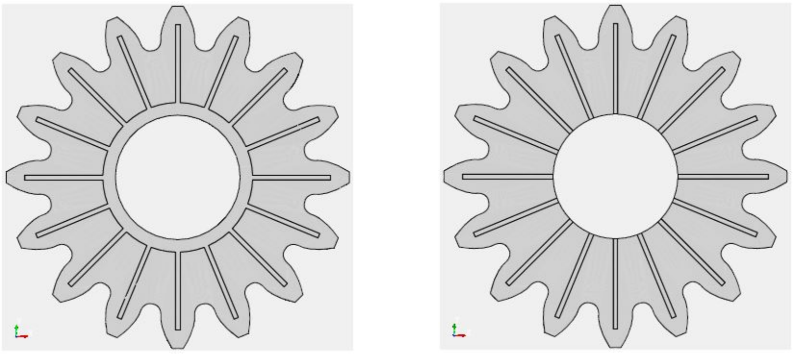

(a) Simple plate, fixed inserts (b) Simple plate, with floating inserts

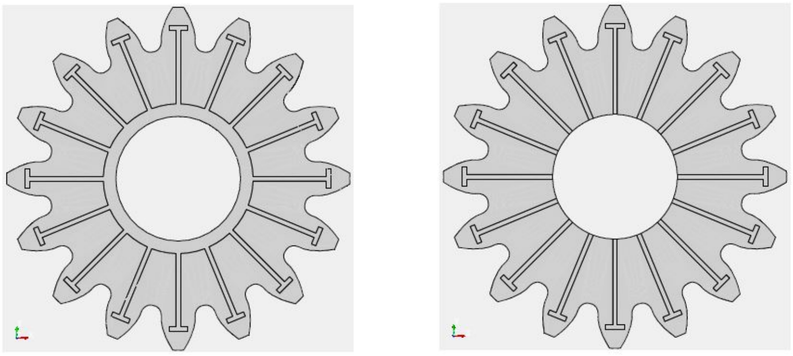

(c) T plate, with fixed inserts (d) T plate, with floating inserts

Figure 2.9: Example of different insert models studied by Moutinho [1].

The geometric dimensions are presented in Figure 2.10 and are based in a C14 type polymer gear. Moutinho [1] developed a FEM model where he was able to study the influence of each geometric variable, either for simple or T plate. Length ($w$), represents the insert width, distance ($L$) is the horizontal length of the T plate profile, distance ($t$) is the length from the tooth tip to the insert, and fillet radius ($Rd$) can be equal to 1 mm or 0.5 mm.

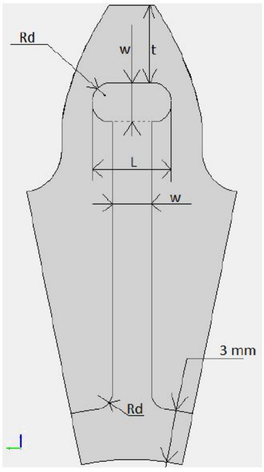

Figure 2.10: Insert's geometric dimensions [1].

All the insert profiles were analysed under the same loading conditions, using a torque of 10 N·m and a rotational speed of 1000 rpm. The temperature results for all the insert geometries were lower than for the standard polymer gear. Regarding the tooth root stress, the fixed T profile with straight corners, exhibited the lowest value, but has an increase in weight of 25% compared to the standard gear. For the majority of the simple plate inserts a higher tooth root stress was obtained when compared to the polymer gear. Nevertheless, simple plate inserts were not excluded since a lower temperature at maximum tooth root stress could still make them part of the equation. Moutinho concluded that geometric effects have less influence on tooth root stress for the simple plate inserts than for the T plate inserts. Therefore, the simple plate geometries needed improvements since their configuration with straight edges and close to the hub is increasing the stress and decreasing load carrying capacity.

Since floating inserts were causing extra stress, an optimization was performed by Moutinho, shortening the length of the insert and maintaining the other dimensions to study the tooth root stress, this time when the base of the insert was not in contact with the hub. Applying this solution, it was expected to obtain higher temperature and tooth root temperature, but a lower tooth root stress. The procedure consisted of simulating three specific increases in the length from the insert to the hub and again, try to improve the results obtained from the first simulations. Observing the results, it was found that a distance equal to the module of the gear was optimal, presenting a low enough value of tooth root stress without excessively increasing the tooth root temperature. Concluding, the final optimized insert geometry was the simple plate type, with straight corners and a distance from the insert to the hub equal to the gear module.

Once the ideal geometry among the different possibilities was defined, Moutinho studied the influence of the insert materials on the tooth root temperature and tooth root stress. For that purpose, three different insert materials were tested, copper, steel and aluminium. The result showed that tooth root stress is higher for aluminium, followed by copper and then steel. However, aluminium has the lower values for tooth root stress temperatures, together with copper. It was concluded that aluminium was the best material for the insert.

As a final improvement, and due to the high stresses in the interface of the hybrid tooth, caused by thermal expansion of the polymer material, Moutinho suggested a final solution. It consisted of using an epoxy silver-filled material as the insert. The advantages were its better compatibility with POM than aluminium, higher thermal conductivity and higher Young's Modulus than POM.

### 2.7.2 Hooton's Work

As previously mentioned at the introduction of the chapter, Hooton's work consisted of verifying the feasibility of the hybrid polymer gear and validate its concept, based on the final hybrid geometry suggested by Moutinho [1]. The tooth polymer material used was also POM.

In order to experimentally test the hybrid gear tooth, Hooton developed and manufactured a gear tooth heating system. The goal of the system was to apply concentrated heat on both gear tooth flanks, from a controlled source, and also to measure the temperature of different sections of the tooth. To closer simulate the gear meshing conditions, pressure was applied simultaneously with heat to the gear tooth. Summarising, the main requirements of the system were to apply both controlled pressure and heat to both tooth flanks, to control the point of contact of the applied load to the tooth flank and to be able to measure the surface temperature on the tooth using type K thermocouples. After a few iterations, the author achieved a final system, represented in Figure 2.11.

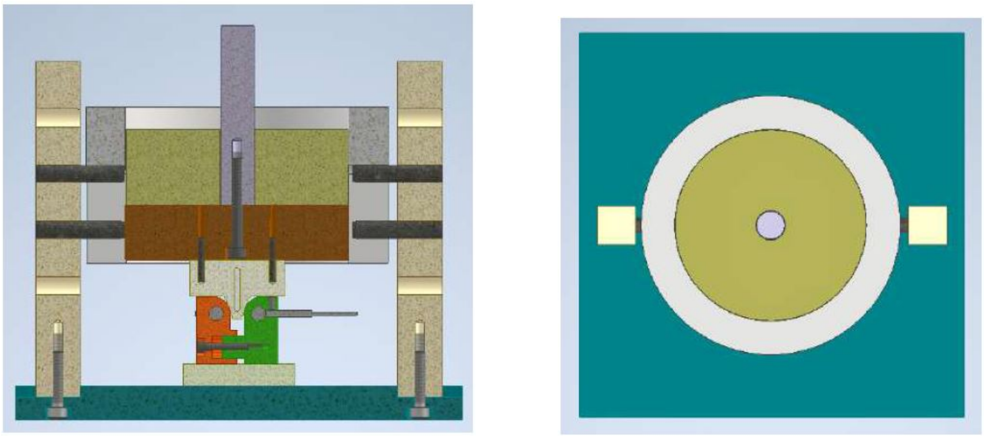
(a) Front view

(b) Top view

Figure 2.11: Final gear tooth heating system developed by Hooton [2].

Before proceeding to the experimental tests, a FEM model of the tooth was developed by Hooton in order to use it to compare and understand the experimental results. Both thermal and thermo-mechanical models were created to simulate the exact condition of the heating System. For the thermal model, the boundary conditions took into account the heating System design and also the procedure used for the thermal tests. Regarding the mechanical model, its development complements the previous simulation by better simulating the real conditions the tooth rack is submitted to. The boundary conditions took into account the heating System design. Finally, the thermo-mechanical model coupled the thermal and mechanical models mentioned so far. After defining the FEM models, thermal test and digital image correlation (DIC) tests were prepared.

Starting with the thermal tests, the goal was to study the impact of different insert materials, as well as to validate the hybrid gear concept when applying heat to the tooth flank. Four different specimens were tested: the standard tooth rack (STD), the hybrid tooth rack with no insert (HT1), hybrid tooth rack with an aluminium insert (HT2) and hybrid tooth rack with an epoxy insert (HT3). In Figure 2.12, it is represented the location of the bore holes for the thermocouple.

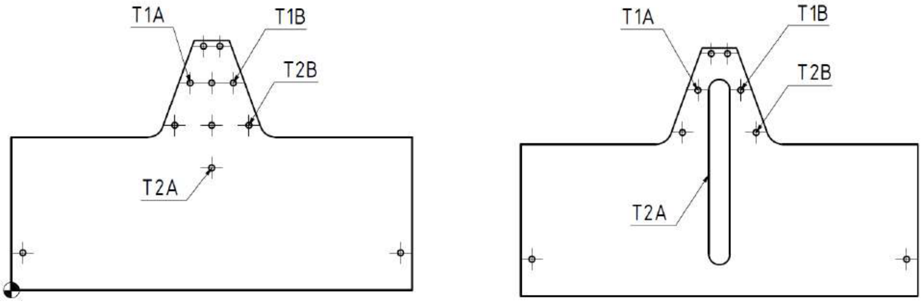

(a) Standard tooth (b) Hybrid tooth

Figure 2.12: Bore holes location for the thermocouple used for the thermal tests [1].

Thermal tests measurements were performed for all the four specimens with a heat temperature in the interval range of $T_{Heater}$=[40, 50, 60, 70, 80, 90, 100, 110] °C, and with only one flank of the tooth being heated (the $T_{1b}$ flank side). For a better analysis of the impact of the hybrid tooth design, relative change of temperature was calculated for each hybrid tooth in relation to the standard tooth. For the temperature $T_{1a}$, STD and HT1 (air) obtained similar results with an average temperature change o 1.9 %, while HT3 (epoxy) registered 6.7 % of temperature change and HT2 (aluminium) 12.6 %. From these first results, it was possible to conclude that in presence of an insert, the hybrid teeth were more capable of absorbing heat. Next, $T_{1b}$ temperature was analysed, with HT1 (air) being 5.2 % lower than STD, a result that could be explained by the convective heat transfer inside the region of the insert. The highest temperature change was for HT2, with an average of 27.9 % and HT3 got 19.6 %. Regarding $T_{2a}$, it was a very important region to study since it is where the insert would be located at. HT1 and HT3 did not register any significant temperature changes, with an average temperature change of 1.1 % for HT3. However, HT2 has registered an average temperature change of 30.4 %. The difference between the results for HT2 and HT3 could be explained by the difference of the thermal conductivity of the materials insert.

For the digital image correlation (DIC) technique, it consists of measuring surface displacements by capturing a series of images during the experimental procedure, and then comparing the coordinates of the reference image with the deformed image. This technique will also be used in the experimental section of this thesis, so it will be explained again, in more detail in the next chapters. The objective of these experiments was to study the thermal expansion of the tooth rack polymer material and also to validate the thermo-mechanical model, again, when heat is being applied to the tooth flank. The standard tooth rack and the hybrid tooth without an insert were the specimens to test and in Figure 2.13, it is represented the location of the bore holes for the thermocouple.

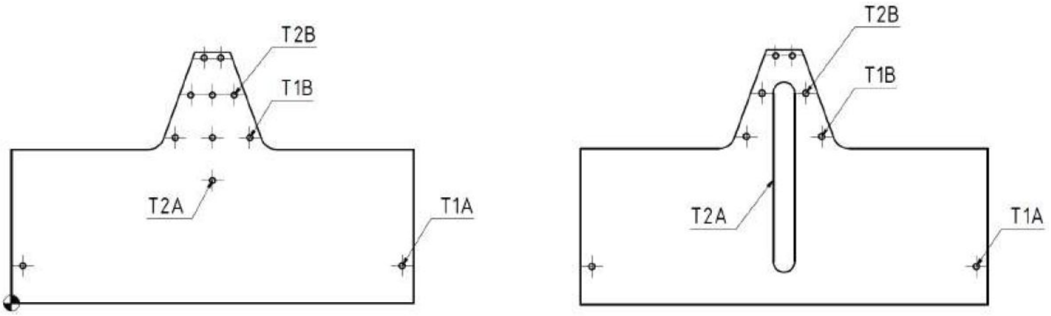

(a) Standard tooth (b) Hybrid tooth

Figure 2.13: Bore holes location for the thermocouple used for the DIC tests [1].

DIC tests were performed with a heat temperature in the interval range of $T_{Heater}$=[40, 70, 100] °C.

For the standard tooth rack, it presented the largest thermal expansion for $T_{Heater}$=100 °C. In the x direction, the thermal expansion was greater on the right side of the tooth due to the heating only coming from the cartridge heater of the right side. The temperature at the pitch point was the highest, but in the x direction the tooth's expansion was restricted by the heaters. In y direction, there were higher displacements for the gear tip and lower for the base of the tooth. The maximum y direction displacement was coincident with the contact point of the cartridge heater, which is also the tooth region with the highest change in temperature.

For the hybrid tooth rack measurements, in the x direction, although the displacement values for $T_{Heater}$=40 °C were 125 % larger than the standard tooth, they did not change significantly with the increase of the temperature. It resulted in a displacement value 33.7 % lower than the standard tooth for $T_{Heater}$=100 °C. Regarding y direction, for all the temperature increments, there was also an increase of the maximum displacements. For a $T_{Heater}$=40 °C, the displacement value was 125 % higher than the standard tooth, and for the other two temperatures, that value decreased for 33 %.

Finally, Hooton compared the experimental results with the adjusted FEM models and took the final conclusions.

Concerning the thermal model validation, for the STD, the results showed that the model could accurately predict the surface temperature, with the relative errors varying in the interval [6.1; 14.8] %. In the HT1 case, the relative errors were higher, [12.5; 29.5] % and for the HT2 specimen, [12.3; 39.4] % values were obtained.

For the thermo-mechanical model validation, in the standard tooth rack case, the model was considered as accurate, since the y displacements were accurate along the length of the tooth, and the x displacements as well, but with an offset caused by the rigid body motion of the heaters. Regarding the hybrid tooth rack, a similar analysis happened compared to the previous case. Here, the x displacements showed a similar progression with an offset from the DIC results, for the same reason previously mentioned. Also, the maximum displacements registered in the DIC test were significantly higher than the FEM results. The y displacements were accurate, but also the maximum values registered in the DIC tests were significantly higher than the FEM results, with an offset of the displacement values for the insert region and tooth tip. To validate the model, Hooton considered some final details and the model was validated.

At the end of the work, a comparison of the thermal behaviour of the STD, HT2 (aluminum) and HT3 (epoxy) was performed, to conclude that the hybrid teeth with an insert require significantly less power to increase the minimum body temperature. For the HT3, 85.9 % and for the HT3 63.8 % less power than the STD.

## 2.8 Specifications of the Hybrid Gear Tooth Specimen

As a continuation of the work performed by Hooton [2], in this work the hybrid gear tooth geometry to study will remain the same. This way, a C14 standard gear geometry was employed.

Only a single gear tooth is needed to be tested, so a pinion and rack system was used. This approach is advantageous given the simpler geometry and simpler manufacturing process of the rack system.

A standard and an hybrid tooth geometries will be exposed. The detailed dimensions of the tooth rack bodies, which are the same for both specimens will be shown, as well as the insert region details for the hybrid tooth.

### 2.8.1 Gear Geometric Properties Calculation

Firstly, to determine the gear geometry KISSsoft software was used. This software gives the user the possibility to generate and study several different machine elements, based on different standards. Some of the most important utilities used for this work were the data calculation and the functionality to export the geometry to any 3D CAD software in a STEP file format.

In order to obtain the 3D model and its geometrical properties, the following steps were covered in the KISSsoft software:

- **1st**: Geometry properties for pinion and wheel were obtained based on the C14 standard gear;

- **2nd**: C14 gear pinion values were used to create a pinion and rack model;

- **3rd**: Tooth rack geometric parameters were obtained and a 3D pinion and rack model was exported.

In table 2.5, are shown the pinion and rack geometric properties.

Table 2.5: Pinion and rack geometric properties obtained from the KISSsoft software.

| Property | Pinion | Rack |
|---|---|---|
| Number of teeth, z | 16 | - |
| Module, m / mm | 4.5 | |
| Center distance, $a_c$ / mm | 82.318 | |
| Pressure angle, $\alpha_n$ / ° | 20 | |
| Face width, b / mm | 14 | |
| Root radius coefficient, $\rho_r$ | 0.38 | |
| Fillet radius, $r_f$ / mm | 1.71 | |
| Addendum modification, x | +0.1817 | 0 |
| Addendum coefficient, $h_{aP}$ | 1 | |
| Deddendum coefficient, $h_{fP}$ | 1.25 | |

### 2.8.2 Tooth Rack Geometry Definition

KISSsoft generates a 3D rack and pinion model, however, only one tooth will be necessary to perform the tests, as mentioned before. At this point, it will be required to import the model into a 3D modeling software (as a STEP file), in this case SolidWorks, so the tooth rack will be trimmed into one tooth with proper specific dimensions. The dimensions chosen are explained next, based on properties obtained from Table 2.5.

#### 2.8.2.1 Standard and Hybrid Tooth Rack

The rack length, $l_{rack}$, was set as three times the length of an individual tooth. This means that this dimension will be equal to three times the pitch circle dimension, $p$, Equation 2.1.

$$l_{rack} = 3 \cdot p = 3 \cdot \pi \cdot m = 42.41 \text{ mm} \tag{2.1}$$

Concerning the rack body height, $h_{rack,b}$, it was defined as the length between the pinion root radius or deddendum radius, $r_d$, and the shaft radius, $r_{shaft} = 15$ mm. The deddendum radius is calculated as given in Equation 2.2.

$$r_d = r - h_{fP} \cdot m = \frac{z_1 \cdot m}{2} - h_{fP} \cdot m = 30.37 \text{ mm} \tag{2.2}$$

Also, considering the profile shift coefficient, $x_1$, it is possible to finally obtain the rack height, Equation 2.3.

$$h_{rack,b} = r_d + x_1 \cdot m - r_{shaft} = 16.19 \text{ mm} \tag{2.3}$$

As the dimensions of the rack body were defined, it was now performed the action of removing the extra material, using SolidWorks software. The two extra teeth were cut off and the rack body dimensions were adjusted, also applying the cutting tools.

The final result for the standard tooth rack is presented in Figure 2.14.

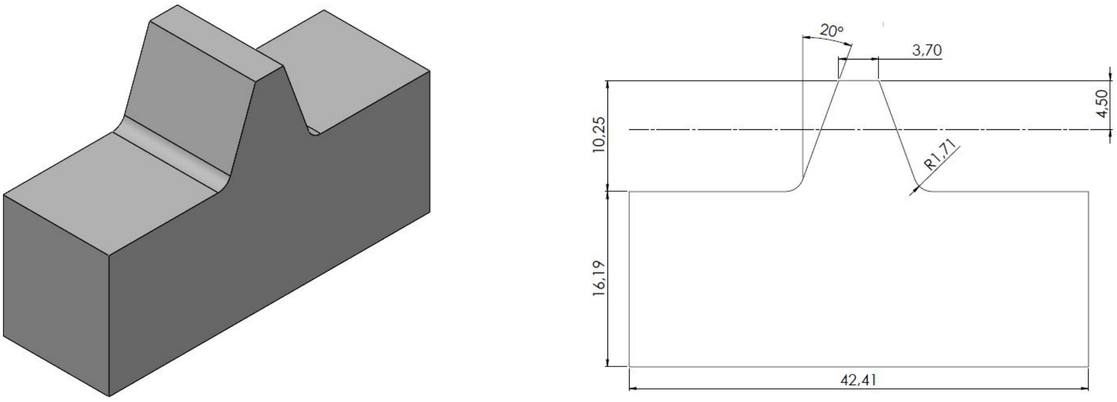

(a) Isometric view.

(b) Geometry.

Figure 2.14: Standard tooth rack geometry definition.

For the hybrid tooth rack geometry definition, the previous trimming process applied to the standard tooth rack had remained, but a new extruded cut action was needed to house the inserts.

To determine the insert geometry and dimensions, the conclusions reached in Moutinho's [1] work were used. As mentioned at the end of section 2.7.1, the ideal insert geometry was the simple plate type, with straight corners. However, in the present project, and following Hooton's [2] work, the insert geometry was chosen to have round corners, for the greater simplicity when manufacturing the part.

Thus, the insert geometry has a width equal to half of the gear module, the distance from the insert to the hub and from the insert to the tooth tip is equal to the module. The length of the insert is now easily deduced subtracting to the total height of the rack, $h_{rack}$, two times the module, Equation 2.4.

$$l_{insert} = h_{rack} - 2 \cdot m = 17.44 \text{ mm} \tag{2.4}$$

Finally, the SolidWorks extruding cut tools were used again to create the final hybrid tooth rack, Figure 2.15.

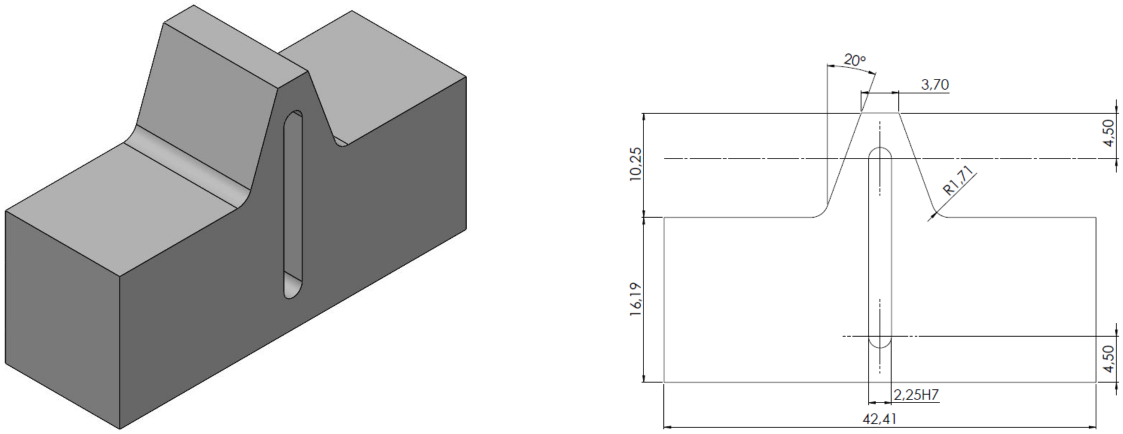

(a) Isometric view.

(b) Geometry.

Figure 2.15: Hybrid tooth rack geometry definition.

### 2.8.3 Chosen Materials

#### 2.8.3.1 Tooth Rack Polymer Material

In section 2.2, it was listed some of the most typical polymer materials used in gears. The material selection process had to take into account not only the research made on common gear polymer materials used, but also previous works and studies related to this topic.

The interest of the project was to choose the same polymer material used in Hooton's work [2] and with the same specimen geometry develop a new test equipment to simulate closer conditions to what happens in gear meshing. That being said, the polymer material chosen was the type c acetal, ERTACETAL C® (PolyLanema Lda., Portugal). Its properties can be consulted in Table 2.6.

Table 2.6: Material properties of ERTACETAL C®.

| Property | ERTACETAL C® PolyLanema |
|---|---|
| Young modulus, E / GPa | 2.8 |
| Density, $\rho$ / kg/m$^3$ | 1410 |
| Thermal conductivity, $\kappa$ / W/(m·k) | 0.31 |
| Thermal expansio coeff. [23-100°C], $\alpha$ / °C$^{-1}$ | 1.25E-04 |
| Max. service temperature / °C | 140 |
| Max. continuous service temperature / °C | 100 |
| Melt temperature, T$_f$ / °C | 165 |

#### 2.8.3.2 Hybrid Tooth Insert Material

Regarding, the hybrid tooth insert material, only aluminium will be tested, since the silver filled epoxy resin showed some problems in this function, as studied by Hooton [2].

The aluminium alloy properties are presented in Table 2.7.

Table 2.7: Material properties of Aluminium 6061 alloy.

| Property | Aluminum 6061 alloy |
|---|---|
| Young modulus, E / GPa | 69 |
| Poisson's ratio, $\nu$ / - | 0.33 |
| Density, $\rho$ / kg/m$^3$ | 2700 |
| Thermal conductivity, $\kappa$ / W/(m·k) | 237 |
| Thermal expansion coeff., $\alpha$ / °C$^{-1}$ | 2.25E-05 |

# Chapter 3

# Design and Manufacturing of a Gear Tooth Heating and Loading System

## 3.1 Introduction

After defining the tooth rack geometry and understanding some of the previous works focused on the hybrid polymer gears topic, it is now necessary to design and manufacture an heating and loading system capable of performing the experimental tests.

Initially, a set of requirements were established which served as the foundation to the system design. With these requirements set, and after searching for some existing gear testing models, the initial sketches were drawn up. During this project development process, new ideas and better solutions kept emerging, making the design phase go through some iterations. The system was developed using SolidWorks, a 3D CAD software.

All the gear tooth heating and loading system details will be exposed throughout this chapter.

## 3.2 System Objectives and Requirements

The objective was to build a system capable of inducing heat and a load application to one of the tooth flanks, so to approximate this conditions to what happens in the real case for gears meshing. Some of the system specifications are similar to the ones used in Hooton's work [2]. However some other new requirements were imposed for the present work, so the system must be designed from scratch in order to comply with those purposes.

In the following list the system requirements needed to accomplish the objectives are stated:

- Apply heat and pressure to only one of the tooth flanks;
- Guarantee the fixation of the tooth rack, when load and heat are being applied to one of its flanks;
- Apply the contact pressure in different positions of the tooth flank. When no load is being applied, the system must allow a translation movement of the teeth to readjust its position;

- Apply different pressures values before the beginning of the experimental tests, using a dead weight system;
- Control temperature values during the experimental tests, using a cartridge heater;
- Monitor temperature values supplied by the heating source, and the temperature field on the entire tooth surface, using a thermal camera.

## 3.3 Design Phase

As previously mentioned, the design phase was approached keeping in mind the objectives and requirements, as well as some already existing gear tooth testing systems, such as the one schematically presented in Figure 3.1.

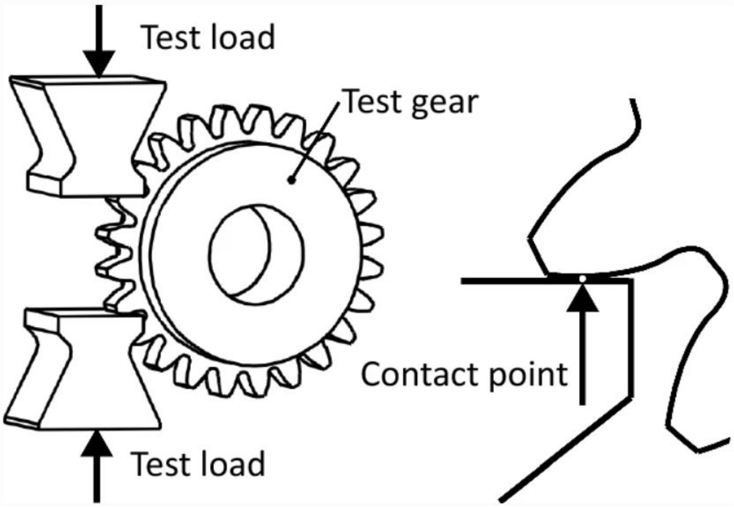

Figure 3.1: Gear tooth testing machine model [14].

Inspired in this successful gear tooth testing mechanism, a system where the load was also applied on the tooth rack using a tool with a vertical translation movement, was developed.

Immediately, it was thought to use two linear guides: one vertical linear guide (3) to move up and down the weight (6) and to transport the load and heat application tool (7); one horizontal linear guide (11) which enables the positioning of the tooth rack (9), so the pressure could be applied in different points of the tooth flank. An initial 3D design was made to visualize the idea which can be seen in Figure 3.2. The main parts of the system are listed for a better perception of the initial idea.

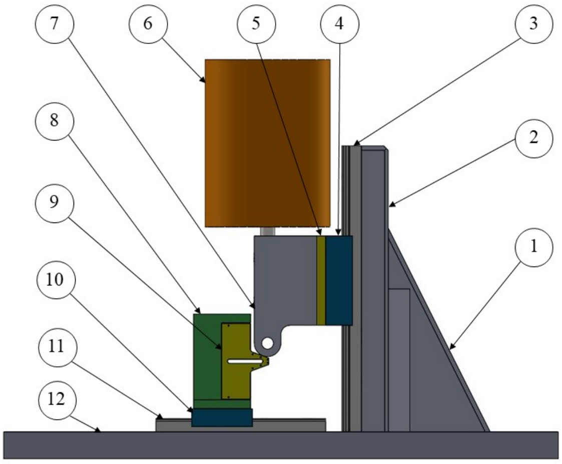

| Item number | Descripton |
|---|---|
| 1 | Vertical Rib |
| 2 | Vertical Support Column |
| 3 | Vertical Linear Guide |
| 4 | Vertical Guide Carriage |
| 5 | Polymer Plate |
| 6 | Weight |
| 7 | Load and Heat Application Tool |
| 8 | Hybrid Polymer Gear Support |
| 9 | Hybrid Polymer Gear Tooth |
| 10 | Horizontal Guide Carriage |
| 11 | Horizontal Linear Guide |
| 12 | Table Support Plate |

Figure 3.2: Initial 3D design of the gear tooth heating and loading system, and respective part list.

The general description of the mechanism will be now exposed. In this initial 3D design, there is a load and heat application tool (7) in contact with the tooth rack (9) flank. This tool is connected to the vertical guide carriage (4), having a vertical polymer plate (5) interface in between them. The top cylinder would be used as the weight (6) to apply the necessary pressure on the tooth flank. This weight (6) was intended to be supported in the upper part of the load and heat application tool (7). To hold all the vertical components and keep them stabilized, a vertical support column (2) with a rib (1) was designed.

Regarding the tooth rack (9), it was created a support (8) that would fix it by using two hexagon socket head cap screws (ISO 4762), one on the top and one on the bottom. As seen in Figure 3.2, the hybrid polymer gear support (8) would also be laterally restricting the movement.

Given the very general description of the initial 3D design, it is now important to go into more detail and understand better the solutions here exposed.

### 3.3.1 Components Attached to the Vertical Part of the System

In this section, all the components attached to the part of the system responsible for the vertical movement of the load and heat application tool will be addressed.

The load and heat application tool is one of the most important parts, because of its direct responsibility in assuring the contact with the tooth rack flank. This component must have a hole which would allow to hold a cartridge heater and also an application tip with a round shape and a specific radius. An initial solution was developed, Figure 3.3.

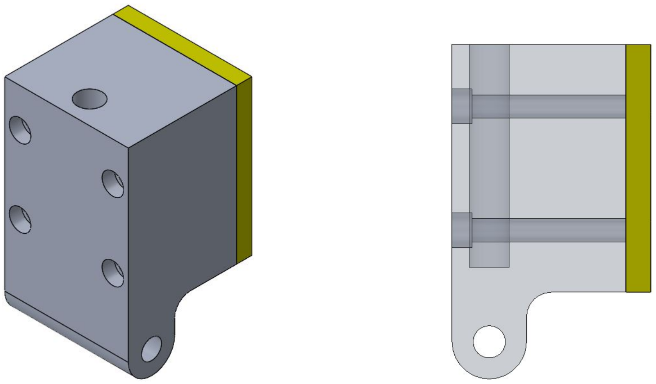

(a) Isometric view. (b) Front view.

Figure 3.3: Initial design of the load and heat application tool.

In the first solution, the load and heat application tool was attached to the vertical guide carriage by four hexagon socket head cap screws (ISO 4762) and this part of the system had a single polymer vertical plate. The role of the polymer plate was to prevent the heat conduction to the carriage in order to do not damage it and its function. Before proceeding to further details, the first modifications start.

First of all, the heat problem was not completely solved since the polymer plate was still very close from the carriage and the heat could still propagate through the tool material and through the plate. To solve that, it was implemented a solution of two plates closer to the application tip. Now, a polymer vertical plate attached to the tool by one hexagon socket head cap screw (ISO 4762), and a polymer horizontal plate, together with the tool, attached to a new application block by two hexagon socket head cap screws (ISO 4762) enabled a better safety and blocking of the heat conduction. Moreover, to facilitate the tool tip production, its geometry was modified consisting now of only one round edge and all the other corners straight, Figure 3.4. With this change, it was also easier to manufacture the threaded holes to house the hexagon socket set screw flat point (ISO 4026), which would guarantee the fixation of the cartridge heater on the hole of the load and heat application tool. Another centered threaded hole was manufactured to house a Pt100 sensor, which will be used to monitor the cartridge heater temperature values.

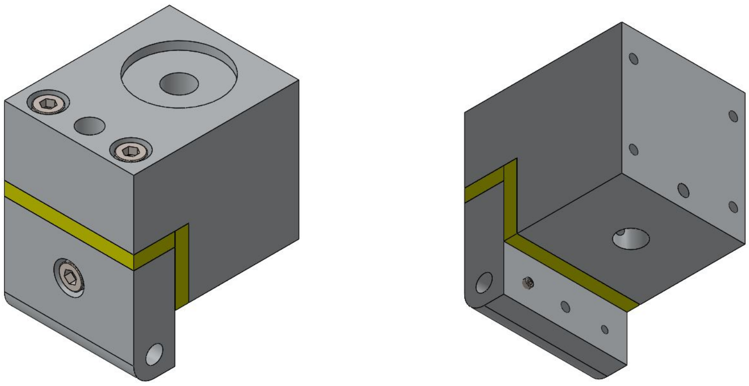
(a) First isometric view.
(b) Second isometric view.

Figure 3.4: Isometric views of the new solution design for the assembly of the load and heat application tool.

An important addition was also a new way to apply the weights on the system. Initially, the weights were applied on the top of the load and heat application block, as represented in Figure 3.5a. This approach was already addressed when the general description of the initial 3D design was made. Due to the instability when many weights need to be used, a new version was developed allowing the weights to be applied from the bottom. Basically, if a closer look is taken to Figure 3.4 and 3.5b, there is a through-hole in the table support plate and in the load and heat application block, where a shaft with threaded ends passes through. At the shaft ends, there are two circular plates, also with threaded inner holes, so they are fixed to the shaft. One of the plates rests on the top of the load and heat application block, and the other one is located at the bottom of the system and its function is to support the weights. In this new configuration, with the entire system fixed in a working table, the weight application is done on the bottom side of the table, guaranteeing a better system stabilization and security, as well as more space on the top part of the table to operate the equipment.

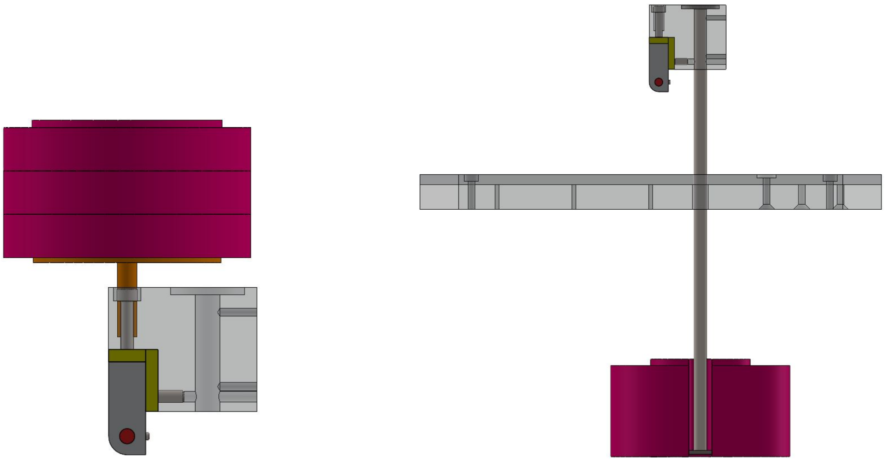

(a) Top application of the weights.

(b) Bottom application of the weights.

Figure 3.5: Two different approaches to apply the weights on the gear tooth heating system.

Regarding the remaining components, it is necessary to mention that there is a support column and a vertical rib which support and align the vertical linear guide, as can be seen in Figure 3.6. The alignment is performed by two perpendicular grooves. One of the grooves goes across the table support plate from one end to the other, which permits to align not only the vertical rib, but also the components of the horizontal part of the system (explained in the next section 3.3.2). This vertical rib is connected to the plate by two hex socket CTSK head (ISO 10642). The other perpendicular groove aligns the support column, which is also attached to the table support plate by two hex socket CTSK head (ISO 10642).

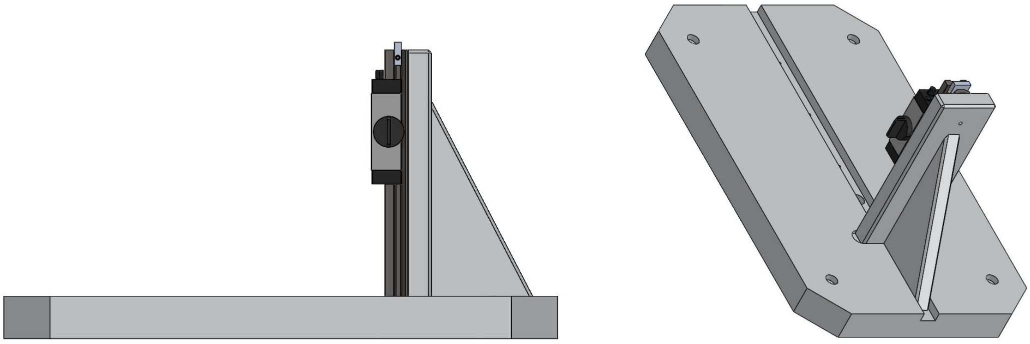

(a) Vertical support parts, front view.

(b) Vertical support parts, isometric view.

Figure 3.6: Final 3D design and positioning of the support column and vertical rib, which support the vertical linear guide, on the table support plate.

All the threaded connections and construction specifications addressed so far, can be consulted in more detail in Appendix A.

Regarding the vertical linear guide, it is important to refer that it was purchased a Drylin® T guide rail TS model, mounted with a Drylin® T guide carriage TW-01-HKA model with a manual locking device. The carriage has a static carrying capacity of 4000 N and a static load capacity of 25 Nm in the direction parallel to the table support plate width. The aluminium and polymer materials of this part of the system were applied also taking into consideration the low weight and the high stiffness (in the case of the aluminium material) they would offer. Summarizing, the linear guide safely supports the weight of all the components attached to the vertical part of the system, as it will be calculated in Section 5.2.2.

### 3.3.2 Components Attached to the Horizontal Part of the System

On the horizontal part of the system is where the specimen fixation mechanism is located at. Here, there is an horizontal linear guide used to allow the positioning of the tooth rack, so different points on the tooth flank can be tested. The horizontal guide carriage supports the test specimen and its support. In this part of the project what really changed since the first design of Figure 3.2 was the approach to get the tooth rack fixed when pressure is being applied.

The first configuration is shown in Figure 3.7. It consists of a support with a rectangular shaped platform to fully settle on the carriage of the horizontal linear guide, with four hexagon socket head cap screws (ISO 4762). In addition, the support also has other two hexagon socket head cap screws (ISO 4762), one on the top and the other on the bottom (Figure 3.7a), which attach the tooth rack to the support. On these top and bottom sides, it was given a slight clearance between the tooth rack and the tooth support for the thermal expansion effect, while the base of the specimen rests on the support. The problem that arises from this solution is precisely related to the thermal expansion effects. During Hooton's work [2], the author connected the base of the tooth rack to a platform using a thread connection. What happened was that this restrictive connection did not allow the POM material of the specimen to thermally expand in its normal way, showing some impact on the final results. Some extra stresses appeared in this region, which was not the most optimized way to simulate the polymer hybrid gear tooth behaviour. Keeping this in mind it was necessary to improve the specimen fixation.

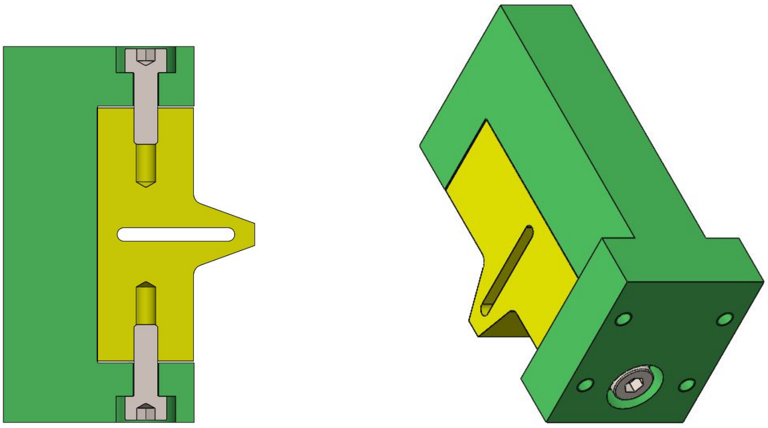
(a) Section view of the 3D design.
(b) Isometric view of the 3D design.

Figure 3.7: First 3D design of the hybrid polymer gear tooth base.

It was decided that the new solution could not have any threaded connection to fix the tooth rack, so a new connection construction was conceived, Figure 3.8. In this case, there is a hybrid polymer gear tooth base, where the tooth rack and the hybrid polymer gear tooth support are placed at. The hybrid polymer gear tooth support is attached to the vertical part of the base by four Hexagon socket head cap screws (ISO 4762), and in turn, the base is connected to the linear guide carriage by other four hexagon socket head cap screws (ISO 4762). Therefore a dovetail construction was applied. What this construction solution offers is a non restrictive material thermal expansion, while it keeps the tooth rack safely fixed during the tests performed. The dovetailed connection is practicable mainly when dealing with traction loads.

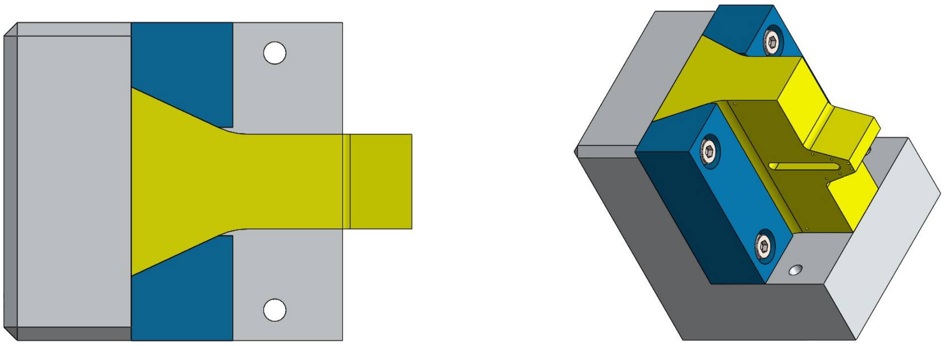
(a) Top view of the 3D design.
(b) Isometric view of the 3D design.

Figure 3.8: Final 3D design of the hybrid polymer gear tooth base and support.

Finally, it was also essential to ensure the correct alignment of the horizontal linear guide with the vertical part of the system. Thus, as previously stated, a groove that covers the entire table support plate through its length is responsible to align the vertical supports with the horizontal linear guide. There is an horizontal linear guide support fitted in the groove and then, the guide is based on the support and at the same time aligned by the groove, Figure 3.9. This way, a correct positioning is preserved and the support gives the guide a sufficient height to work properly. The connection among these three elements, the guide, its support, and the table support plate is done by three hexagon socket head cap screws (ISO 4762). As the groove along the length is the same used both for positioning the vertical and horizontal parts of the system, the required alignment between these parts is achieved.

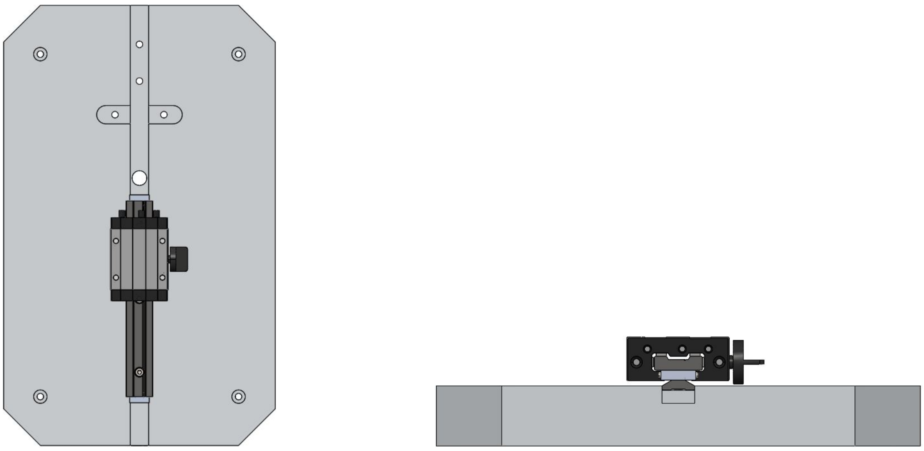

(a) Top view of the 3D design.

(b) Bottom view of the 3D design.

Figure 3.9: Final 3D design and positioning of the horizontal linear guide on the table support plate.

As in the vertical part of the system, here it was purchased a Drylin® T guide rail TS model for the horizontal guide, mounted with a Drylin® T guide carriage TW-01-HKA model with a manual locking device. In the horizontal part of the system aluminium and polymer materials were used to guarantee enough stiffness (in the case of the aluminium) and a low weight, so the horizontal carriage is able to safely support all the load, whether the vertical load is being applied or not.

### 3.3.3 Final Design and Technical Drawings

The final solution that was manufactured and used for this experimental work is presented in Figure 3.10.

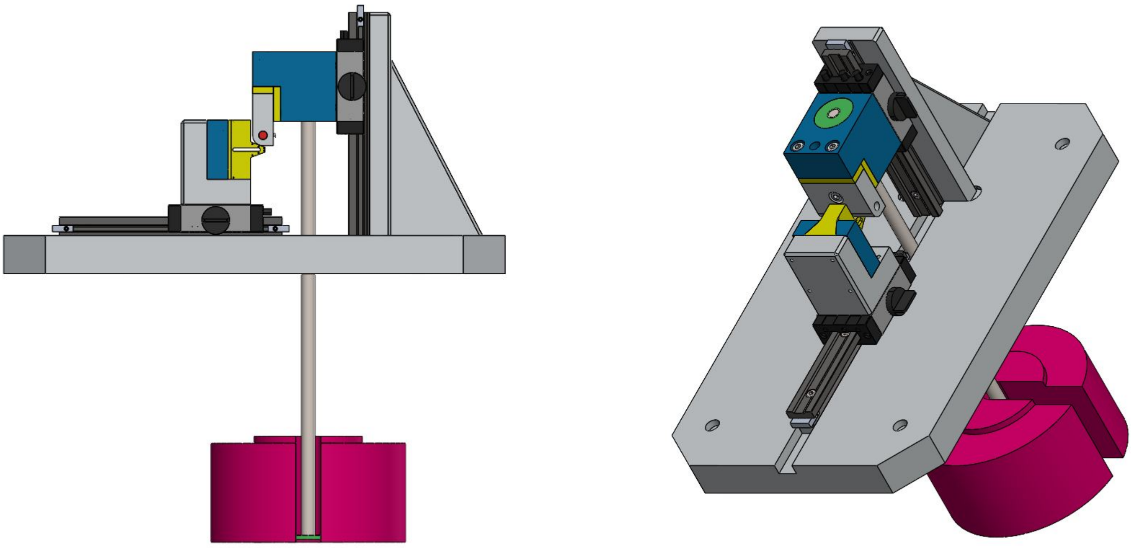

(a) Front view of the 3D design.

(b) Isometric view of the 3D design.

Figure 3.10: Final 3D design of the complete gear tooth heating and loading system.

In Figure 3.11 it can be seen the system fully set up in the working table.

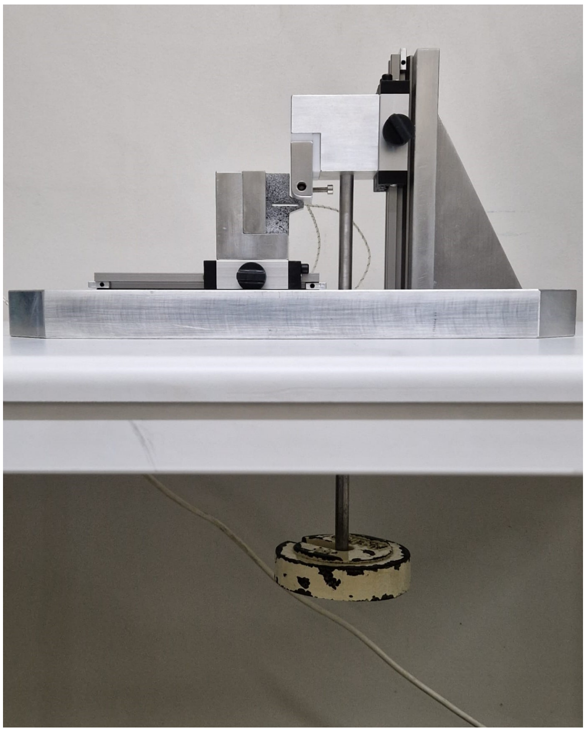

Figure 3.11: Gear rack test rig setup.

To check all the manufacturing drawings, including the assembly drawing and the bill of materials, Appendix A should be consulted.

# Chapter 4

# Thermal and Thermo-Mechanical Finite Element Models

## 4.1 Introduction

To simulate both the tooth rack and the hybrid tooth rack behavior under thermal and mechanical conditions, a FEM model was created.

The procedure was to first develop a mesh for each specimen, using the Gmsh software, and then to import the mesh into a FEM software, in the case PrePoMax, so the thermal and mechanical conditions were applied to the model. At the end, a h-refinement method was implemented for the results to converge.

## 4.2 FEM Mesh

Before proceeding to the mesh generation, it is important to make a brief introduction to the Gmsh functionalities that will be employed during the FEM mesh development. First of all, Gmsh is an open-source software created for a fast and user-friendly 3D finite element mesh generation, including a built-in CAD engine and post-processor. The programm is based on four modules, geometry, mesh, solver and post-processing, and each of them can be controlled either using a graphical user interface (GUI) or a scripting language, similar to standard C++ [15].

To define a 3D model, Gmsh uses boundary representation and so it comprises four kinds of model entities, those being vertices, edges, faces and regions. Regarding the meshing process, the software is able to deal with the majority of the finite element shapes: lines, triangles, quadrangles, tetrahedra, hexahedra, prisms and pyramids. Structured and unstructured meshes are available in 1D, 2D and 3D. For instance, there are several techniques and technologies incorporated, such as transfinite and elliptic meshes for the structured algorithm [15].

The software offers several output file formats facilitating the integration with other computational tools, in particular, other FEM solver programs, such as Calculix which will be used in this work.

For the FEM models, the dovetail section of the tooth rack will not be analysed, since it has a very little influence, so it can be disregard. Also, it would significantly increase the computational time.

### 4.2.1 Standard Tooth Rack Mesh Generation

To create the standard tooth rack mesh in the Gmsh software, it was firstly necessary to introduce the geometry parametric coordinates to generate the points of the 2D design. With the point coordinates set, lines were created by connecting the points and shaping the 2D geometry of the standard tooth rack. In order to build a structured mesh, a transfinite algorithm was applied to the lines, in which the number of nodes per curve was defined. With the number of nodes defined, it is also possible to change their progression, allowing to apply more nodes closer to one of the ends of the curve. This setting was used to concentrate more nodes closer to the tooth flank where the heat and load are being applied. Next, the tooth rack was divided into several regions to allow the generation of a more detailed mesh in the different tooth rack regions. This surface generation is intuitively done by selecting the contour lines of the surface geometry that is wanted to delimit. Also, a transfinite algorithm was again applied, now to the 2D geometry, and then it was recombined, as presented in Figure 4.1.

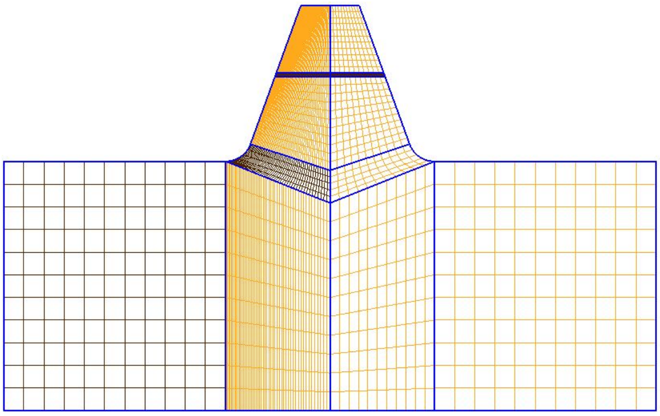

Figure 4.1: Standard tooth rack 2D mesh model.

As a final step, it was only missing the extruding of the 2D geometry to obtain the final 3D mesh with the eight-node brick elements, C3D8, presented in Figure 4.2.

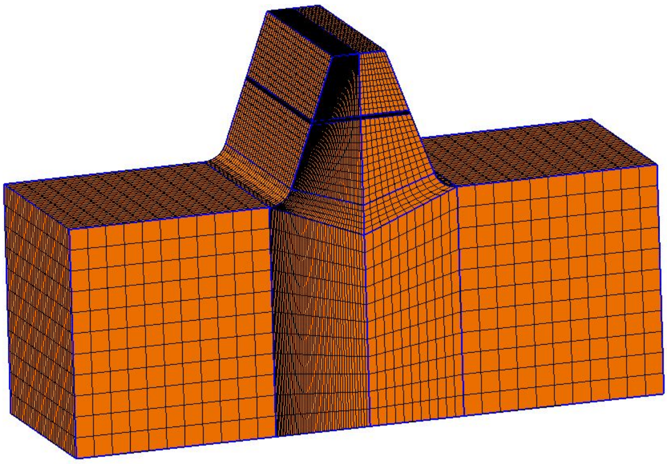

Figure 4.2: Standard tooth rack 3D mesh model.

### 4.2.2 Hybrid Tooth Rack Mesh Generation

The procedure to generate the hybrid tooth rack mesh was quite similar to the one described for the standard tooth rack. Thus, the geometry parametric coordinates were defined, now also taking into account the hollow intended for the insert and the insert itself. Then, the points were connected by lines which formed the 2D geometry of the hybrid tooth rack. Once again, a transfinite algorithm was applied to the lines, with the number of nodes per curve being defined. To create different regions, several surfaces were defined by picking the lines which delimit the surface geometry intended to define. For the 2D geometry a transfinite algorithm was applied as well, and recombined resulting in the now presented Figure 4.3.

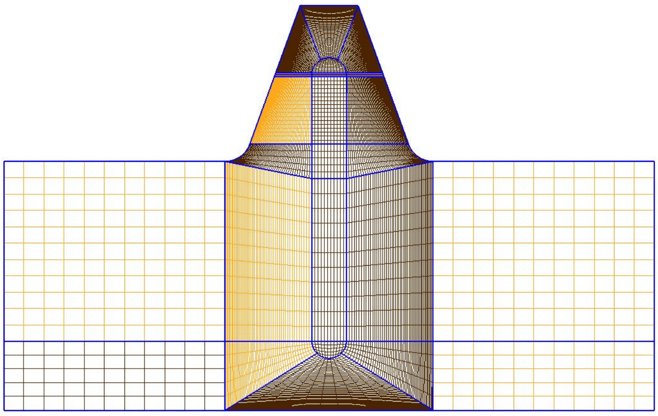

Figure 4.3: Hybrid tooth rack 2D mesh model.

After extruding the 2D geometry, the 3D mesh with the eight-node brick elements, C3D8, of Figure 4.4 was obtained.

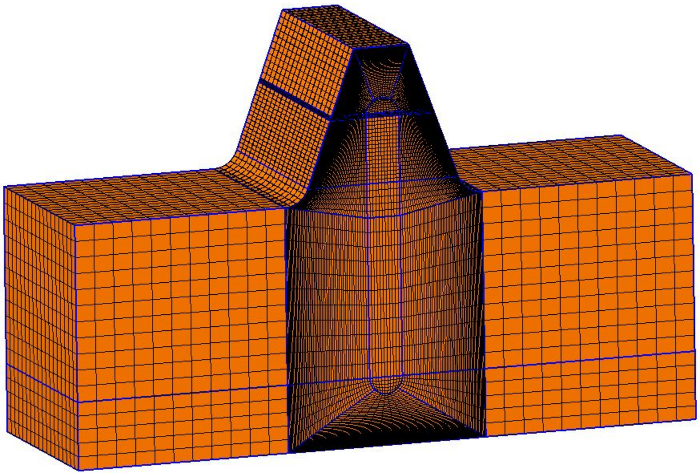

Figure 4.4: Hybrid tooth rack 3D mesh model.

## 4.3 Thermal Model Definition

After generating the necessary meshes for all the racks to test, the thermal model conditions need to be defined as close as possible to the real system behaviour. Throughout the model definition, the dovetail section of the tooth rack will not be analysed, since it has a very little influence in the thermal component, so it can be disregard. Also, it would significantly increase the computational time.

In the next sections, all the boundary conditions applied will be addressed and the steady state approximation will also be explained.

### 4.3.1 Steady State

For transient thermal problems, the temperature distribution for meshing gears in the three dimensional space is governed by the equation 4.1.

$$k \cdot \left( \frac{\partial^2 T}{\partial x^2} + \frac{\partial^2 T}{\partial y^2} + \frac{\partial^2 T}{\partial z^2} \right) = \rho \cdot c_p \cdot \left( \frac{\partial T}{\partial t} \right) \tag{4.1}$$

Regarding the transient effects, those are negligible at points below the meshing tooth flank, but considerable in this surface region. It is assumed that after a sufficiently long time from the start of the heat source's work, the temperature solution within the body can be considered quasi-steady. Also, in a steady state, the bulk temperature of a point distant from the heating source is considered constant at any point on the gear [3]. Taking the previous hypothesis into account, the temperature distribution problem in the tooth rack can be approached based on a steady state problem.

Thereby, this consideration implies the transient term of equation 4.1 to be null, equation 4.2.

$$\frac{\partial T}{\partial t} = 0 \tag{4.2}$$

Finally, the governing equation for the steady state is given by equation 4.3 [3].

$$k \cdot \left( \frac{\partial^2 T_B}{\partial x^2} + \frac{\partial^2 T_B}{\partial y^2} + \frac{\partial^2 T_B}{\partial z^2} \right) = 0 \tag{4.3}$$

### 4.3.2 Boundary Conditions

To establish the boundary conditions, a designation was attributed to each of the tooth rack surfaces and they can be consulted in Figure 4.5.

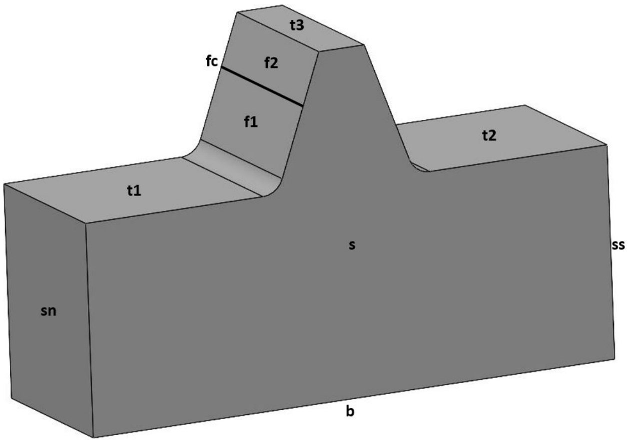

Figure 4.5: Boundary condition surfaces of the heat transfer problem and their designations.

The boundary conditions were defined for each surface and are listed next.

#### 4.3.2.1 Convection Effect

Concerning the case of dry contact in study during this work, the surrounding medium's temperature is considered to be the same as air temperature. On the gear surfaces, s, sn, t2 and t3, the convection effect with the air temperature must be taken into account. The ss surface is simply supported on the hybrid polymer gear tooth base, so is not directly affected by the convection effect. This way, the boundary condition is given by equation 4.4.

$$-k \cdot \left[ \left.\frac{\partial T}{\partial n}\right|_{s} + \left.\frac{\partial T}{\partial n}\right|_{sn} + \left.\frac{\partial T}{\partial n}\right|_{t2} + \left.\frac{\partial T}{\partial n}\right|_{t3} \right] = h_s \cdot (T - T_{Air}) \tag{4.4}$$

In order to determine the heat transfer coefficient, $h_s$, it was assumed the approximation of the tooth surface to a vertical plate subjected to natural convection. The plate's natural convection depends on: the heat transfer regime; the geometry of the plate and its orientation; the air and surface temperature of the plate; physical and thermal properties of the fluid [16]. Applying this assumption on the gear sides, it is possible to obtain the heat transfer coefficient by the equation

4.5. Also, the Rayleigh number needs to be determined, using equation 4.6, and to calculate the Nusselt number, equation 4.7 is used.

$$h_s = \frac{\overline{Nu}_L \cdot k}{L_c} \tag{4.5}$$

$$Ra_L = \frac{g\beta\,(T_s - T_\infty)\,L_c^3}{\nu^2} Pr \tag{4.6}$$

$$\overline{Nu}_L = \left\{0.825 + \frac{0.387 Ra_L^{1/6}}{[1+(0.492/Pr)^{9/16}]^{8/27}}\right\}^2 \tag{4.7}$$

#### 4.3.2.2 Radiation Effect

The radiation effect takes into account the temperature of the load and heat application tool and the emissivity coefficient of the gear material ($\varepsilon$). In this case, there were four surfaces affected by the radiation effect, surfaces sn, f1, f2 and t3, and the respective boundary condition expressions are presented in equations 4.8, 4.9, 4.10 and 4.11. Each boundary condition corresponds to a different temperature, since the surfaces are at different distances from the load and heat application tool (recall Figure 3.10a). As an example, surfaces f1 and f2 are the ones closer to the load and heat application tool, and from the heating source, so the radiation effect has an higher impact for these regions.

$$-k \cdot \left.\frac{\partial T}{\partial n}\right|_{sn} = \varepsilon \cdot \sigma \cdot \left(T_{Tool\_vert\_surf}^4 - T_{Air}^4\right) + h_s \cdot (T - T_{Air}) \tag{4.8}$$

$$-k \cdot \left.\frac{\partial T}{\partial n}\right|_{f1} = \varepsilon \cdot \sigma \cdot \left(T_{Tool\_tip\_round\_surf}^4 - T_{Air}^4\right) + h_s \cdot (T - T_{Air}) \tag{4.9}$$

$$-k \cdot \left.\frac{\partial T}{\partial n}\right|_{f2} = \varepsilon \cdot \sigma \cdot \left(T_{Tool\_tip\_straight\_surf}^4 - T_{Air}^4\right) + h_s \cdot (T - T_{Air}) \tag{4.10}$$

$$-k \cdot \left.\frac{\partial T}{\partial n}\right|_{t3} = \varepsilon \cdot \sigma \cdot \left(T_{Tool\_tip\_straight\_surf}^4 - T_{Air}^4\right) + h_s \cdot (T - T_{Air}) \tag{4.11}$$

#### 4.3.2.3 Contact Temperature

The tooth flank is in direct contact with the load and heat application tool. The tool tip has a curved surface with a specific radius, which makes its contact with the tooth flank being along a line (fc), schematically represented in Figure 4.5. In this case, the boundary condition will ensure an equal temperature along the contact line (fc) as for the tool contact region, and is represented in equation 4.12.

$$T_{fc} = T_{Tool\_contact} \tag{4.12}$$

Other three approximations were performed. First one, the t1 surface is placed very close to the vertical surface of the load and heat application tool during the tests. The distance is slightly less than 1 mm, so t1 surface is considered to have the temperature equal to the average temperature of the vertical surface of the load application tool close to t1, equation 4.13.

$$T_{t1} = T_{Tool\_vert\_surf} \tag{4.13}$$

Also, bottom and supported side surfaces have shown a constant average temperature during the experiments, being assigned to each of the surfaces the respective registered temperature, equations 4.14 and 4.15.

$$T_b = T_{Tooth\_supp} \tag{4.14}$$

$$T_{ss} = T_{Tooth\_base} \tag{4.15}$$

## 4.4 Mechanical Model Definition

After defining the thermal model, considering all the experimental test conditions, it was now necessary to establish the mechanical model. Here, the Hertzian contact theory will be used to explain the contact conditions on the tooth flank and the tooth root bending stress will be presented. Once again, the dovetail section of the tooth rack will not be analysed, and its mechanical impact will be translated into proper mechanical boundary conditions. The addition of section solution would significantly increase the computational time.

### 4.4.1 Hertzian Contact Model

The contact between the teeth of a gear can be approximated to a linear contact and described by the Hertzian contact theory. In the case of this work, this model can be applied to the contact between the load and heat application tool tip and the tooth rack flank, based on some considerations of this theory. Those main hypotheses from this theory are listed next [17]:

- Each body can be approached as an elastic half-space loaded over the small contacting area;
- The dimensions of the contact area must be small compared with the dimensions of each body and with the relative radii of curvature of the surfaces;
- Only normal load is applied between the surfaces, as they are considered friction-less;
- The material behaviour is elastic and isotropic, with small strains, so that Hooke's law is valid;

So, to define the mechanical model, the Hertzian contact model was followed and a contact pressure solution between two cylinders is presented in Figure 4.6. Firstly, in order to obtain the contact pressure, $\sigma_H$, it is necessary to calculate the equivalent radius (equation 4.16), $\rho^*$, which is a function of the curvature radius of the load and heat application tool, $\rho_1$, and of the tooth rack radius, $\rho_2$. Also, the equivalent Young's modulus, $E^*$, is given by equation 4.17, and depends on the material mechanical properties of both surfaces.

$$\rho^* = \left(\frac{1}{\rho_1} + \frac{1}{\rho_2}\right)^{-1} \tag{4.16}$$

$$E^* = \left(\frac{1-\nu_1^2}{E_1} + \frac{1-\nu_2^2}{E_2}\right)^{-1} \tag{4.17}$$

Now, the normal load, $F_n$, must be computed. For this purpose, considering the tangential load, $F_t$, which results from the system weights, plus the own mass of the components that support the load and heat application assembly, it is given by equation 4.18. Since the pressure angle is known by the gear geometric properties definition in section 2.8.1, with equation 4.19 the normal load, $F_n$, is obtained.

$$F_t = m_{total} \cdot g \tag{4.18}$$

$$F_n = \frac{F_t}{cos\alpha_n} \tag{4.19}$$

Lastly, the Hertzian contact pressure results from equation 4.20 and the Hertzian semi-width of the contact area generated is computed by equation 4.21.

$$\sigma_H = \sqrt{\frac{F_n \cdot E^*}{\pi \cdot b \cdot \rho^*}} \tag{4.20}$$

$$a = \frac{\rho^* \cdot \sigma_H}{E^*} \tag{4.21}$$

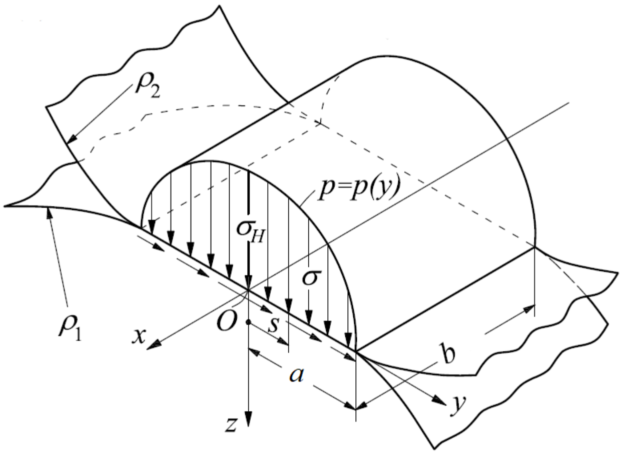

Figure 4.6: Hertzian contact pressure solution for the contact between two cylinders [17].

### 4.4.2 Tooth Root Bending Stress

In the present work, in addition of aiming to validate the FEM models it is also pretended to analyse the tooth root bending stress from them. In particular, it is wanted to determine the tooth root bending stress considering the instant when only a single pair of teeth is in contact during the gear meshing.

In order to calculate it, only the tooth region of the specimen will be considered and the problem is approached as a beam with a built-in end problem, as shown in Figure 4.7.

From the structural mechanics, it is known that the equation to calculate the bending stress for a beam under these conditions, with a constant cross section is given by equation 4.22 [18].

$$\sigma_b = \frac{M_b \cdot y}{I_z} \tag{4.22}$$

Even with the tooth rack having a variable cross section, investigations shown that if its variation is not too extreme, the problem can be solved as a constant cross section problem [18]. Thus, and considering the dimension variables presented in Figure 4.7, the bending stress equation 4.22 can be developed as follows in equation 4.23, using the tangential force calculated in equation 4.18.

$$\sigma_b = \frac{F_t \cdot h \cdot \frac{s_b}{2}}{\frac{b \cdot s_b^3}{12}} \tag{4.23}$$

Working the previous expression, it is obtained equation 4.24.

$$\sigma_b = \frac{6 \cdot F_t \cdot h}{b \cdot s_b^2} \tag{4.24}$$

Now, using the dimensions of Figure 4.7 it is possible to define the tooth base thickness, $s_b = s + 2 \cdot m \cdot tan\alpha$, so it becomes equation 4.25.

$$\sigma_b = \frac{6 \cdot F_t \cdot h}{b \cdot (s + 2 \cdot m \cdot tan\alpha)^2} \tag{4.25}$$

After some equation arrangements it is finally obtained equation 4.26.

$$\sigma_b = \frac{6 \cdot F_t \cdot h}{b \cdot m^2 \cdot \left(\frac{\pi^2}{4} + 2 \cdot \pi \cdot tan\alpha + 4 \cdot (tan\alpha)^2\right)} \tag{4.26}$$

In the ISO 6336-3 [19], the tooth root bending stress equation comes in function of some factors that will be here taken into account and are explained in the following list:

- The form factor, $Y_F$, considers the influence of the tooth form on the nominal tooth root stress;
- The stress correction factor, $Y_S$, allows to convert the nominal tooth root stress to local tooth root stress. It is based in some considerations, for instance, the section change at the fillet radius at tooth root, which causes a stress amplifying effect considered by this factor;
- The stress concentration factor, $Y_T$, is similar to the stress correction factor, but this one considers not the tangential, but the the radial force effect.

Considering the previous factors, the final tooth root bending stress, $\sigma_f$, is computed by equation 4.27.

$$\sigma_f = \frac{F_t}{b \cdot m} \cdot Y_F \cdot Y_S - \sigma_r \cdot Y_T \tag{4.27}$$

For this case, considering equation 4.26, the form factor, $Y_F$, is given by equation 4.28.

$$Y_F = \frac{6 \cdot h}{m \cdot \left(\frac{\pi^2}{4} + 2 \cdot \pi \cdot tan\alpha + 4 \cdot (tan\alpha)^2\right)} \tag{4.28}$$

Consulting the ISO 6336-3 [19], it is possible to obtain, $Y_S$=1.65 and $Y_T$=2, for the current problem. The radial stress is calculated using the radial force, $F_r$, as presented in equation 4.29.

$$\sigma_r = \frac{F_r}{s_b \cdot b} \tag{4.29}$$

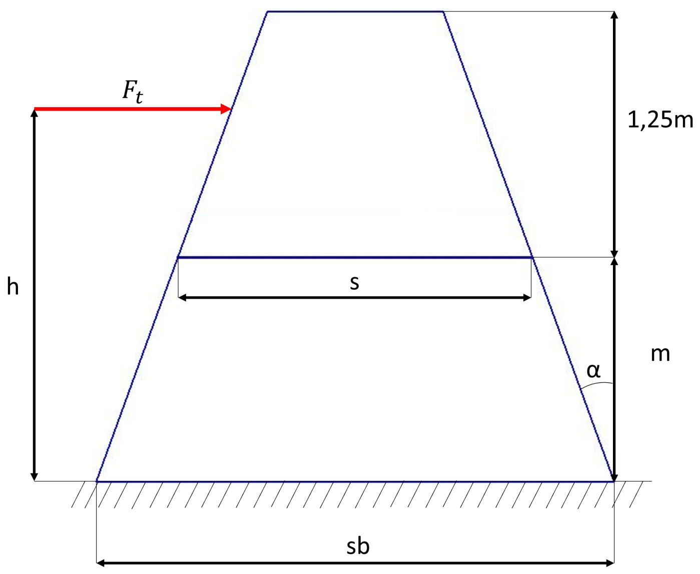

Figure 4.7: Dimensions for the analysis of the tooth root bending stress.

With the bending stress already defined, it is still needed to compute the height, h, for which the gear meshing happens with only a single pair of teeth in contact. This height is computed by equation 4.30, as the pinion and rack geometric properties were already defined in section 2.8.1.

$$h = m + r - r_B \tag{4.30}$$

In order to obtain, $r_B$, equation 4.31 was used.

$$r_B^2 = \sqrt{r_{b_2}^2 + \overline{T_1 B}^2} \tag{4.31}$$

The length $\overline{T_1 B}$=10.438 mm was possible to obtain from KISSsoft software when the analysis of a pinion and wheel was performed in section 2.8.1. The root radius, $r_{b_2}$ is calculated by Equation 4.32.

$$r_{b_2} = r \cdot cos\alpha = \frac{z \cdot m}{2} \cdot cos\alpha = 33.829 \text{ mm} \tag{4.32}$$

Finally, with equations 4.30 and 4.27 it is possible to compute the final tooth root bending stress, $\sigma_f$ =2.391 MPa.

### 4.4.3 Boundary Conditions

The mechanical model boundary conditions were defined taking into account all the tooth rack support designed, which was already described in section 3.3.2. The graphic representation of the boundary conditions can be seen in Figure 4.8.

The tooth rack is simply supported in one of the sides, restricting the vertical movement in the x direction. The dovetail construction restricts the movement of the bottom surface of the rack body. In this case, there is no movement in the y and z directions.

As can be observed in Figure 4.6, the contact pressure distribution is parabolic over the contact width [17] and it is described by equation 4.33.

$$p(y) = \sigma_H \sqrt{1 - \left(\frac{y}{a}\right)^2} \tag{4.33}$$

For the FEM mechanical model, it was implemented this pressure variation, by distributing parabolically the pressure over the constituent mesh elements of the Hertzian width.

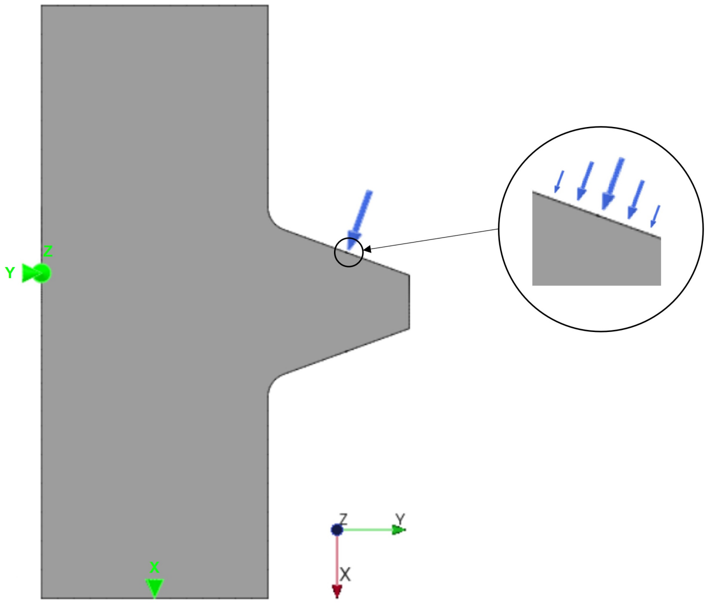

Figure 4.8: Mechanical model boundary conditions.

## 4.5 Thermo-Mechanical Model Definition

Finally, to define the thermo-mechanical model it is necessary to combine both the thermal and the mechanical models, following all the details mentioned in sections 4.3 and 4.4.

In the PrePoMax software, the uncoupled temperature-displacement step was used and this way, the temperature and pressure application on the tooth flank were both taken into account at the same time in the simulations. It is called an uncoupled temperature-displacement step because, firstly performs the thermal analysis for each increment. Only after, the mechanical analysis is performed using the resulting temperature field as a boundary condition for the same increment. This analysis runs faster since the resulting system of equations are smaller, because of the sequential calculations.

## 4.6 Mesh Convergence Study

A convergence study was performed, increasing the number of elements for each simulation. While defining the mesh density, it was intended to define it proportionally to the gear modulus,

$m$, so its density would follow the principle of, $n_M = N \cdot m$. Here, $n_M$ stands for the number of elements used in the mesh, while $N$ represents the coefficient proportional to the gear modulus which defines the final number of elements. In each new mechanical simulation, the $N$ coefficient was increased by 0.5, and the results were compared with the previous simulation. The evolution of the relative differences is presented in Figure 4.9.

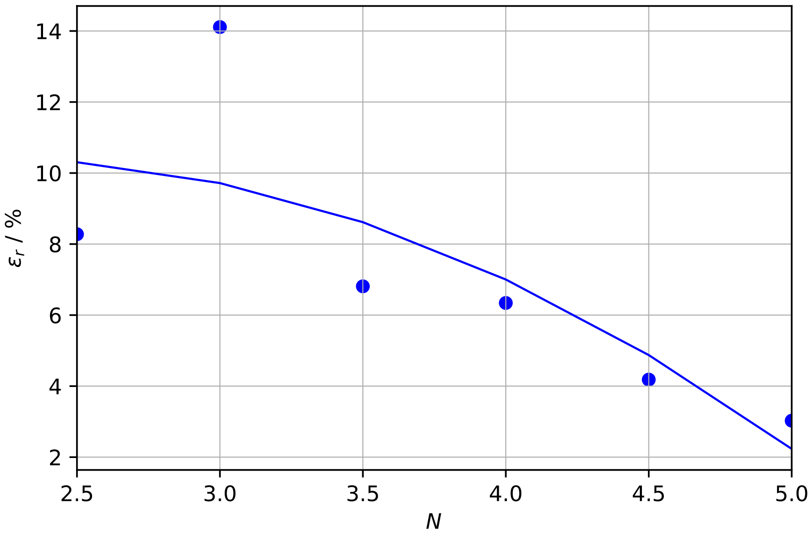

Figure 4.9: Mesh convergence study.

At the end it was concluded that the mesh for $N$=5 and $n_M$=266847 elements, with a relative difference of 3.0267% would be the one to use, since the computational resources were limited and the computational time was already high, about 5632 seconds.

# Chapter 5

# Experimental Procedure

## 5.1 Introduction

Along this section, the experimental procedure will be addressed both for the thermal and for the thermo-mechanical tests.

To obtain the thermal results, a thermal camera FLIR A325 was used, with all the data being recorded in a proper software, the ThermaCam Researcher Pro 2.10. Regarding the thermo-mechanical tests, the DIC technique was applied, using a DSLR D5100 camera to capture the tooth surface images.

The test specimens, for both types of experiments are listed in Tabel 5.1.

Table 5.1: Different thermal test specimens and corresponding designations.

| **Designation** | **Test Specimens** |
|---|---|
| STD | Standard Tooth Rack |
| HT1 | Hybrid Tooth Rack with no Insert |
| HT2 | Hybrid Tooth Rack with an Aluminium Insert |

## 5.2 Thermal Tests

### 5.2.1 Objective and method

The objective of the thermal tests is to validate the hybrid gear concept and also the FEM model developed. For that purpose, the experiments were performed in the three different types of specimens, previously presented in Table 5.1.

Before each thermal experiment there are some steps which need to be controlled and carried out by the user working with the test rig. Those steps must be performed in the following order:

1. The STD and HT1 tooth racks are assembled directly to the test rig. In the case of the HT2 tooth rack, the aluminium insert is prepared and fitted in the tooth rack hollow, and then the specimen is assembled in the test rig;
2. The cartridge heater must be centered inside the housing hole of the load and heat application tool;
3. The contact between the tool tip and the tooth flank must be set in the desired position and the guide should then be locked (using the linear guide locking device);
4. The load is set by placing the necessary weights in the load supporting system;
5. The thermal camera is positioned close to the tooth rack specimen, so it can capture the entire specimen surface and read the temperature at any point of it. The software is also set up;
6. Two type-k thermocouple sensors are also used, one to measure the ambient temperature, and the other to check the temperature measurement by the thermal camera.
7. The power source is turned on but not supplying any power.

In Figure 5.1 is possible to check the thermal test equipment, before the beginning of the experiment.

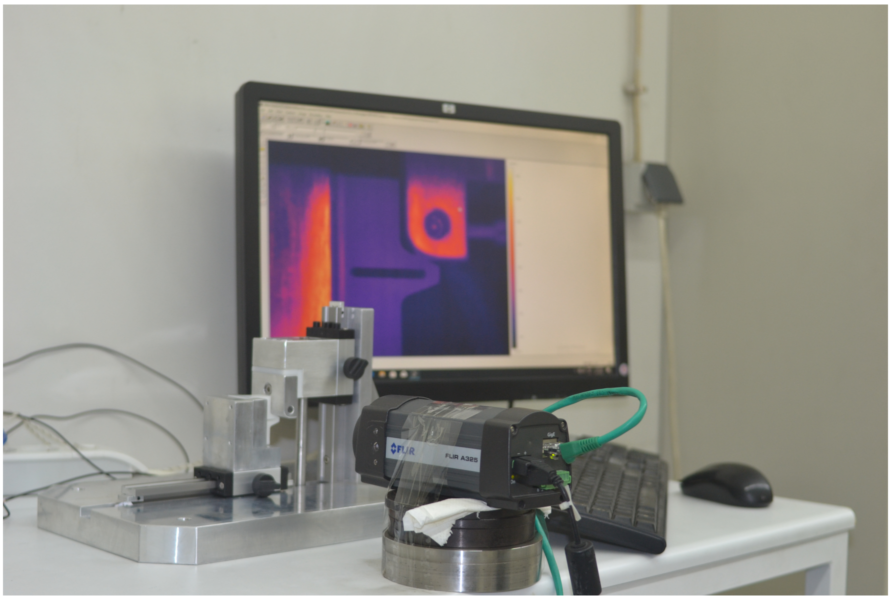

Figure 5.1: Thermal experiment equipment.

To establish the desired tooth flank testing position, a proper tool with a width equal to the necessary distance was used to place the specimen. As mentioned before, for the thermal tests, a thermal camera FLIR A325 was used to measure the surface temperatures, and it is also presented in Figure 5.1. All the data was saved and recorded in real time using the software ThermaCam Researcher Pro 2.10.

To proceed with the test, the following steps must be trailed in the indicated order:

1. The thermal camera software is initialized, as it starts to record the pictures of the surface temperature distribution.

2. The power source starts supplying a predefined power value while the thermocouples are also working. The thermocouples data is saved into a micro SD card, in an excel data sheet format.

After obtaining all the results, Python scripts were created to read and organize the information in a graphical format, as it will be presented in the result analysis section. The main reference points, where there is more interest to analyse the temperature evolution, are presented in Figure 5.2.

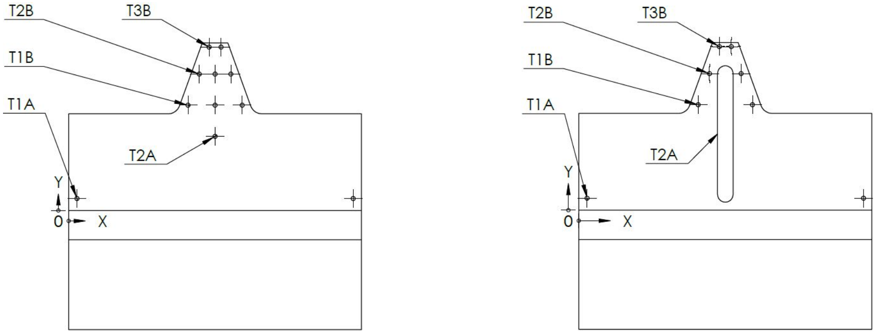

(a) Standard Tooth (b) Hybrid Tooth

Figure 5.2: Critical analysis points for temperature measurements.

#### 5.2.1.1 Assembly of the Aluminium Insert in the Hybrid Tooth Rack Hole

In order to prepare the specimen HT2, the aluminium insert must be assembled in the hybrid tooth cavity. Both the hybrid tooth and its insert technical drawings can be found in Appendix A. To fit the aluminium insert it was necessary to apply some pressure, and when fully fitted, it stands fixed.

In Figure 5.3 it is possible to observe the final configuration of this HT2 specimen.

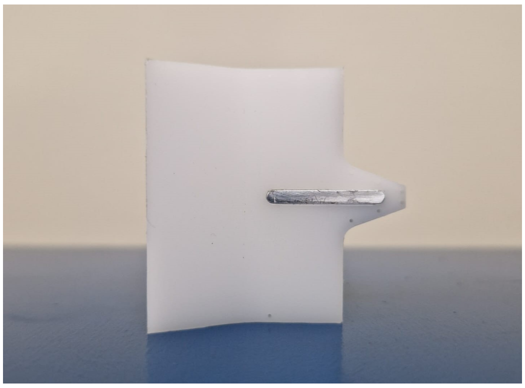

Figure 5.3: Hybrid tooth rack with the insert assembled, HT2.

### 5.2.2 Variables Definition

Once the thermal test method is established, it is now important to understand what are the variables being studied, as well as the definition of each variable to control in the process.

Starting with the applied weights, their value determination was achieved by obtaining the weight of all the parts which directly influence the load application, being those the parts 6, 7, 8, 9 , 10, 16, 26 and 28 attached in Appendix A, and using the formulas presented in section 4.4.1. Without any weighing plates applied, the system itself already weighs, $m_s = 0.769$ kg. In Table 5.2, are presented the mechanical and geometric properties that are used for the Hertzian calculations and which will allow the determination of the final force and consequently, the total weight needed for the experiments.

Table 5.2: Mechanical and geometric properties needed for the Hertzian calculations.

| **Properties for Hertzian Calculations** | |
|---|---|
| b / mm | 14 |
| Pressure angle, $\alpha_n$ / rad | 0.349 |
| $\rho_1$ (POM) / mm | $\infty$ |
| $\rho_2$ (Al) / mm | 7.5 |
| $E_1$ (POM) / GPa | 2.8 |
| $E_2$ (Al) / GPa | 69 |
| $\nu_1$ (POM) / - | 0.386 |
| $\nu_2$ (Al) / - | 0.33 |

Using the properties of Table 5.2 and the equations of section 4.4.1, the final Hertzian parameters can be computed and they are presented in Table 5.3.

Table 5.3: Final Hertzian parameters.

| **Hertzain Theory Parameters** | |
|---|---|
| $\rho^*$ / mm | 7.5 |
| $E^*$ / MPa | 3156.122 |
| $F_t$ / N | 83.409 |
| $F_n$ / N | 88.759 |
| $\sigma_H$ / MPa | 29.142 |
| $m_{total}$ / kg | 8.502 |
| a / mm | 0.138 |

Finally, the mass of the required weights is obtained by equation 5.1.

$$m_w = m_{total} - m_s = 7.733 \text{ kg} \tag{5.1}$$

However, the weights available to conduct the experimental tests had slightly different mass. Therefore, the mass used for all tests was actually, $m_{w,a} = 7.726$ kg.

It is important to recall the static carrying capacity of 4000 N of the vertical carriage, mentioned at the end of the Section 3.3.1. Once it was calculated the $m_{total}$=8.502 kg, it is now understandable that the carriage safely supports the maximum total weight it will be subjected to.

The power required during the tests will be sequentially incremented. The power source has a 50W power and 24V operating voltage. It will be turned on, and as soon as the test starts the power will be regulated to 10%, where it will remain for 30 minutes. After, it is increased to 15% for another 30 minutes and lastly increased to 20% for a further 30 minutes. Then, the power source goes off, and the cooling period starts for 55 minutes, the time it takes for the surface temperature of the tooth rack to cool down. An illustration of the test procedure is shown in Figure 5.4, where the power evolution versus time is graphically represented. With the thermal camera software it was then possible to record the maximum temperatures reached in the heater during the entire test session.

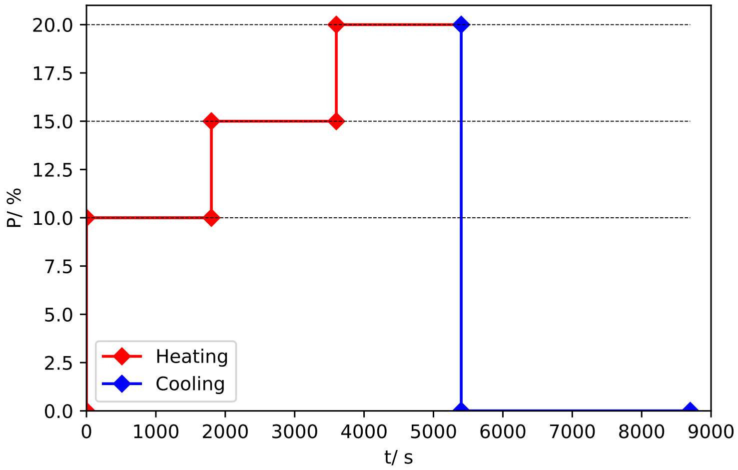

Figure 5.4: Power evolution over time, during a thermal test.

To summarize, the thermal test variables are listed in Table 5.4.

Table 5.4: Thermal experiment variables.

| | Thermal Experiment Variables |
|---|---|
| **Response Variables:** | Surface Temperature of the Tooth, ºC |
| **Fixed Variables:** | Weight of the Load and Heat Application Assembly: 0.769 kg |
| | Weights: 7.726 kg |
| | Gear material: POM |
| | Gear insert, if hybrid: Air or Aluminium |
| | Heating Time: 90 min |
| | Cooling Time: 55 min |
| | Power Range, %: [10, 15, 20] |
| **Independent Variables:** | Ambient Temperature, ºC |

## 5.3 DIC Tests

### 5.3.1 DIC technique

The Digital Image Correlation method, DIC, is a widely used subset-based tool for deformation and shape measurements. This technique consists of tracking the digital images of the specimen surface (the subsets), taken during the experiment, both in the reference and deformed images, so the full displacements field is obtained [20].

For the optimal application, the test specimen must be painted with a speckle pattern as it is one of the conditions which most influences the pixel subset registration accuracy. To create a speckle pattern, specific painting sprays are used, but is difficult to control the spraying distribution on the surface. Generally it is desirable to evenly distribute the speckle pattern, avoiding an excessively dense pattern, and at the same time a pattern barely visible to the naked eye. After the experiment, the displacements are measured making use of a DIC-software [21].

### 5.3.2 Objective and Method

The objective of the DIC tests is to study and validate the displacements on the gear tooth surface and once again, the FEM model developed. As with the thermal tests, the DIC tests were performed for the same three specimens presented in Table 5.1.

The method for the experiment preparation is quite similar to the one implemented for the thermal tests, but with the respective changes starting from the DIC equipment. The DIC test followed the same steps used for the thermal tests as stated in section 5.2.1. Here only the different stages will be added. The following order must be followed to prepare a DIC test:

1. The speckle pattern is applied to the STD and HT1 specimens and then they are assembled in the test rig. In the case of the test specimen HT2, firstly it is needed to proceed with the assembly of the aluminium insert in the tooth rack cavity, described in section 5.2.1.1, and so then the speckle pattern is applied and the specimen assembled in the test rig;
2. Step 2 comprises steps 2 to 4 of the thermal tests, since they are related to the test rig and specimen set up;
3. The DSLR camera is positioned close to the specimen to test, so the entire surface region is captured with the best resolution (number of pixels) possible;

In Figure 5.5, it is possible to see the DIC test set up, before the start of the experiment.

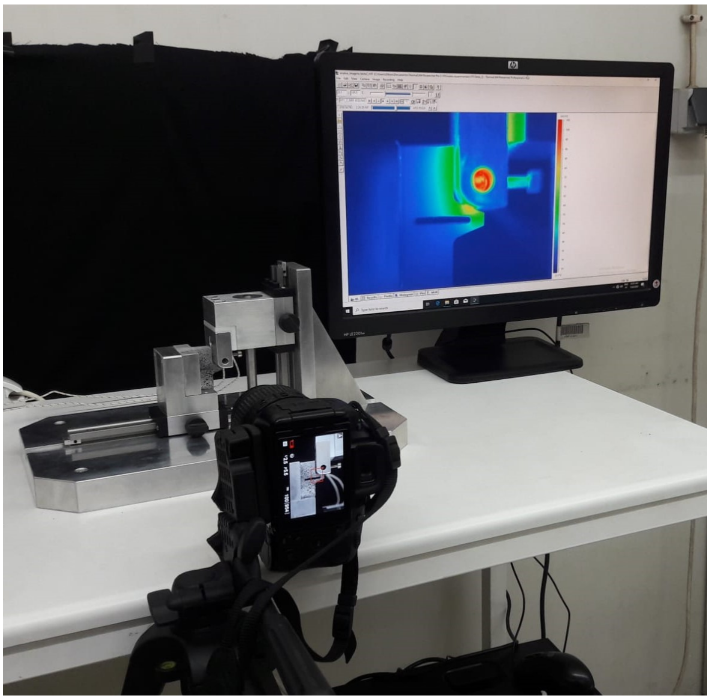

Figure 5.5: DIC experiment set up.

Once every test preparing steps are performed, the experiment may start by turning on the power source for a predefined value. During the test, pictures will be taken every fifteen minutes.

The results are processed in a DIC software, in this case GOM Correlate Pro. After managing all the information, Python scripts to translate all the data into graphical representations were created.

#### 5.3.2.1 Speckle Pattern Preparation

To prepare the speckle pattern, two different sprays were employed. First a Rivelex 200 was applied (Figure 5.6a) to the tooth surface. This first layer is added in order to improve the adhesion of the speckle pattern to the surface. After waiting for a few minutes for the spray to dry, another LUX matt black (Figure 5.6b) spray is used to create the speckle as can be seen in the example of Figure 5.7, for the standard (STD) and the hybrid tooth with the aluminium insert (HT2).

(a) Rivelex 200 (b) Luxens matt black

Figure 5.6: Sprays used to create the speckle pattern on the tooth rack surface.

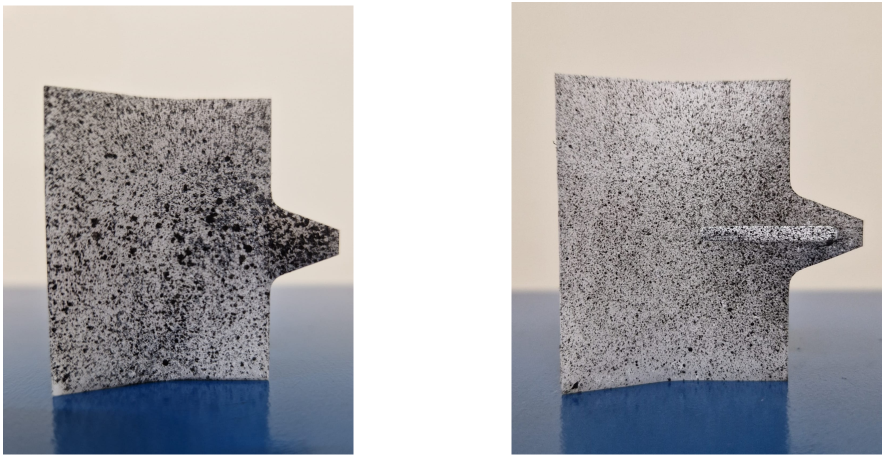

(a) STD (b) HT2

Figure 5.7: STD and HT2 specimens with the speckle pattern applied for the DIC tests.

### 5.3.3 Variables Definition

The DIC tests have in consideration the same variables as for the thermal tests. This way, every DIC test is performed with an applied weight of, $m_{w,a} = 7.726$ kg.

Regarding the power stages, at the beginning of the experiment the power source is turned on and as soon as the timer is initiated, the power is set to 10% starting the heating period, and the value stands for 30 minutes. Then, the power is increased to 15% for 30 minutes more, and afterwards, the value is increased to 20% for the final 30 minutes of the heating phase. Immediately after this period, the power source goes off to 0% and the cooling phase is initiated and extended for 55 minutes.

The DIC test variables are concisely listed in Table 5.5.

Table 5.5: DIC experiment variables.

| | **DIC Experiment Variables** |
|---|---|
| **Response Variables:** | Surface Temperature of the Tooth, ºC |
| **Fixed Variables:** | Mass of the Load and Heat Application Assembly: 0.769 kg |
| | Mass of the Weights: 7.726 kg |
| | Gear material: POM |
| | Gear insert, if hybrid: Air or Aluminium |
| | Heating Time: 90 min |
| | Cooling Time: 55 min |
| | Power Range, %: [10, 15, 20] |
| **Independent Variables:** | Ambient Temperature, ºC |

# Chapter 6

# Experimental and Numerical Results

## 6.1 Introduction

In this chapter the experimental results will be presented and compared with the FEM models developed.

Firstly, the thermal tests will be addressed starting by analysing the evolution of the points already presented in Figure 5.2, and then the entire temperature field will be compared to the FEM thermal model. For the thermo-mechanical experiments, the DIC results, after processed in the DIC software and translated by the Python scripts, will be presented and also compared with the respective FEM model.

## 6.2 Thermal Experimental Results

For the thermal results, there was an evident variation on the evolution of the temperature values among the tested specimens. That difference was most notorious for the hybrid tooth rack with the aluminium insert, HT2, when compared to the others, particularly the STD specimen.

Before proceeding to the temperature analysis it is necessary to take into consideration that each experiment had a different ambient temperature, which directly influences the final results. Thus, it was adopted a stabilized temperature concept, which subtracts the registered temperatures to the average ambient temperature registered during the corresponding test, equation 6.1.

$$T_{stabilized} = T - T_{amb} \tag{6.1}$$

The average ambient temperature registered during each specimen test is shown next:

- **STD:** 24.7 °C
- **HT1:** 25.3 °C
- **HT2:** 25.3 °C

Now, according to Figure 5.2, the temperature evolution of each point versus the maximum temperature registered in the heater, will be shown. The entire test evolution of the stabilized temperatures over the time for each point can be consulted in Appendix B, as here the interest is placed in the heating phase.

Starting with point T3B at the addendum region of the tooth, Figure 6.1 shows the stabilized temperatures evolution for all test specimens. At this point, the temperature is affected not only by the heating source, but also for the radiation coming from the tip of the load and heat application tool. As it is possible to observe, HT2 reached the lowest temperatures for each heating stage, while HT1 and STD have progressed with close values, but still with STD presenting higher temperatures.

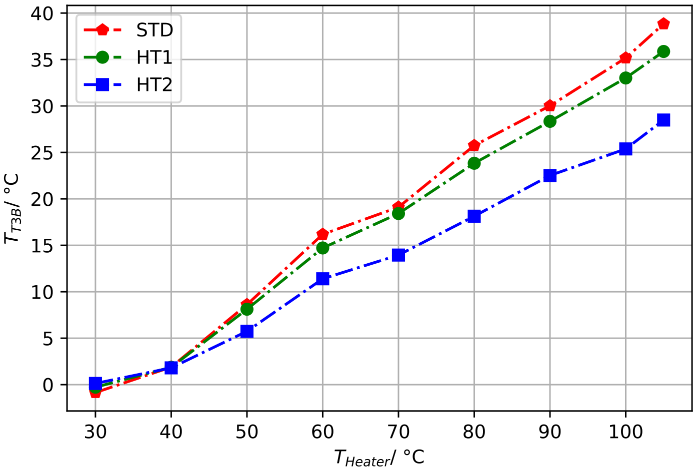

Figure 6.1: Stabilized temperature evolution of point T3B with heater temperature, during the heating phase.

In Figure 6.2, the point T2B is under analysis, a point which is quite close to the point of contact between the tooth flank and the load and heat application tool, so the temperature increase is mainly affected by the heating source. Once again, HT2 stands out for having a notorious progression with lower values than the other specimens. STD and HT1 evolution is almost overlapping, indicating that the hybrid tooth with no insert (air) does not improve the temperature behaviour in the critical contact region, compared with the standard tooth.

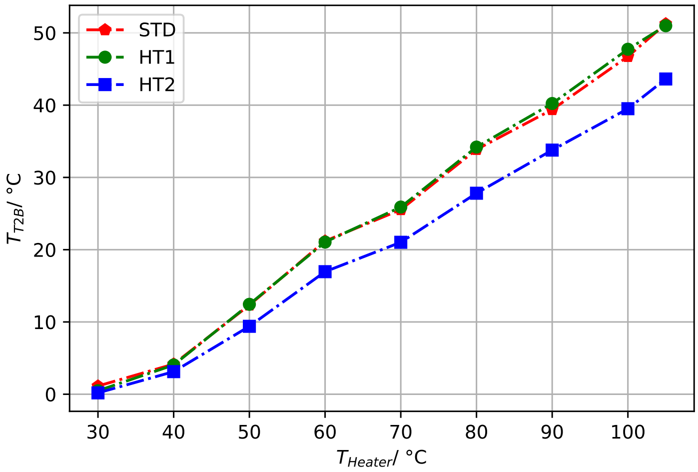

Figure 6.2: Stabilized temperature evolution of point T2B with heater temperature, during the heating phase.

Regarding point T1B, it is located at the tooth root region and has a direct influence of the radiation coming from the application tool, besides the heating source effect (just as in T3B point). Its stabilized temperature can be seen in Figure 6.3, where HT1 was the specimen with the highest temperatures registered almost during the entire heating phase, followed by STD and then HT2 presenting once more the lowest values.

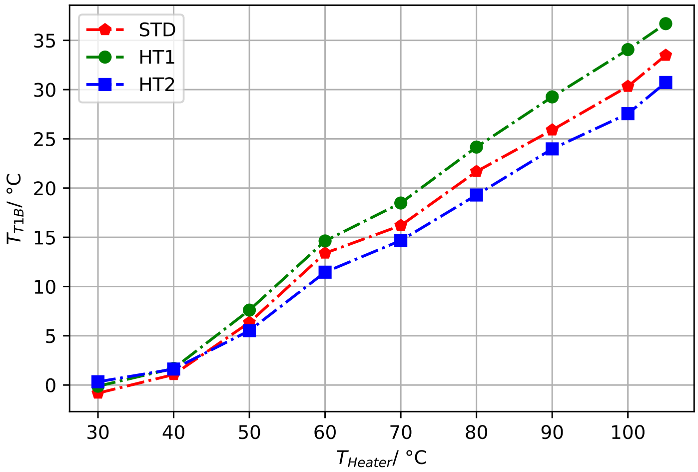

Figure 6.3: Stabilized temperature evolution of point T1B with heater temperature, during the heating phase.

The point T2A is located close to the insert region and analysing Figure 6.4, this occasion HT2 is not the specimen with the lowest temperatures, but STD. HT2 starts with the highest temperatures, until the maximum temperature of the heater reaches 50 °C, then HT1 assumes this condition.

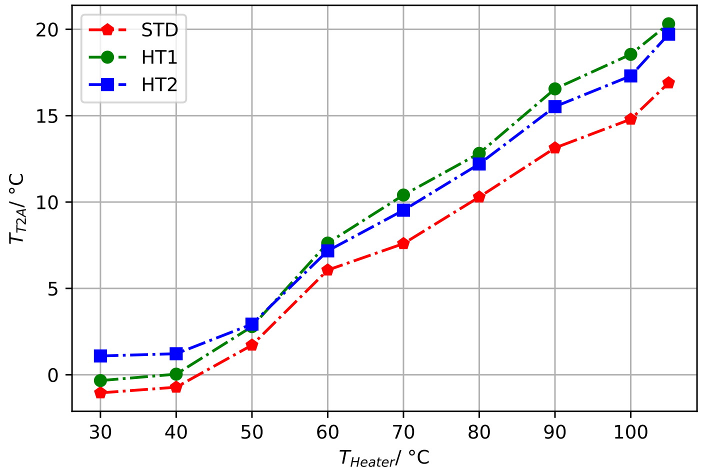

Figure 6.4: Stabilized temperature evolution of point T2A with heater temperature, during the heating phase.

Finally, T1A point informs of the temperature at the bottom region of the rack body, where the convection effect influences its result. In Figure 6.5, STD is presented as the tooth with the lowest temperatures during the entire heating period, a similar behaviour to the one observed for point T2A. HT2 has the highest stabilized temperature values until the maximum temperature of the heater reaches 80 °C, moment from which HT1 registers higher values. However, by the end of the heating phase, the HT2 specimen obtains the highest temperature among all the teeth.

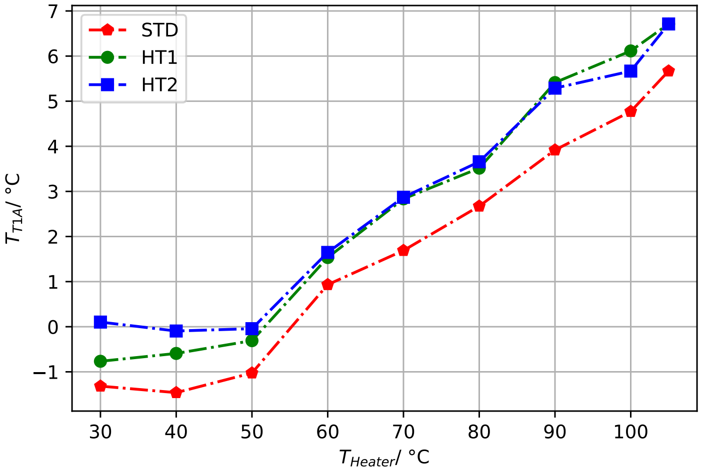

Figure 6.5: Stabilized temperature evolution of point T1A with heater temperature, during the heating phase.

At the end, it is of interest to notice that the aluminium insert (HT2) effect was visible in the tooth tip, contact and root regions. It resulted in the lowest temperatures registered among all the specimens. As an example, differences of approximately less 10 °C in the tooth tip, comparing to the STD, when the heater temperature reached the maximum value. In the rack body the effect of the insert was reverse. For the points in this region, the heating evacuation through the insert raised its own temperature, which was distributed along the rack body. That is the reason for the slightly higher temperature of HT2 specimen compared to the STD tooth rack in these regions, 16.63 % higher in the insert point, and 18.34 % higher at the bottom. All the temperature values can be consulted in Table 6.1, where it possible to find the comparison of the temperatures among all the tested specimens for a heater temperature of 105 °C, when the conditions are the most extreme during the testing period.

Table 6.1: Temperature differences for all the points under analysis and for all the tested specimens, for a heater temperature of 105 °C.

|  | $T_{STD}$ | $T_{HT1}$ | $\%_{HT1}$ | $T_{HT2}$ | $\%_{HT2}$ |
|---|---|---|---|---|---|
| T3B | 38.84 | 35.86 | -7.67 | 28.48 | -26.67 |
| T2B | 51.26 | 50.99 | -0.53 | 43.62 | -14.90 |
| T1B | 33.48 | 36.70 | 9.62 | 30.72 | -8.24 |
| T2A | 16.90 | 20.32 | 20.24 | 19.71 | 16.63 |
| T1A | 5.67 | 6.71 | 18.34 | 6.71 | 18.34 |

### 6.2.1 Thermal Results versus FEM Thermal Model Results

Once the thermal experimental results were presented, it is now important to understand if the FEM thermal model developed is in line with what happens in the real case. To perform this comparison, the same moment of the heating period must be considered. Therefore, the instant at which the highest temperature of the heater was registered was chosen and those conditions were applied to the FEM model. This time, the stabilized temperature concept is not needed as the FEM model uses the same ambient temperature registered during the experiments.

As a remark, since the thermal camera software had the setting to pick a very small area in the thermal image and obtain among the minimum, average and maximum temperature registered at that region, the average temperatures were the ones considered for the comparison, hence the designation of $T_{avg}$ for the experimental results. A small area was used instead the point feature, because getting only a point value, in the case a pixel value, could lead to less precision in the final results. The software would identify area regions with the label "*AR*" and a corresponding number, as can be seen in Figure 6.6. These labels could then be modified.

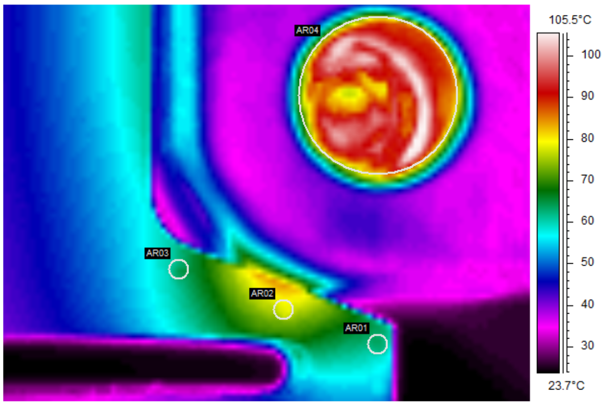

Figure 6.6: Example of the use of the area feature instead of the point one, to obtain the temperature data.

#### 6.2.1.1 STD Thermal Comparison

For the STD specimen, in Table 6.2 is possible to find the temperatures values for every point under analysis (recall Figure 5.2), both for the FEM, $T_{FEM}$, and for the experimental results, $T_{avg}$, as well as the corresponding relative error, $\varepsilon_r$. The point with the highest relative error was T2B, which corresponds to the contact region point, with 9.80 %. In the FEM model, the heating source conditions were replied by applying a temperature value in the entire Hertzian surface, that value being equal to the maximum temperature obtained not in T2B, but in the exact contact edge. This methodology was implemented for all cases. Such an high relative error can be in part explained by the surface finish of the load and heat application tool not being in accordance with the specified in the technical drawings. Therefore, its tip radius was a little affected which lead to a slightly larger contact area and so higher temperatures were reached. The point close to the insert region (T2A) also presented a relative error of 8.53 %.

Overall, the FEM model has shown satisfactory results, such as in the tooth addendum region, the tooth root and the rack body points, T3B, T1B and T1A, respectively. All of them presented relative errors lower than 4.2 %, approximately. The minimum relative error was registered for the tooth addendum point (T3B) with 0.03 %.

Table 6.2: Comparison between the FEM model and the thermal experiment results, of the temperatures registered at the points under study for the STD.

| | **STD** | | |
|---|---|---|---|
| | $T_{FEM}/°C$ | $T_{avg}/°C$ | $\varepsilon_r/\%$ |
| T3B | 61.78 | 61.80 | 0.03 |
| T2B | 67.02 | 74.30 | 9.80 |
| T1B | 54.83 | 57.20 | 4.14 |
| T2A | 45.15 | 41.60 | 8.53 |
| T1A | 30.37 | 30.40 | 0.10 |

To understand the temperature behaviour along the tooth rack, a temperature analysis was performed over a line along the x and y axis, Figure 6.7, for the experimental and FEM results. In the x axis direction it was chosen a height of y=13.22 mm, which corresponds to half of the total height of the tooth rack (disregarding the dovetail connection). For the y axis direction, it was chosen an analysis over a line for x =21.21 mm, which corresponds approximately to half of the rack length.

For the x direction, Figure 6.7a, with y=13.22 mm, the temperature shows an identical evolution for both cases, but with an offset that is reduced over the distance covered. The FEM temperatures are higher, except near the supported tooth rack side, where the values are slightly lower.

Regarding the y direction, Figure 6.7b, with x=21.21 mm, again the temperature distributions are similar. The FEM model presents higher values for intermediate regions, or the insert region, something already verified and compatible with what analysed for the T2A point. In the tooth region, the thermal tests temperatures overtake the FEM temperatures, something that also happened when the tooth region points were checked.

In Figure 6.8, are presented the thermal camera image results and the FEM results, both with the same temperature scale range and colour map for a better comparison.

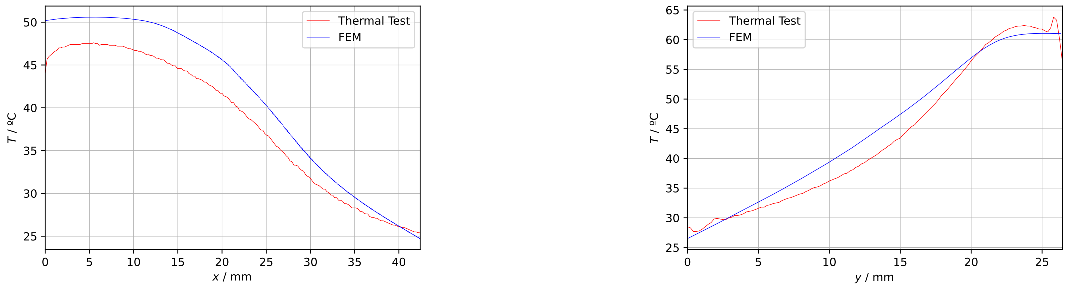

(a) x axis direction, for y=13.22 mm.

(b) y axis direction, for x=21.21 mm.

Figure 6.7: STD thermal test and FEM results over a line.

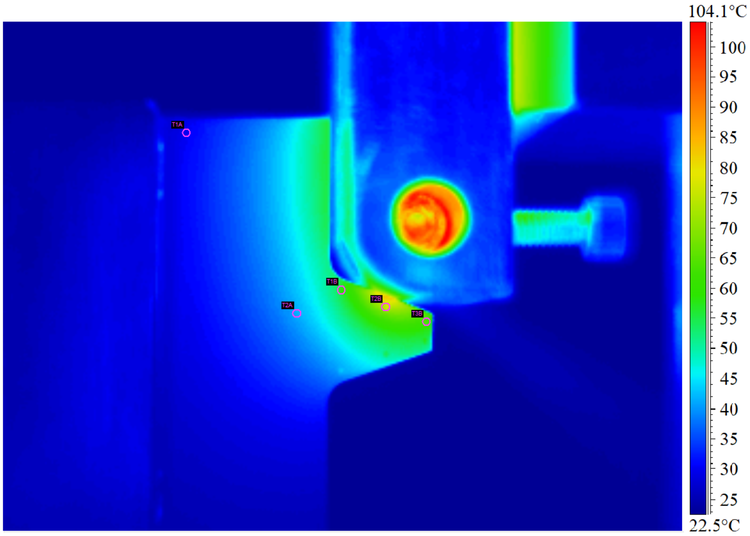

(a) Thermal test

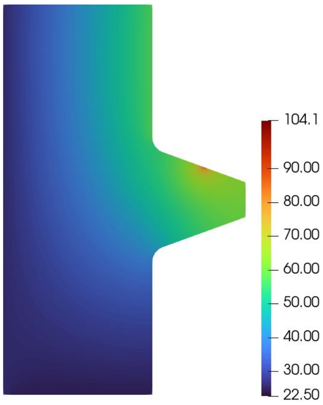

(b) FEM

Figure 6.8: Thermal test temperature results vs FEM temperature results, for STD.

#### 6.2.1.2 HT1 Thermal Comparison

For the HT1 tooth, the highest relative errors came for the contact region point (T2B) and for the insert region point (T2A), with the values of 8.27 % and 15.62 %, respectively, as stated in Table 6.3. All the other points obtained relative errors below 1.5 %, approximately. The minimum value registered was 0.32 %, again for the tooth addendum point (T3A).

Table 6.3: Comparison between the FEM model and the thermal experiment results, of the temperatures registered at the points under study for the HT1.

| | **HT1** | | |
|---|---|---|---|
| | $T_{FEM}/°C$ | $T_{avg}/°C$ | $\varepsilon_r/\%$ |
| T3B | 61.50 | 61.70 | 0.32 |
| T2B | 70.63 | 77.00 | 8.27 |
| T1B | 62.07 | 63.00 | 1.48 |
| T2A | 52.84 | 45.70 | 15.62 |
| T1A | 32.93 | 32.60 | 1.01 |

The temperature distribution over a line along the x and y directions is translated into a graphical format in Figure 6.9. Once again, in the x axis direction it was chosen a height of y=13.22 mm, being half of the total height of the tooth rack (disregarding the dovetail connection). However, this time for the y axis direction, it was chosen an analysis over a line for x=19.71 mm, so the line does not overlap the insert region, but is located immediately next to it.

Starting with the x axis direction, Figure 6.9a, for y=13.22 mm, the FEM temperature progress follows the trend of the thermal test results, with the FEM model reaching higher temperatures from the not supported rack side (x=0 mm), until the insert hole region. From the insert hole to the tooth rack supported side (x=42.41 mm), the FEM model follows the test values with small differences, but with the test results being higher this time.

In y direction, for x=19.71 mm, Figure 6.9b, the FEM model shows an almost linear evolution during the rack body height, with this behaviour changing completely for the tooth region, more precisely, for the regions closely affected by heat from the contact region. In the rack body height, the FEM results are almost ever higher than the thermal test temperatures and with a visible difference, already proven by the relative error shown for the insert region point (T2A). Again, when entering the tooth region, the most affected by the heating source, the FEM model temperatures are lower than the experimental results, mainly close to the contact region where the difference is higher as proven by the relative error obtained for the T2B point and observed at the final stage of the plot representation.

In Figure 6.10, an image taken by the thermal camera, for the maximum heater temperature value obtained during the test is compared with the FEM model result.

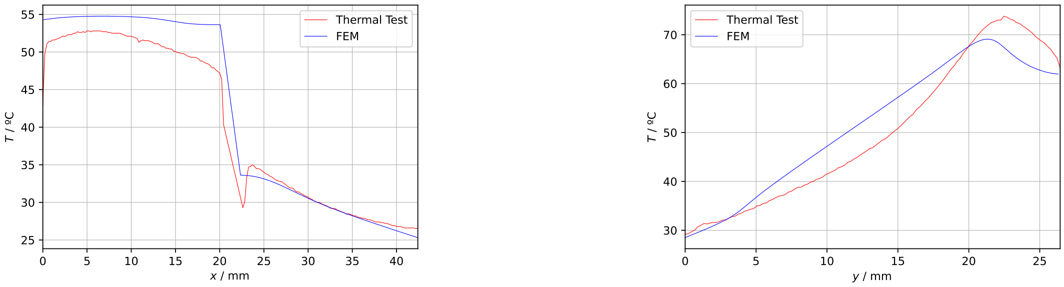

(a) x axis direction, for y=13.22 mm.

(b) y axis direction, for x=19.71 mm.

Figure 6.9: HT1 thermal test and FEM results over a line.

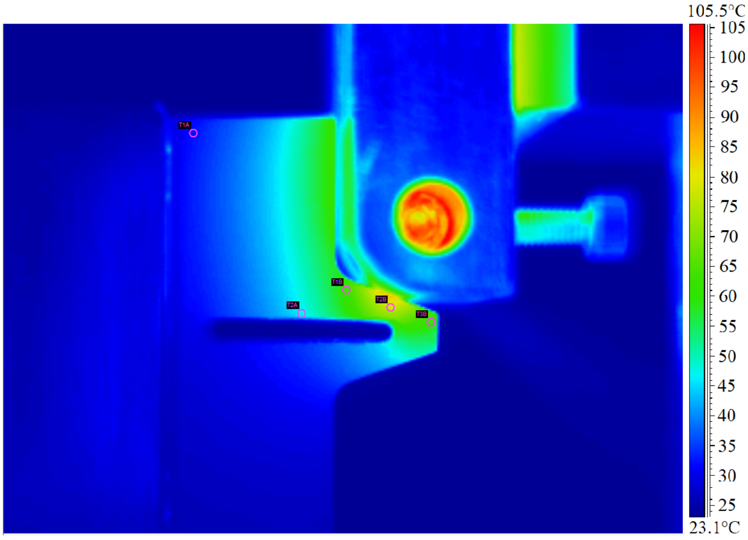

(a) Thermal test

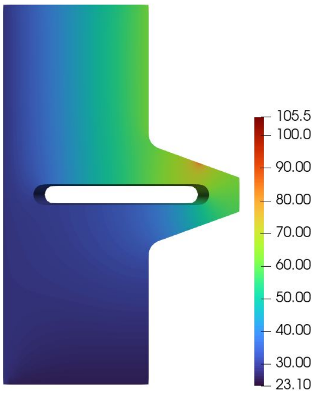

(b) FEM

Figure 6.10: Thermal test temperature results vs FEM temperature results, for HT1.

#### 6.2.1.3 HT2 Thermal Comparison

The HT2 specimen was the one which acquired the highest relative errors, Table 6.4. The three points that belong to the tooth meshing region obtained between 12.56 % and 17.90 %, approximately, being the highest value obtained in the contact region point (T2B) with 17.90 %. The minimum relative error was 2.81 % for the tooth rack body point (T1A). Here, it is also important to highlight that the point located at the tooth addendum region (T3B) is the one that most increased the relative error value compared to the other specimens. For STD and HT1, the values were equal or less than 0.32 %, and for HT2 the value raised to almost 12.56 %, approximately.

Table 6.4: Comparison between the FEM model and the thermal experiment results, of the temperatures registered at the points under study for the HT2.

| | **HT2** | | |
|---|---|---|---|
| | $T_{FEM}/°C$ | $T_{avg}/°C$ | $\varepsilon_r/\%$ |
| T3B | 46.52 | 53.20 | 12.56 |
| T2B | 52.87 | 64.40 | 17.90 |
| T1B | 47.96 | 55.60 | 13.74 |
| T2A | 43.11 | 45.70 | 5.67 |
| T1A | 33.31 | 32.40 | 2.81 |

In Figure 6.11, it is possible to find the representation of the temperatures over a line for the x and y direction, for the HT2 specimen. As in the case of HT1 specimen, for HT2 it was chosen a height of y=13.22 mm for the x axis direction, corresponding to half of the total height of the tooth rack (disregarding the dovetail connection). For the y axis direction, it was performed an analysis over a line for x=19.71 mm, for the inspection line do not overlap the insert region, but for it to be located immediately next to that region.

For the x axis direction, with y=13.22 mm, Figure 6.11a, the FEM model is a good approximation to the experiment performed, except in the insert region itself. As in the case of the HT1, here the FEM model has higher temperatures from the not supported side (x=0 mm) of the tooth, until the regions close to the insert and with a similar evolution. However, in the insert region itself and for distances close to it, the FEM model has the highest temperature difference registered in the plot. Just as in the previous case, after the insert region down to the supported side of the rack (x=42.41 mm), the thermal test values are close, but slightly higher than the FEM ones.

Concerning the y axis direction, for x=19.71 mm, Figure 6.11b, from the bottom of the tooth rack (y=0 mm) up to the beginning of the tooth region (y=16.19 mm), the progression of the FEM model is very close to the thermal results, but with an offset. Recalling the insert point, for y=13.22 mm (T2A), the relative error of 5.67 % can be used as a reference for the deviation of the results from the thermal values. From the insert region, to the tooth tip (y=26.44 mm), the FEM model starts to depart from the thermal results and consequently, the errors for the tooth meshing region are higher, as stated before when discussing the T1B, T2B and T3B points which belong to that area.

Once again, the thermal image was compared to the FEM result, both presented in Figure 6.12.

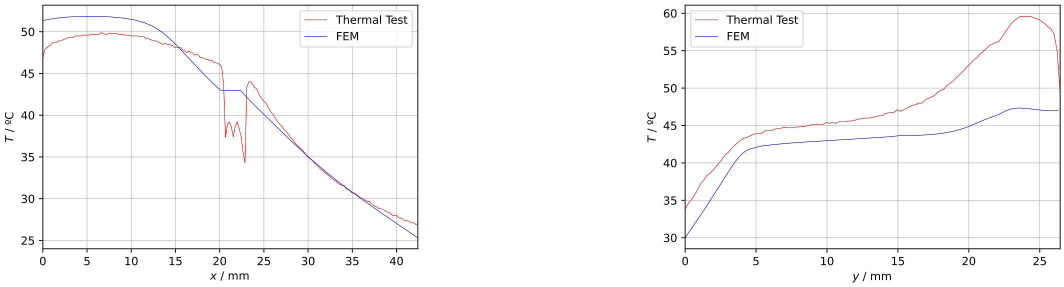

(a) x axis direction, for y= 13.22mm.

(b) y axis direction, for x= 19.71mm.

Figure 6.11: HT2 thermal test and FEM results over a line.

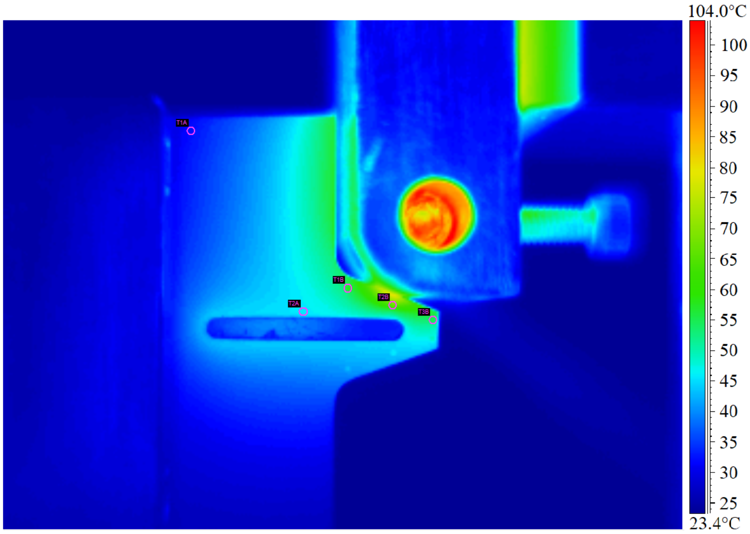

(a) Thermal test

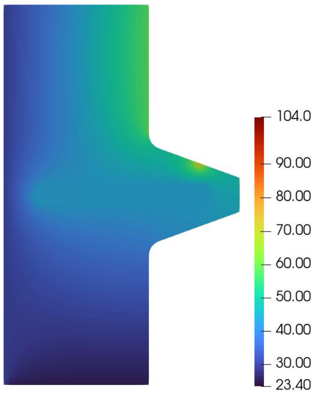

(b) FEM

Figure 6.12: Thermal test temperature results vs FEM temperature results, for HT2.

## 6.3 Thermo-Mechanical Experimental Results

In this section, the colour maps for the x and y displacements will be presented, as well as the maximum values obtained for each case. The interest here is to analyse the DIC results for the stage where the thermal expansion is the highest, and so the final moment of the heating period was chosen to study. To remember, the final stage of the heating phase goes from the 60 minutes up to the 90 minutes of test, with the power source supplying a power of 20 %, and pictures are taken every 15 minutes since the very beginning of the experiment. That being said, the analysis for the 3 specimens will be performed for the picture taken in the minute 90, right before the cooling period starts.

### 6.3.1 STD DIC Results

For the STD specimen, the maximum displacements obtained were of -0.0854 mm and -0.0887 mm, for x and y directions, respectively.

The maximum x displacement point is highlighted in Figure 6.13, where all the x displacement field of the STD specimen is presented. This point is located in the not supported side of the tooth rack for a height equal to the rack body height, so with the coordinates x=0 mm and y=16.19 mm. However, the tooth tip, at the flank side opposite to the one where the load was applied, also exhibits displacements close to the maximum, but in the positive direction.

In Figure 6.14 it also is indicated the maximum displacement in y direction, this being located at the supported tooth rack side (x=42.41 mm).

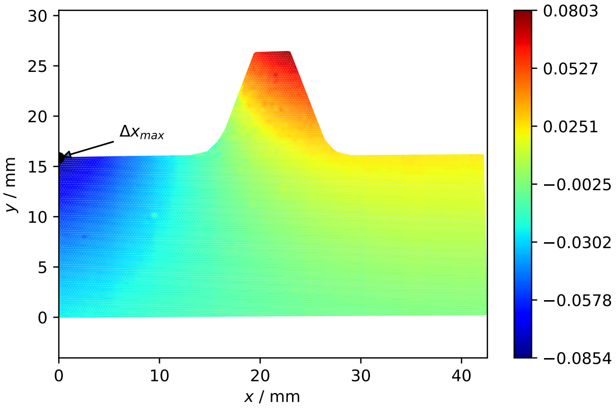

Figure 6.13: STD displacements in x direction, for the maximum heater temperature reached during the test.

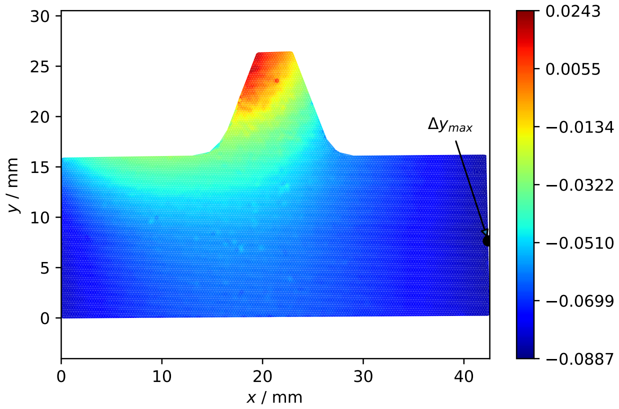

Figure 6.14: STD displacements in y direction, for the maximum heater temperature reached during the test.

### 6.3.2 HT1 DIC Results

Regarding the HT1 tooth rack, the maximum x and y displacements are 0.1122 mm and 0.0750 mm, respectively.

For the x displacement, this point is situated in the tooth tip apex, in the flank tooth side where the load is not applied, Figure 6.15. Remembering that for the STD specimen, this was also a region with values close to the highest displacements registered.

In the y displacements, the maximum is located in the opposite tooth flank, in the tooth tip apex, as seen in Figure 6.16. The thermal expansion effect is clearly noticeable as the tooth tip region expands in the positive y axis direction.

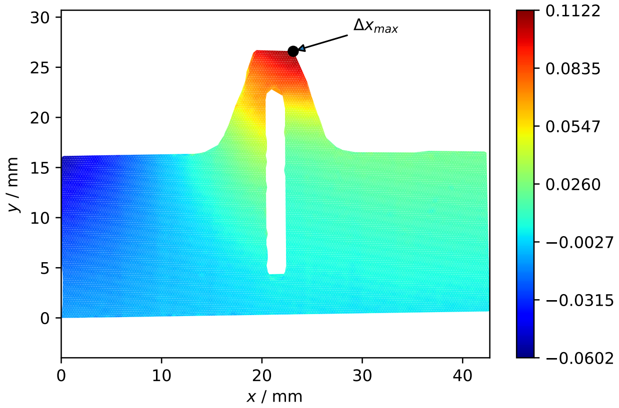

Figure 6.15: HT1 displacements in x direction, for the maximum heater temperature reached during the test.

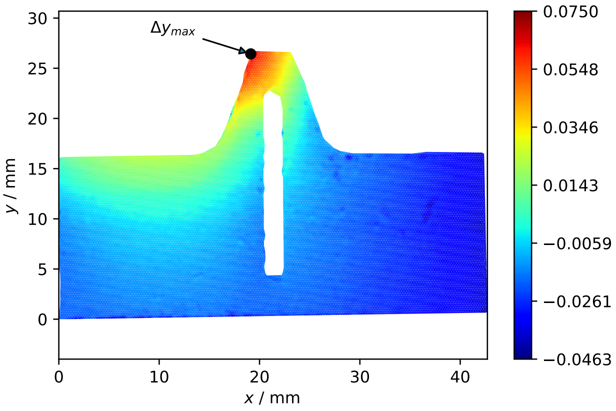

Figure 6.16: HT1 displacements in y direction, for the maximum heater temperature reached during the test.

### 6.3.3 HT2 DIC Results

The HT2 tooth rack obtained -0.1936 mm as the maximum x displacement value, and -0.1335 mm as the maximum y displacement value.

The place where the maximum x displacement is located at is the same as in the STD case, so in the top of the rack body, in the not supported side, Figure 6.17. Since this region is not restricted with physical boundary conditions, the thermal expansion effect promotes its highest displacement in the negative direction of the x axis.

Regarding the y maximum displacement point, it is in the not supported side, just like the x displacement, but close to the bottom of the rack, Figure 6.18. This displacement distribution is also affected by the aluminium insert which offers resistance to the POM thermal expansion and also helps with the heat evacuation as previously analysed.

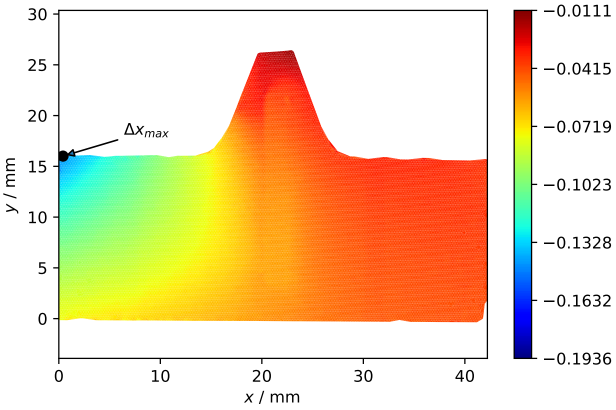

Figure 6.17: HT2 displacements in x direction, for the maximum heater temperature reached during the test.

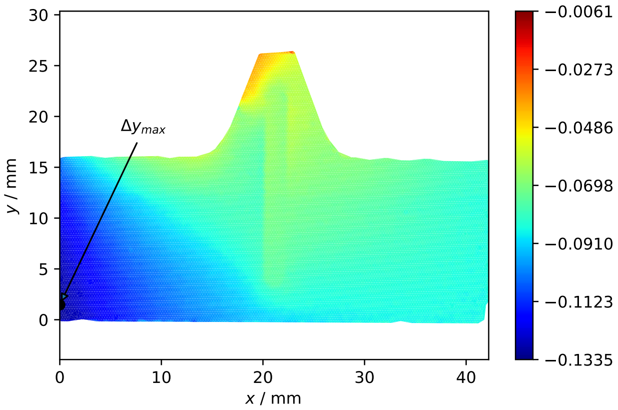

Figure 6.18: HT2 displacements in y direction, for the maximum heater temperature reached during the test.

### 6.3.4 DIC Results versus FEM Thermo-Mechanical Model Results.

A comparison between DIC results and the FEM thermo-mechanical results will be performed in the next sections, for all the three tested specimens. To proceed with the analysis, the rack body displacements will be analysed over a line in the bottom length direction, for an height that includes the insert region. Also, an over a line study will be done along the tooth rack height, for a region that covers the insert proximity. The entire x and y displacement field is also compared with the FEM model.

All the information was processed in a DIC software and then collected and summarised into python scripts, which translated all the following results.

Once the FEM thermo-mechanical model is validated, the tooth root bending stress will also be compared with the theoretical result.

#### 6.3.4.1 STD Thermo-Mechanical Comparison

Starting with the STD specimen, its displacement values in the x axis direction for y=13.22 mm are represented in Figure 6.19a. As possible to check, at the initial stage, the FEM model obtained similar values to the ones registered in the DIC experiment. However, as the length distance in study gets closer to the supported side of the tooth (x=42.41 mm), the FEM results are lower than the DIC ones, and an increase of the distance between the values is observed.

Concerning the y displacements, for x=21.21 mm, Figure 6.19b, the graphical evolution of the FEM model is identical to the DIC one, but with an offset difference along the entire distance.

Overall, the FEM model predicted accurately the displacements in both directions, but with an offset. The displacement fields for both directions are next compared in Figure 6.20 for the x displacements, and in Figure 6.21 for y displacements. The similar displacement field in both directions suggest that the boundary conditions defined for the mechanical model were accurate.

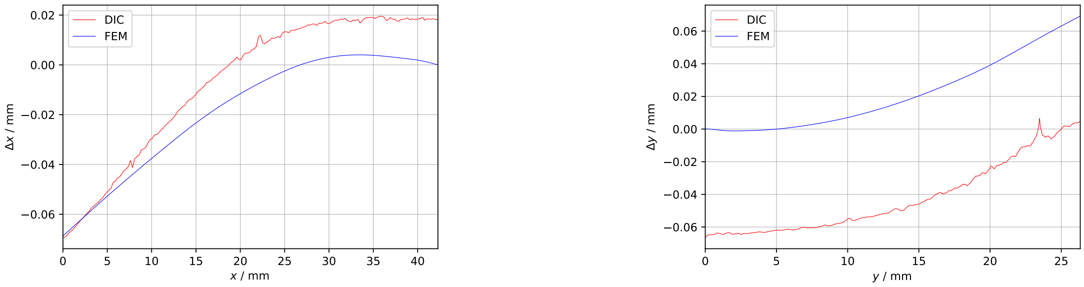

(a) STD displacements along x axis direction, for y=13.22 mm.

(b) STD displacements along y axis direction, for x=21.21 mm.

Figure 6.19: STD displacements plotted for the over a line analysis, both in x and y directions.

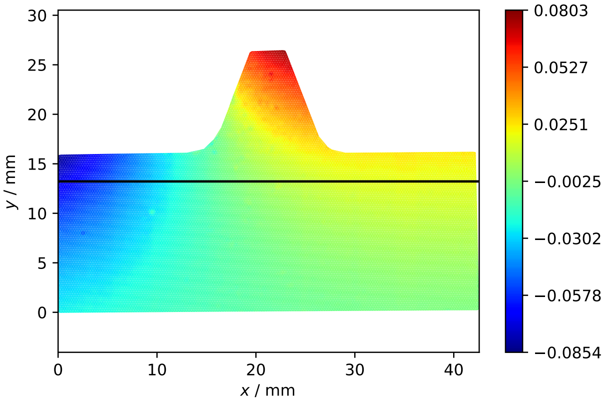

(a) DIC

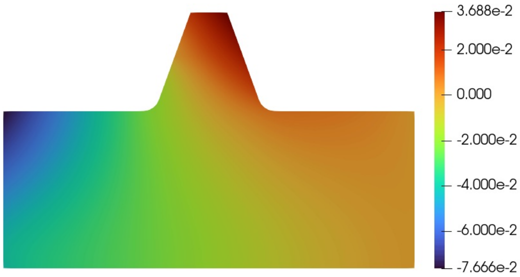

(b) FEM

Figure 6.20: STD displacements along x axis direction, for y=13.22 mm.

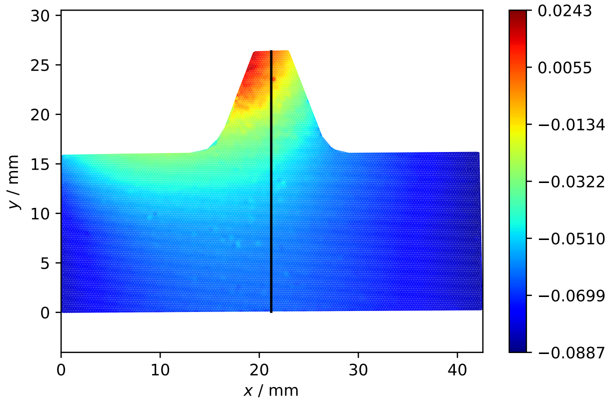

(a) DIC

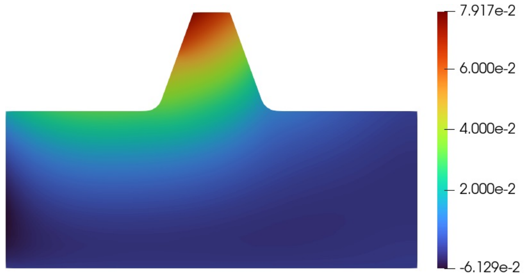

(b) FEM

Figure 6.21: STD displacements along y axis direction, for x=21.21 mm.

### 6.3.4.2 HT1 Thermo-Mechanical Comparison

For the HT1 tooth rack, the x displacements over a line for y=13.22 mm, are presented in Figure 6.22a. In this case, the FEM progression along the rack body length is similar to the DIC results. Once again, there is an offset between the plots, that increases in the region that goes from the insert region until the supported side of the tooth rack (x=42.41 mm), while form the not supported side (x=0 mm), to the insert region that offset is lower.

The y displacements for x=19.71 mm are shown in Figure 6.22b. There keeps being an offset between the graphical representations, but the FEM evolution across the entire height is quite close to the DIC values.

In order to emphasize the FEM accurate results, the entire x and y displacement fields are compared in Figure 6.23 and Figure 6.24, respectively.

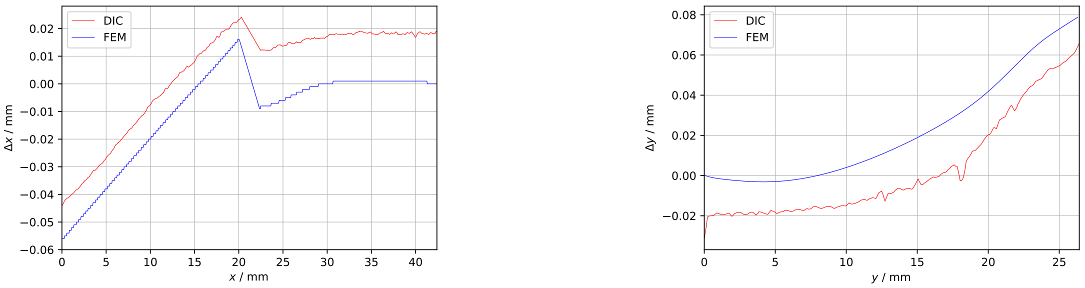

(a) HT1 displacements along x axis direction, for y=13.22 mm.

(b) HT1 displacements along y axis direction, for x=19.71 mm.

Figure 6.22: HT1 displacements plotted for the over a line analysis, both in x and y directions.

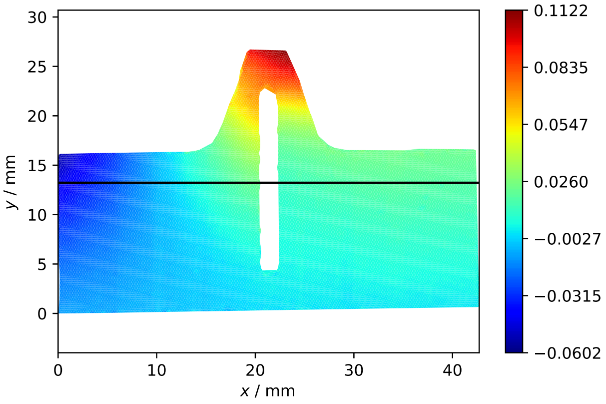

(a) DIC

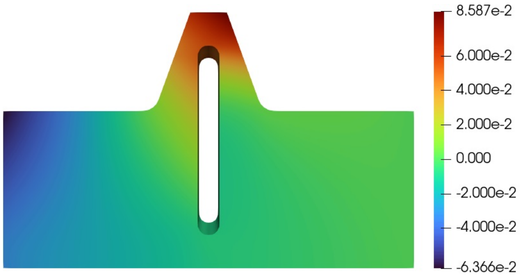

(b) FEM

Figure 6.23: HT1 displacements along x axis direction, for y=13.22 mm.

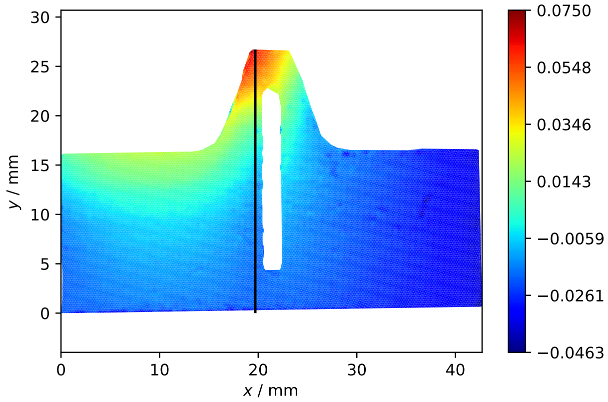

(a) DIC

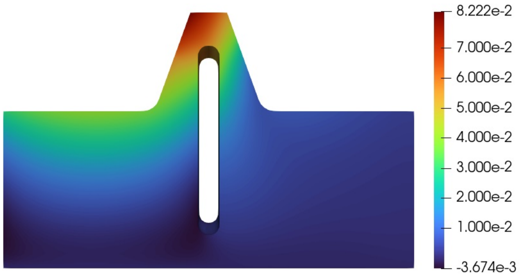

(b) FEM

Figure 6.24: HT1 displacements along y axis direction, for x=19.71 mm.

#### 6.3.4.3 HT2 Thermo-Mechanical Comparison

Finally, the HT2 x displacements are shown in Figure 6.25a, for y=13.22 mm. The FEM model results in a good approximation to the DIC results, but it is necessary to consider the offset between the representations, just as happened for the STD and HT1 tooth racks.

Regarding the y displacement plotted over a line for x=19.71 mm, Figure 6.25b, the FEM model progression is close to the DIC results, except when reaching the tooth tip height, where the FEM displacements increase slower than the DIC values and there is a most notorious progression difference.

The complete displacements field for x and y direction are in accordance with previous comments, with the FEM x displacement field, Figure 6.26 being closer to the DIC behavior, than the y displacement field, Figure 6.27. Nevertheless, the FEM thermo-mechanical model is considered accurate.

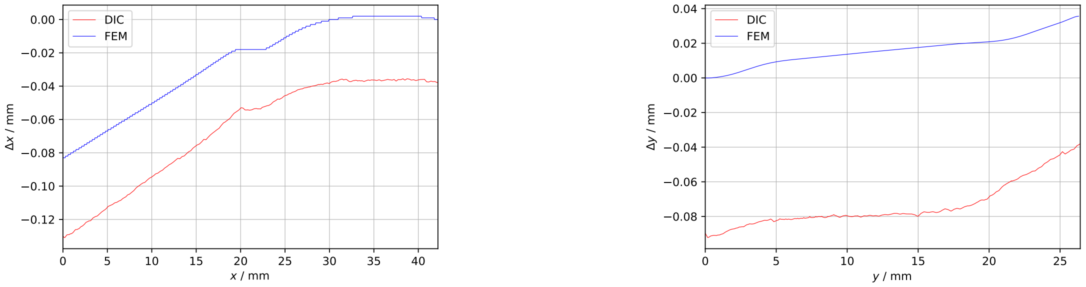

(a) HT2 displacements along x axis direction, for y=13.22 mm.

(b) HT2 displacements along y axis direction, for x=19.71 mm.

Figure 6.25: HT2 displacements plotted for the over a line analysis, both in x and y directions.

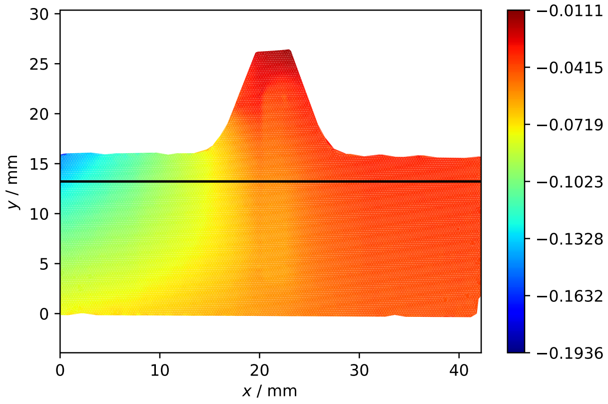

(a) DIC

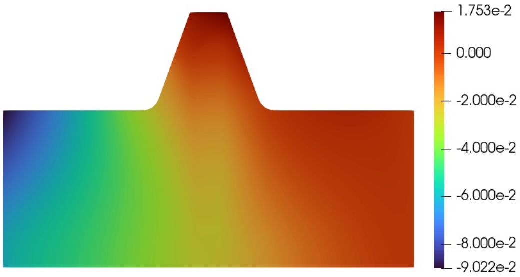

(b) FEM

Figure 6.26: HT2 displacements along x axis direction, for y=13.22 mm.

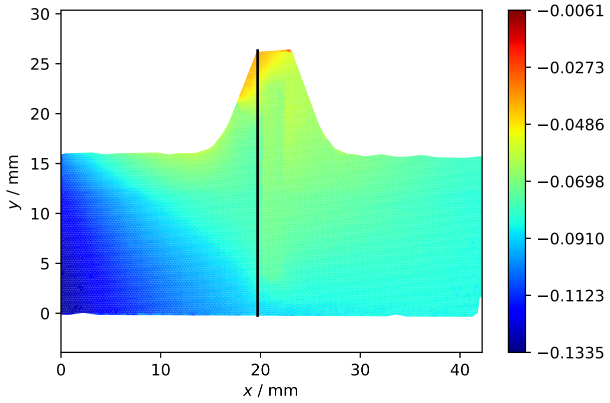

(a) DIC

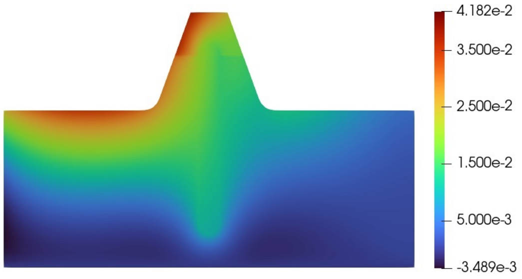

(b) FEM

Figure 6.27: HT2 displacements along y axis direction, for x=19.71 mm.

### 6.3.5 DIC Results with Offset Correction

In this section, the DIC results will be adjusted due to the offset observed when comparing the FEM thermo-mechanical model with the DIC curves. What happens is that, theoretically, the mechanical boundary conditions should restrict the displacements in some of the surfaces, namely the bottom (y=0 mm) and the supported side (x=42.41 mm) surfaces of the tooth rack, as mentioned in section 4.4.3. For the FEM model, these conditions are respected, however in the DIC experiment a certain offset is generated, which makes the displacement values different from 0 mm in those surfaces. This difference can be explained by a not perfectly smooth surface on the supported side, which would enable displacements in the x direction, for the analysed case. Also, the geometrical tolerances for the dovetail connection influenced the bottom surface restriction and displacements were observed in that region for the y direction analysis.

To summarize, for the over a line analysis in the x direction, the DIC results were adjusted in order to obtain a $\Delta x$=0 mm in x=42.41 mm. Regarding the over a line analysis in the y direction, for y=0 mm resulted $\Delta y$=0 mm. These corrections were performed using python scripts, and the results for STD, HT1 and HT2 are shown in Figures 6.28, 6.29 and 6.30, respectively.

It now makes sense to present the results of Tables 6.5, 6.6 and 6.7, which show the maximum displacements in x and y directions for the DIC results with the offset correction and for the FEM results, comparing them. For the all the specimens, it is proved again that the FEM model predicted accurately the displacement field. Although, it was obtained a relative error of 21.591 % in the x direction for STD, and a value of 30.769 % for the HT2 in the y direction.

Table 6.5: STD maximum displacements in x and y direction, for the over a line analysis after the offset correction.

| | STD | FEM | $\varepsilon_r/\%$ |
|---|---|---|---|
| $\Delta x_{max}$ | -0.088 | -0.069 | 21.591 |
| $\Delta y_{max}$ | 0.073 | 0.069 | 5.479 |

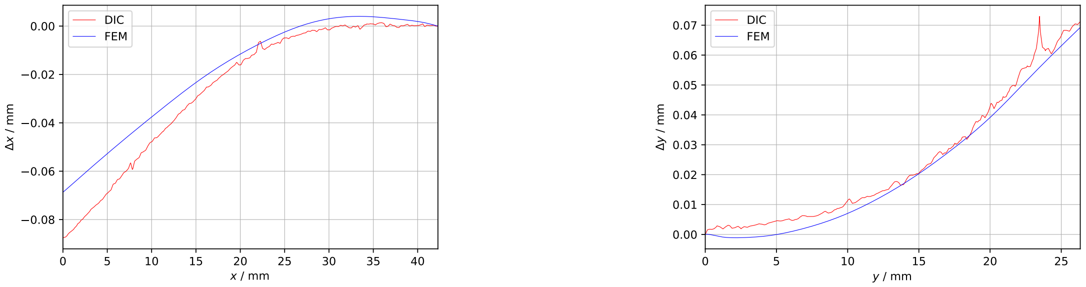

(a) STD displacements along x axis direction, for y=13.22 mm, with the applied offset correction.

(b) STD displacements along y axis direction, for x=21.21 mm, with the applied offset correction.

Figure 6.28: STD DIC displacements results with the respective offset corrections applied.

Table 6.6: HT1 maximum displacements in x and y direction, for the over a line analysis after the offset correction.

| | HT1 | FEM | $\varepsilon_r/\%$ |
|---|---|---|---|
| $\Delta x_{max}$ | -0.063 | -0.056 | 11.111 |
| $\Delta y_{max}$ | 0.086 | 0.079 | 8.139 |

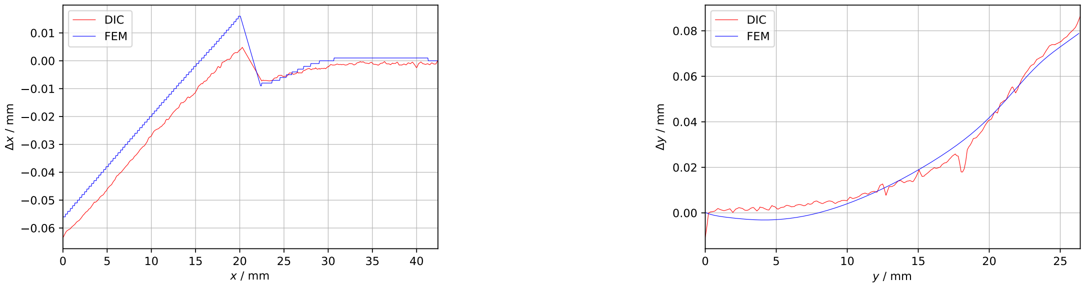

(a) HT1 displacements along x axis direction, for y=13.22 mm, with the applied offset correction.

(b) HT1 displacements along y axis direction, for x=19.71 mm, with the applied offset correction.

Figure 6.29: HT1 DIC displacements results with the respective offset corrections applied.

Table 6.7: HT2 maximum displacements in x and y direction, for the over a line analysis after the offset correction.

| | HT2 | FEM | $\varepsilon_r/\%$ |
|---|---|---|---|
| $\Delta x_{max}$ | -0.093 | -0.083 | -10.753 |
| $\Delta y_{max}$ | 0.052 | 0.036 | 30.769 |

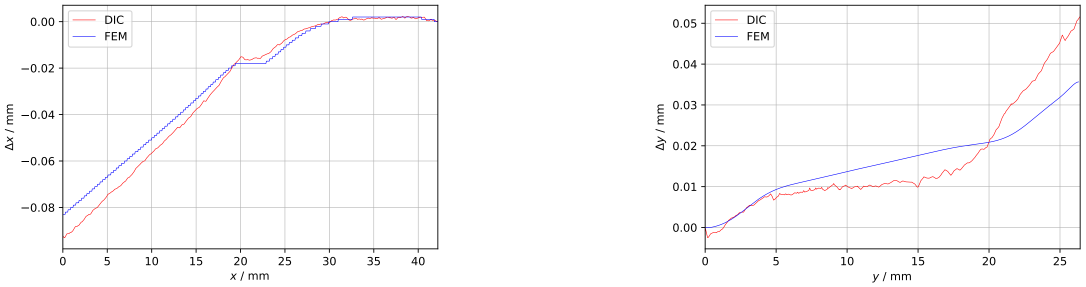

(a) HT2 displacements along x axis direction, for y=13.22 mm, with the applied offset correction.

(b) HT2 displacements along y axis direction, for x=19.71 mm, with the applied offset correction.

Figure 6.30: HT2 DIC displacements results with the respective offset corrections applied.

Concerning the new DIC results with the offset correction, comparing the HT2 results with the STD ones in the x axis direction, the maximum x displacement was higher for HT2, -0.093 mm, than for STD, -0.088 mm, in absolute value. This can be explained by the higher temperatures reached in the rack body for the HT2 specimen than the STD, as it was proven before by the thermal results. Thus, the thermal expansion effect promotes higher displacements for the tooth with the aluminium insert. However, for the y displacements the reverse happens. The highest displacements registered in this direction occur for the tooth tip, and since the HT2 specimen reaches lower temperatures in this region, it also obtains lower displacements. HT2 had a maximum displacement of 0.052 mm, while STD got 0.073 mm.

The maximum displacements obtained over a line, after the offset correction, can be found in Table 6.8, where the hybrid specimens (HT1 and HT2) are compared with the STD specimen for an overview of the final results.

Table 6.8: Comparison with STD of the maximum displacements in x and y directions, after the offset correction was applied.

| | STD | HT1 | $\%_{HT1}$ | HT2 | $\%_{HT2}$ |
|---|---|---|---|---|---|
| $\Delta x_{max}$ | -0.088 | -0.063 | -28.409 | -0.093 | 5.682 |
| $\Delta y_{max}$ | 0.073 | 0.086 | 17.808 | 0.052 | -28.767 |

## 6.4 Tooth Root Bending Stress Comparison

The FEM mechanical model will be now considered and compared with the tooth root bending stress calculated analytically in section 4.4.2. The calculations were performed for the STD specimen and the analytical result obtained was, $\sigma_f$=2.391 MPa.

The FEM model result for a section with a width corresponding to half of the tooth rack face width, so for z=7 mm, was $\sigma_{f,FEM}$=2.584 MPa.

The relative error of the analytical approximation is 7.487 %. At the end, it is possible to consider that the analytical solution can be used to predict the tooth root bending stress. However, the relative error obtained could be improved if more factors presented in the ISO 6336-6 [19] were considered and applied.

# Chapter 7

# Conclusions and Future Work

## 7.1 Conclusion

Throughout this dissertation, the main goal was to experimentally study the improvements of an hybrid polymer gear with an aluminium insert against a standard polymer gear. For this purpose, a heating and loading system was designed with the focus on providing conditions as close as possible to what happens during gear meshing. The thermal and thermo-mechanical behaviours were analysed for the hybrid gears and a FEM model was developed and then validated by the experimental results.

Two different type of tests were performed and analysed separately, those being the thermal and DIC tests. For each of them, three different specimens were studied, the standard tooth rack, STD, the hybrid tooth rack with no insert, HT1, and the hybrid tooth rack with aluminium insert, HT2.

For the thermal tests, a surface temperature analysis was performed and also a point analysis. The maximum temperatures reached in the heater were around 105 °C, and in the point of contact were between 80 °C and 85 °C, approximately, depending on the tested specimen.

Considering a result discussion focused on the moment when the maximum heater temperatures were reached, starting with the tooth tip point, T3B, the HT2 obtained the lowest values. Comparing with the STD, the difference was around 10 °C, with the hybrid tooth with the aluminium insert immediately proving a better heating evacuation impact for this point. For the contact region point, T2B, and the tooth root point, T1B, the same effect was observed. Once again the HT2 registered the lowest temperatures, but for the T1B point, the difference between the HT2 and the STD was not high, with a variation of -8.24 %. A different behaviour was noticed for the insert and the bottom points, T2A and T1A, respectively. Here comparing the STD with the HT2, this time STD obtained the lowest values. The aluminium insert in HT2 has an higher thermal conductivity than POM, so its temperature increased while evacuating the heat and made the temperature values in the rack body slightly higher than the ones registered for STD.

Then, the FEM thermal model is considered accurate, with the results following the tendency of the temperature distribution of the experimental results, for all specimens. Regarding the points in study, for STD the maximum relative error was 9.80 % for the contact point, T2B. The HT1 specimen obtained 15.62 % for the insert point, T2A, and HT2 17.90 % for the contact point, T2B.

As a conclusion for the thermal results, it was verified an improvement of the thermal conditions using a hybrid polymer gear and so the concept was validated.

For the DIC experiments, the testing conditions were similar to the thermal tests ones, but this time it was applied a speckle pattern to the specimens surface to help following the displacement variation. The goal was to study the displacement on the tooth rack surface caused by the thermal and mechanical conditions, for a heater temperature of 105 °C.

For HT2, the maximum displacement in x direction was higher than the one for the STD. The x displacement field of HT2 presented higher values close to the not supported side of the rack, as the aluminium insert also promotes the thermal expansion in this region, but restricts it close to the insert region. Regarding the y direction, HT2 obtained a maximum displacement, again higher than the one verified in STD. For the y displacement field of HT2, the highest displacement values are located at the same region of the x displacement maximum ones, and for the same reasons.

Concerning the FEM thermo-mechanical model, for all the specimens it was shown a similar progression comparing to the experiment results, but always with a certain offset. The y displacements presented higher offsets. In the case of HT2, the x displacements presented an higher offset than the ones verified for the STD and HT1 specimens in the x axis direction. The offsets are much related to the surface finish and geometrical tolerances not totally respected when manufacturing the specimens. It caused the surfaces to not get perfectly fixed in the dovetail connection and not uniformly supported on the supported side of the tooth rack, promoting some extra displacements in the boundary conditions with two movement restricted axis. Also, the thermal resistance at the insert's contact with the rack body is difficult to define precisely. However, applying an offset correction to the DIC results, the maximum displacements registered over a line for x and y direction are closer to the ones obtained by the FEM model.

At the end, HT2 maximum displacement in x direction was 5.682 % higher than the STD one, after the offset correction. In the y direction, HT2 obtained -28.767 % than STD specimen.

Finally, it was concluded that the hybrid polymer gear concept was validated as the heating evacuation successfully decreased the temperature in the tooth contact region and the displacements registered are not far from the ones of the standard tooth and do not disturb the proper gear operation.

## 7.2 Future Works

- Analyse the stresses in the insert region;
- Redesign the heating and loading system to avoid such high direct heat transfer from the load and heat application tool to the tooth rack body;
- Apply the 3D DIC technique to obtain even more accurate displacement results and to study the strain and stresses on the hybrid polymer gear;

- Perform a new experimental test where there is gear meshing between hybrid gears. Study their thermal and thermo-mechanical behaviour;
- Perform a study on the dynamics of hybrid gears;

# References

[1] Mário R. C. Moutinho. Load carrying capacity of polymer-metal hybrid gears. Master's thesis, Faculdade de Engenharia da Universidade do Porto, 2020.

[2] James D. S. Hooton. Preliminary validation of a hybrid polymer gear concept. Master's thesis, Faculdade de Engenharia da Universidade do Porto, 2021.

[3] Carlos M.C.G. Fernandes, Diogo M.P. Rocha, Ramiro C. Martins, Luis Magalhães, and Jorge H.O. Seabra. Finite element method model to predict bulk and flash temperatures on polymer gears. *Tribology International*, 120(December 2017):255–268, 2018. ISSN 0301679X.

[4] Carlos M.C.G. Fernandes, Diogo M.P. Rocha, Ramiro C. Martins, Luis Magalhaes, and Jorge H.O. Seabra. Hybrid Polymer Gear Concepts to Improve Thermal Behavior. *Journal of Tribology*, 141(3):1–12, 2019. ISSN 15288897.

[5] Khalid Abdulkhaliq M. Alharbi. *The Mechanical Contact Behaviour and Tribology of Polymer Gears by*. PhD thesis, The University of Warwick, 2018.

[6] Nikolai K. Myshkin and Alekcander V. Kovalev. Friction and Wear of Polymers and Polymer Composites. In *Friction, Lubrication, and Wear Technology*. ASM International, 2017.

[7] M. Hribersek, M. Erjavec, Gorazd Hlebanja, and Simon Kulovec. Durability testing and characterization of POM gears. *Engineering Failure Analysis*, 124(December 2020):105377, 2021. ISSN 13506307.

[8] Verein Deutscher Ingenieure. VDI 2736 - Part 1. 2736, 2013. Thermoplastic gear wheels-Materials, material selection, production methods, production tolerances, form design.

[9] Alencar Bravo, Demagna Koffi, Lotfi Toubal, and Fouad Erchiqui. Life and damage mode modeling applied to plastic gears. *Engineering Failure Analysis*, 58(P1):113–133, 2015. ISSN 13506307.

[10] Hiroki Arikado. Argument on Plastic Gears for Power Transmission. *JSME International Journal*, 38(43):2091, 2002.

[11] K. Mao, W. Li, C. J. Hooke, and D. Walton. Friction and wear behaviour of acetal and nylon gears. *Wear*, 267(1-4):639–645, 2009. ISSN 00431648.

[12] Hüseyin Imrek. Performance improvement method for Nylon 6 spur gears. *Tribology International*, 42(3):503–510, 2009. ISSN 0301679X.

[13] Prashant Kumar Singh, Siddhartha, and Akant Kumar Singh. An investigation on the effects of the various techniques over the performance and durability of polymer gears. *Materials Today: Proceedings*, 4(2):1606–1614, 2017. ISSN 22147853.

[14] BR Höhn, P Oster, K Michaelis, T Suchandt, and K Stahl. Bending fatigue investigation under variable load conditions on case-carburized gears. In *AGMA Fall Technical Meeting, Cincinnati, OH*, 2000.

[15] JF Remacle, J Lambrechts, and B Seny. Blossom-Quad: A non-uniform quadrilateral mesh generator using a minimum-cost perfect-matching algorithm. *International*, (February): 1102–1119, 2012.

[16] Theodore L Bergman, Adrienne S Lavine, and Eduardo Mach Queiroz. *Fundamentos de Transferência de Calor E de Massa* . Grupo Gen-LTC, 2000.

[17] Vincenzo Vullo. *Gears Volume 2: Analysis of Load Carrying Capacity and Strength Design*, volume 2. Rome, Springer, 2020. ISBN 9783030365011.

[18] Stephen P. Timoshenko. *Strength of materials Part 1*. New York, Van Nostrand Company, Inc., 1955.

[19] ISO 6336-3. Calculation of load capacity of spur and helical gears: Calculation of surface durability (pitting). *International Organization for Standardization*, 3:33, 2006. ISSN 0743-6858.

[20] Bing Pan and Kai Li. A fast digital image correlation method for deformation measurement. *Optics and Lasers in Engineering*, 49(7):841–847, 2011. ISSN 01438166.

[21] D. Lecompte, A. Smits, Sven Bossuyt, H. Sol, J. Vantomme, D. Van Hemelrijck, and A. M. Habraken. Quality assessment of speckle patterns for digital image correlation. *Optics and Lasers in Engineering*, 44(11):1132–1145, 2006. ISSN 01438166.

## Appendix A

# Gear Tooth Heating System Technical Drawings

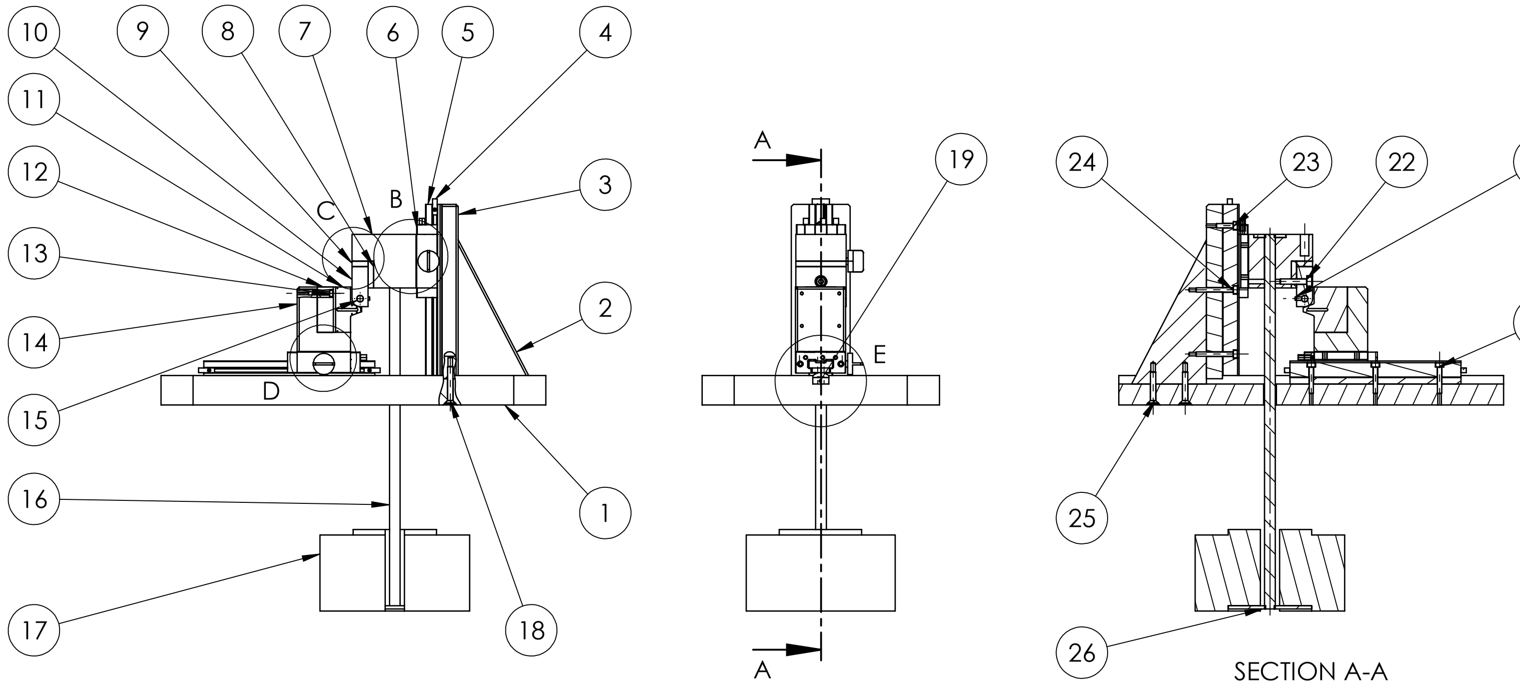

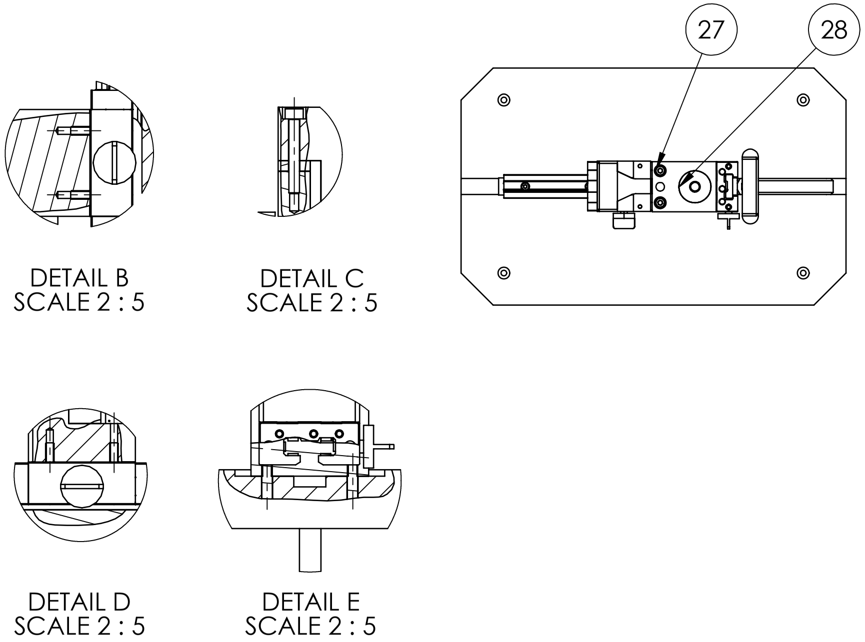

| Scale<br>1:5 | Geometrical Product Specifications ISO 8015<br>General Geometrical Tolerances ISO 2768-fH<br>ISO 13920<br>Surface Texture ISO 1302<br>Edges and Chamfers ISO 13715 | | |
|---|---|---|---|
| | Date | Name | |
| Drawn | 07/04/2022 | João M.A. Pinto | |
| Checked | 07/04/2022 | Carlos M.C.G. Fernandes | Paper Size<br>A3 |
| Standard | | | |
| Responsible Dept.<br>DEMec | Technical Reference | Document Type<br>Assembly Drawing | |
| Legal Owner | DEMec<br>CETRIB<br>João M.A. Pinto | Title<br>Gear Tooth Heating System | Sheet 1/1 |

## PARTS LIST

| ITEM NO. | QTY. | DESCRIPTION | PART NUMBER | MATERIAL |
|---|---|---|---|---|
| 1 | 1 | Table Support Plate | | Aluminium 6061 |
| 2 | 1 | Vertical Rib | | Aluminium 6061 |
| 3 | 1 | Support Column | | Aluminium 6061 |
| 4 | 3 | Travel Stop Device | | Aluminium 6061 |
| 5 | 2 | Drylin® T Guide Rail TS | | aluminum, hard anodized |
| 6 | 2 | Drylin® T Guide Carriage TW-01-HKA | | Aluminum housing, plastic cover, iglidur® J gliders |
| 7 | 1 | Load and Heat Application Block | | Aluminium 6061 |
| 8 | 1 | Polymer Vertical Plate | | POM Acetal Copolymer |
| 9 | 1 | Horizontal Polymer Plate | | POM Acetal Copolymer |
| 10 | 1 | Load and Heat Application Tool | | Aluminium 6061 |
| 11 | 1 | Hybrid Polymer Gear Tooth | | POM Acetal Copolymer |
| 12 | 2 | Hybrid Polymer Gear Tooth Support | | Aluminium 6061 |
| 13 | 4 | Hexagon Socket Head Cap Screw | ISO 4762 M3 x 20 - 20N | |
| 14 | 1 | Hybrid Polymer Gear Tooth Base | | Aluminium 6061 |
| 15 | 1 | Hotend Heater Cartridge (24V, 50W) | | |
| 16 | 1 | Shaft | | AISI 316 Stainless Steel Sheet (SS) |
| 17 | 1 | Weight | | 1.6582 (34CrNiMo6) |
| 18 | 2 | Hex Socket CTSK Head | ISO 10642 - M5 x 35 - 35N | |
| 19 | 1 | Horizontal Linear Guide Support | | Aluminium 6061 |
| 20 | 11 | Hexagon Socket Head Cap Screw | ISO 4762 M4 x 25 - 25N | |
| 21 | 1 | Hexagon Socket Head Cap Screw | ISO 4762 M5 x 25 - 25N | |
| 22 | 1 | Hexagon Socket Head Cap Screw | ISO 4762 M4 x 16 - 16N | |
| 23 | 2 | Hexagon Socket Head Cap Screw | ISO 4762 M4 x 35 - 35N | |
| 24 | 2 | Hex Socket CTSK Head | ISO 10642 - M5 x 30 - 30N | |
| 25 | 1 | Weight Support Plate | | AISI 316 Stainless Steel Sheet (SS) |
| 26 | 2 | Hexagon Socket Head Cap Screw | ISO 4762 M5 x 35 - 35N | |
| 27 | 1 | Support Circular Plate | | AISI 316 Stainless Steel Sheet (SS) |
| 28 | 7 | | ISO 4026 - M3 x 6-N | |

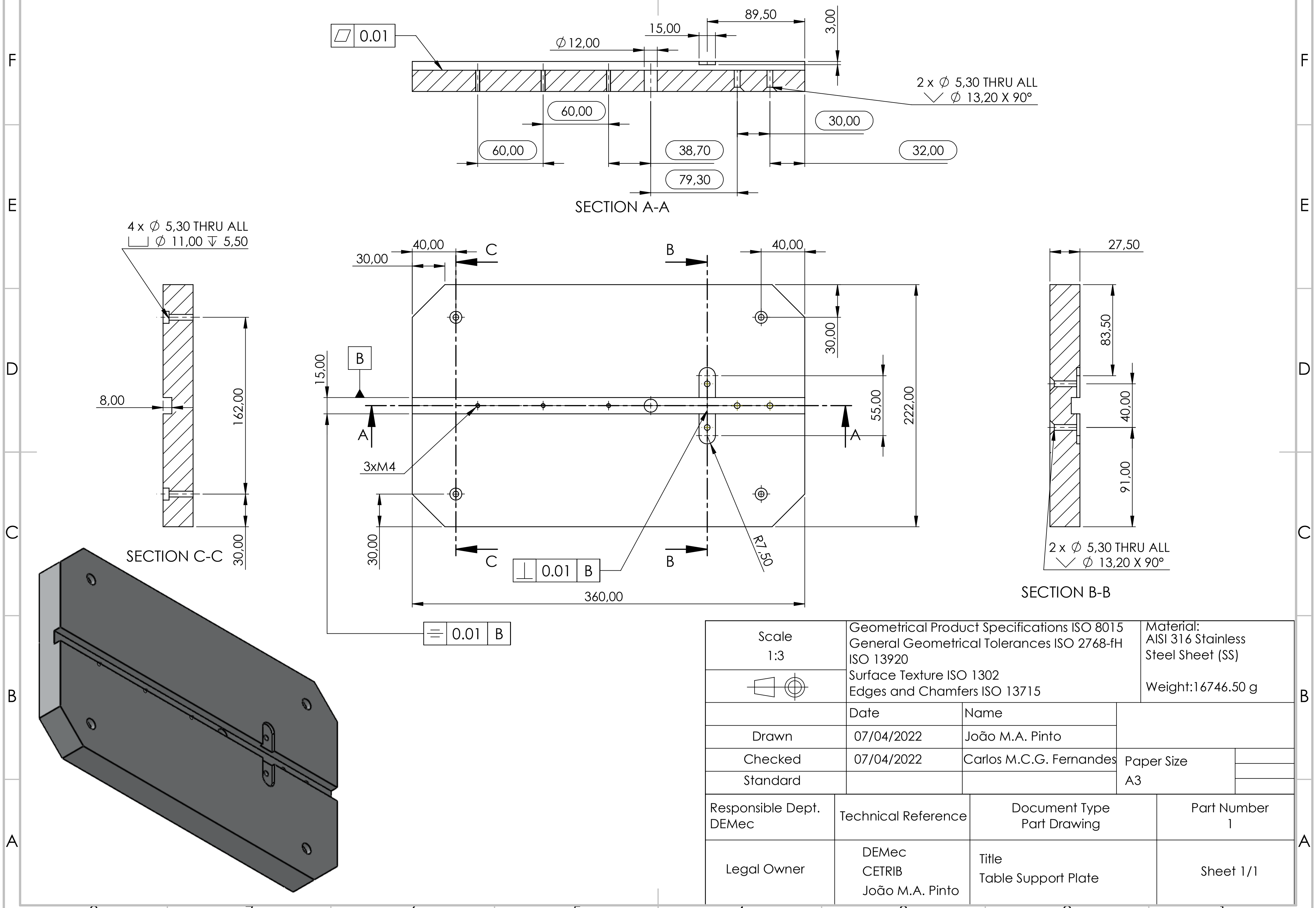

| | | | |
|---|---|---|---|
| Scale<br>1:3 | Geometrical Product Specifications ISO 8015<br>General Geometrical Tolerances ISO 2768-fH<br>ISO 13920<br>Surface Texture ISO 1302<br>Edges and Chamfers ISO 13715 | | Material:<br>AISI 316 Stainless<br>Steel Sheet (SS)<br>Weight:16746.50 g |
| | Date | Name | |
| Drawn | 07/04/2022 | João M.A. Pinto | |
| Checked | 07/04/2022 | Carlos M.C.G. Fernandes | Paper Size<br>A3 |
| Standard | | | |

| | | | |
|---|---|---|---|
| Responsible Dept.<br>DEMec | Technical Reference | Document Type<br>Part Drawing | Part Number<br>1 |
| Legal Owner | DEMec<br>CETRIB<br>João M.A. Pinto | Title<br>Table Support Plate | Sheet 1/1 |

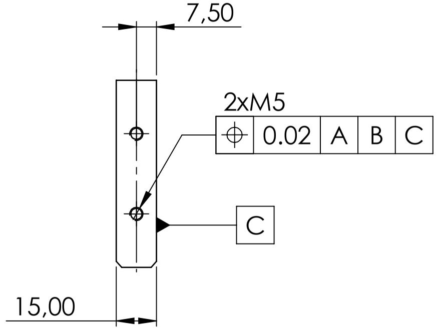

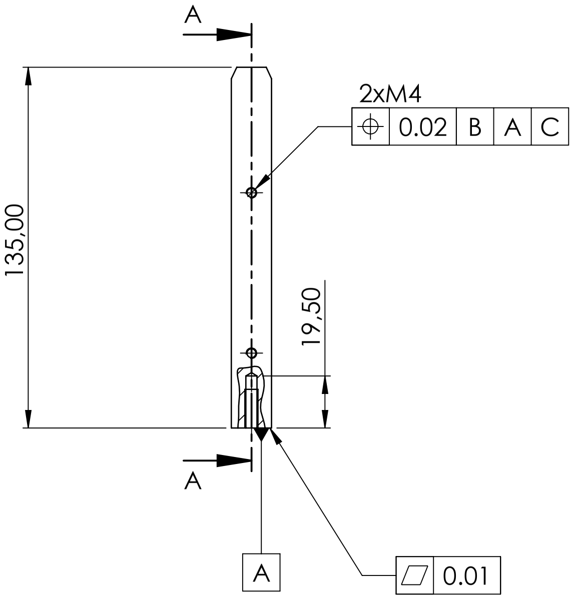

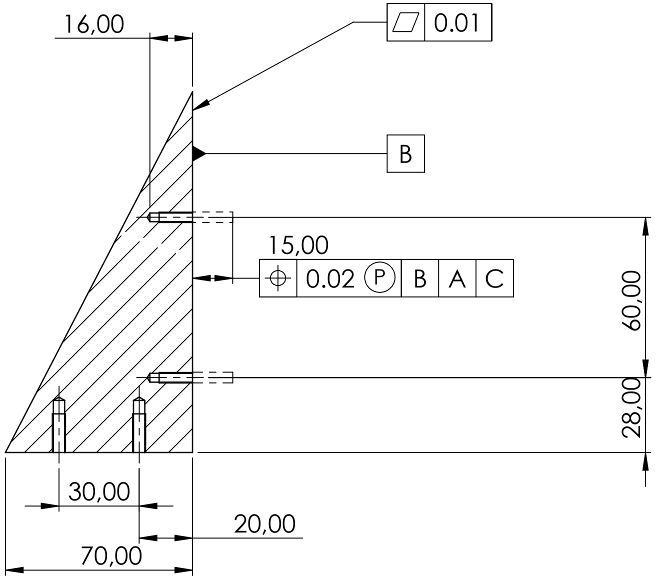

SECTION A-A

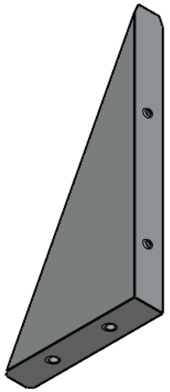

| | | | |
|---|---|---|---|
| Scale<br>1:2 | Geometrical Product Specifications ISO 8015<br>General Geometrical Tolerances ISO 2768-fH<br>ISO 13920<br>Surface Texture ISO 1302<br>Edges and Chamfers ISO 13715 | | Material:<br>6061 Alloy<br>Weight:187.49 g |
| | Date | Name | |
| Drawn | 07/04/2022 | João M.A. Pinto | |
| Checked | 07/04/2022 | Carlos M.C.G. Fernandes | Paper Size<br>A3 |
| Standard | | | |
| Responsible Dept.<br>DEMec | Technical Reference | Document Type<br>Part Drawing | Part Number<br>2 |
| Legal Owner | DEMec<br>CETRIB<br>João M.A. Pinto | Title<br>Vertical Rib | Sheet 1/1 |

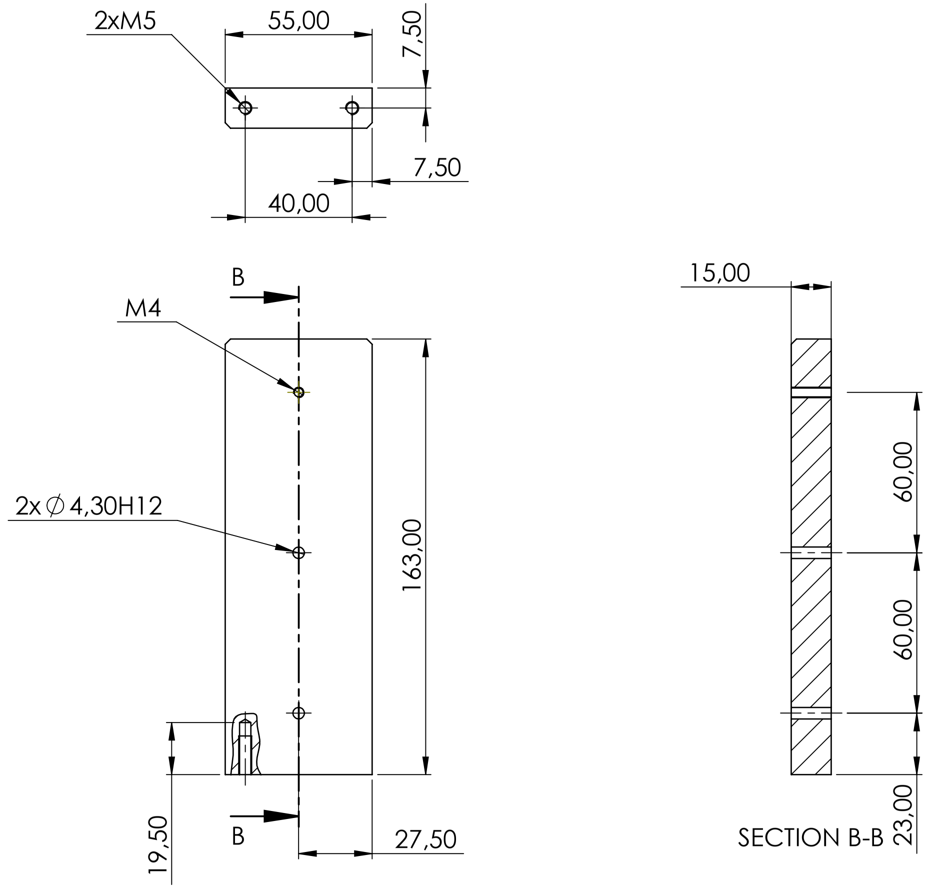

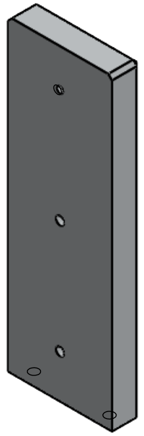

|  |  |  |  |
|---|---|---|---|
| Scale<br>1:2 | Geometrical Product Specifications ISO 8015<br>General Geometrical Tolerances ISO 2768-fH<br>ISO 13920<br>Surface Texture ISO 1302<br>Edges and Chamfers ISO 13715 |  | Material:<br>6061 Alloy<br>Weight:357.88 g |
|  | Date | Name |  |
| Drawn | 07/04/2022 | João M.A. Pinto |  |
| Checked | 07/04/2022 | Carlos M.C.G. Fernandes | Paper Size<br>A3 |
| Standard |  |  |  |
| Responsible Dept.<br>DEMec | Technical Reference | Document Type<br>Part Drawing | Part Number<br>3 |
| Legal Owner | DEMec<br>CETRIB<br>João M.A. Pinto | Title<br>Support Column | Sheet 1/1 |

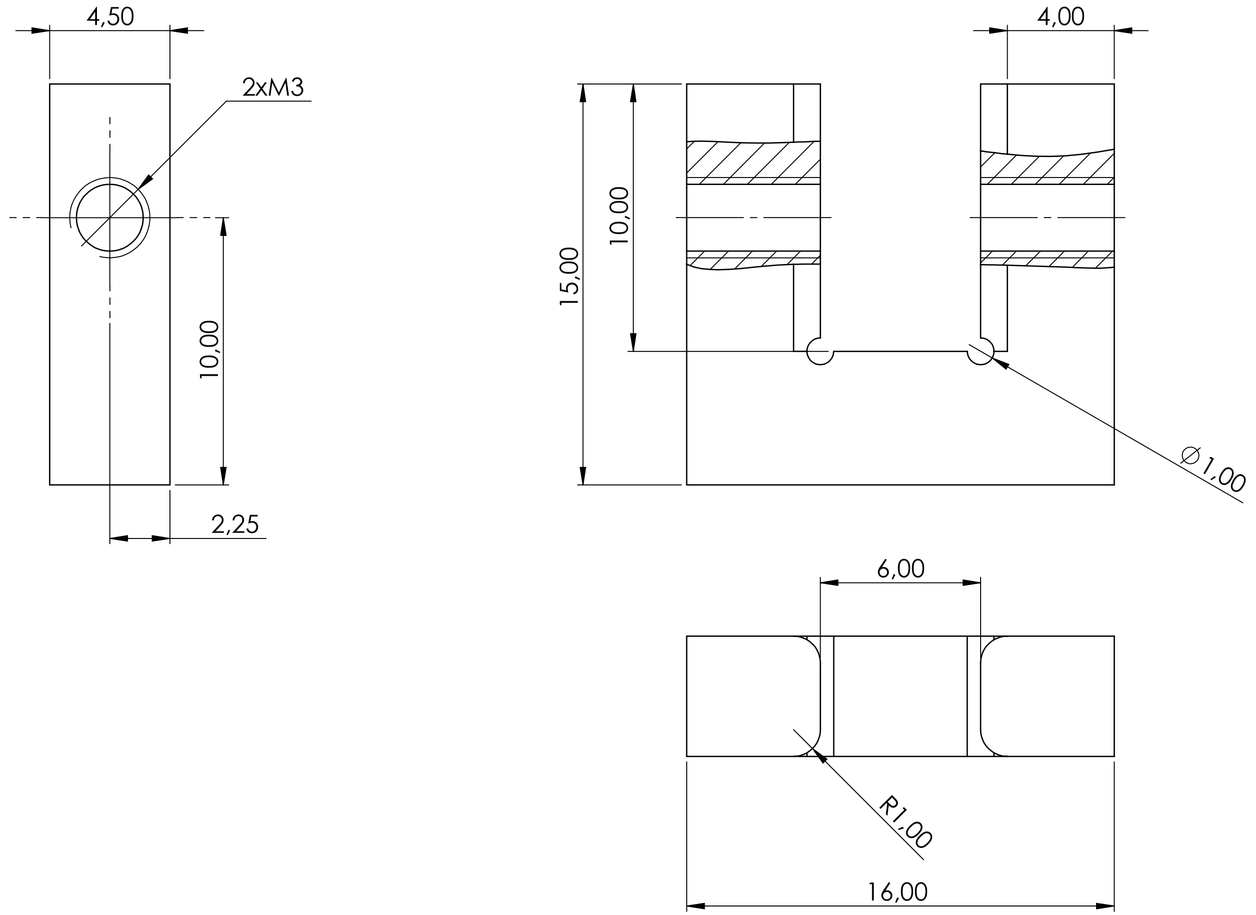

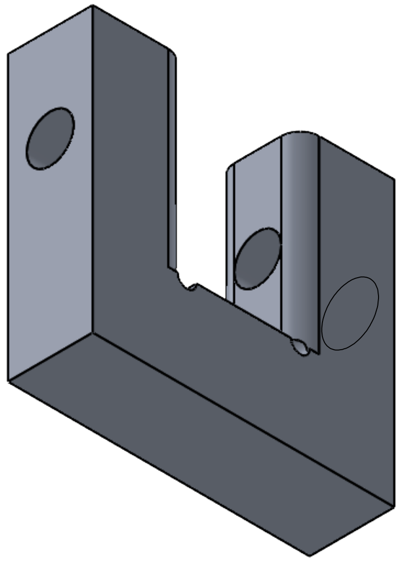

| | | | | |
|---|---|---|---|---|
| Scale<br>5:1 | Geometrical Product Specifications ISO 8015<br>General Geometrical Tolerances ISO 2768-fH<br>ISO 13920<br>Surface Texture ISO 1302<br>Edges and Chamfers ISO 13715 | | Material:<br>6061 Alloy<br>Weight:2.02 g | |
| | Date | Name | | |
| Drawn | 07/04/2022 | João M.A. Pinto | | |
| Checked | 07/04/2022 | Carlos M.C.G. Fernandes | Paper Size<br>A3 | |
| Standard | | | | |
| Responsible Dept.<br>DEMec | Technical Reference | Document Type<br>Part Drawing | Part Number<br>4 | |
| Legal Owner | DEMec<br>CETRIB<br>João M.A. Pinto | Title<br>Travel Stop Device | Sheet 1/1 | |

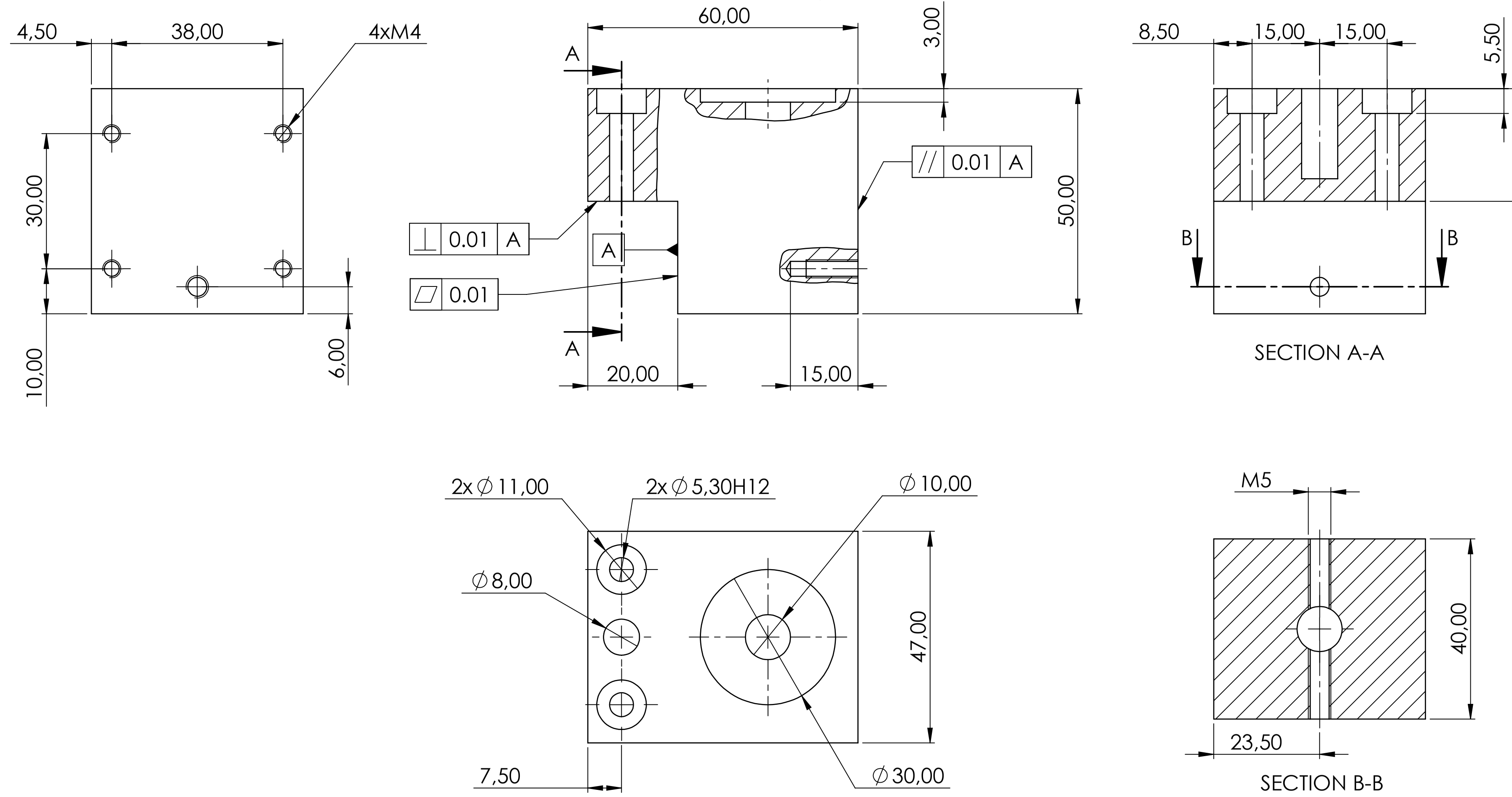

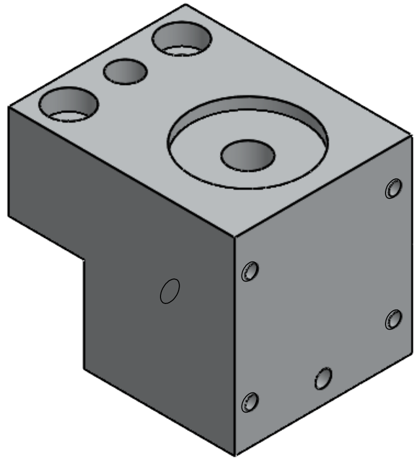

| | | | |
|---|---|---|---|
| Scale<br>1:1 | Geometrical Product Specifications ISO 8015<br>General Geometrical Tolerances ISO 2768-fH<br>ISO 13920<br>Surface Texture ISO 1302<br>Edges and Chamfers ISO 13715 | | Material:<br>6061 Alloy<br>Weight:291.15 g |
| | Date | Name | |
| Drawn | 07/04/2022 | João M.A. Pinto | |
| Checked | 07/04/2022 | Carlos M.C.G. Fernandes | Paper Size<br>A3 |
| Standard | | | |
| Responsible Dept.<br>DEMec | Technical Reference | Document Type<br>Part Drawing | Part Number<br>7 |
| Legal Owner | DEMec<br>CETRIB<br>João M.A. Pinto | Title<br>Load and Heat Application Block | Sheet 1/1 |

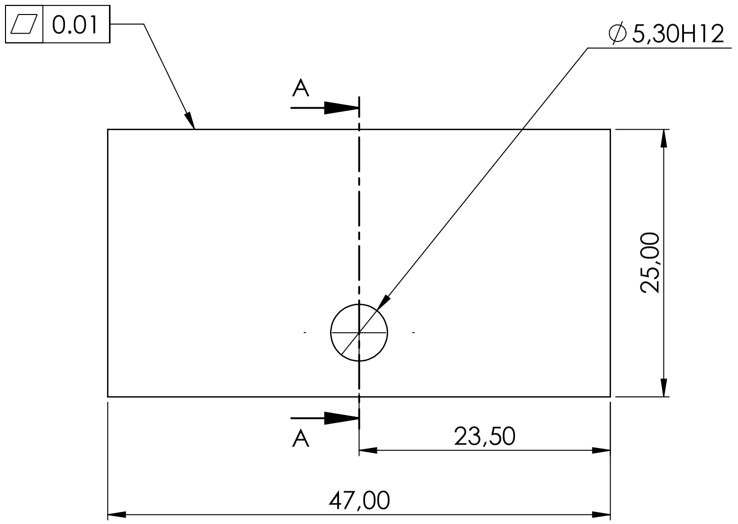

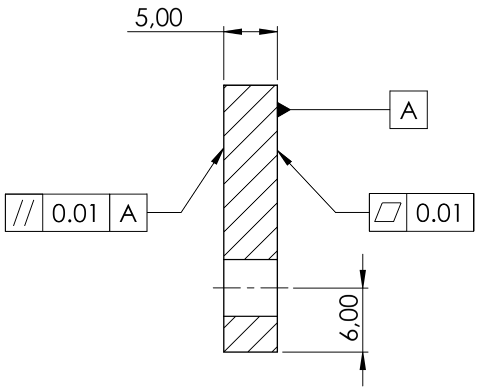

SECTION A-A

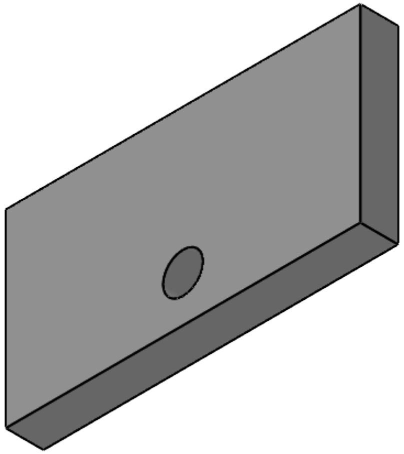

| | | | |
|---|---|---|---|
| Scale<br>2:1 | Geometrical Product Specifications ISO 8015<br>General Geometrical Tolerances ISO 2768-fH<br>ISO 13920<br>Surface Texture ISO 1302<br>Edges and Chamfers ISO 13715 | | Material:<br>POM Acetal<br>Copolymer<br><br>Weight:8.01 g |
| | Date | Name | |
| Drawn | 07/04/2022 | João M.A. Pinto | |
| Checked | 07/04/2022 | Carlos M.C.G. Fernandes | Paper Size<br>A3 |
| Standard | | | |

| | | | |
|---|---|---|---|
| Responsible Dept.<br>DEMec | Technical Reference | Document Type<br>Part Drawing | Part Number<br>8 |
| Legal Owner | DEMec<br>CETRIB<br>João M.A. Pinto | Title<br>Polymer Vertical Plate | Sheet 1/1 |

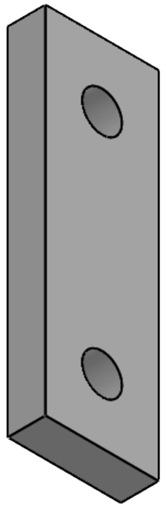

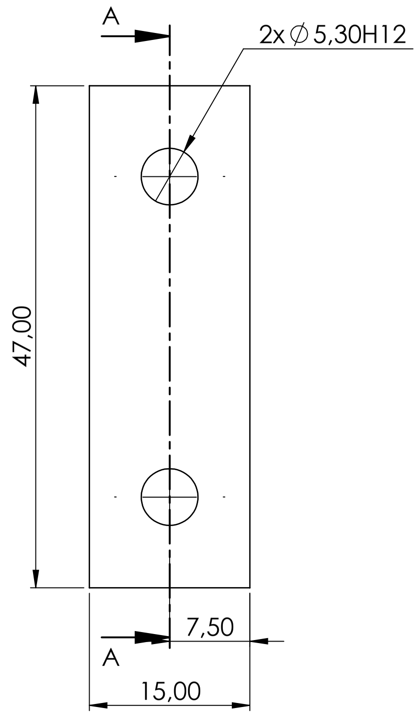

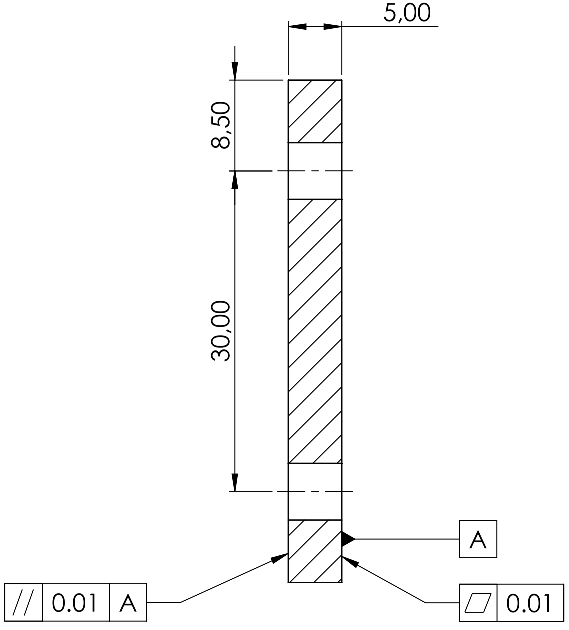

SECTION A-A

| | | | |
|---|---|---|---|
| Scale<br>2:1 | Geometrical Product Specifications ISO 8015<br>General Geometrical Tolerances ISO 2768-fH<br>ISO 13920<br>Surface Texture ISO 1302<br>Edges and Chamfers ISO 13715 | | Material:<br>POM Acetal<br>Copolymer<br>Weight:4.59 g |
| | Date | Name | |
| Drawn | 07/04/2022 | João M.A. Pinto | |
| Checked | 07/04/2022 | Carlos M.C.G. Fernandes | Paper Size<br>A3 |
| Standard | | | |

| | | | |
|---|---|---|---|
| Responsible Dept.<br>DEMec | Technical Reference | Document Type<br>Part Drawing | Part Number<br>9 |
| Legal Owner | DEMec<br>CETRIB<br>João M.A. Pinto | Title<br>Horizontal Polymer Plate | Sheet 1/1 |

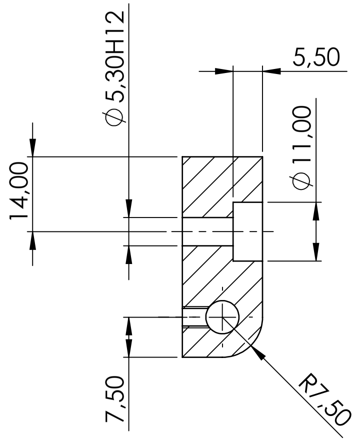

SECTION B-B

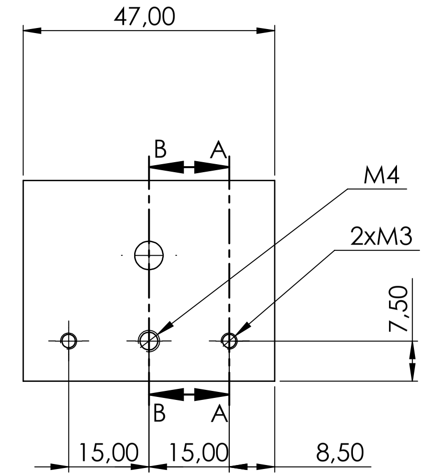

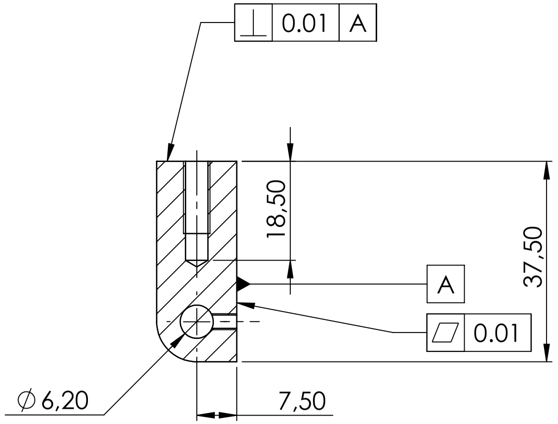

SECTION A-A

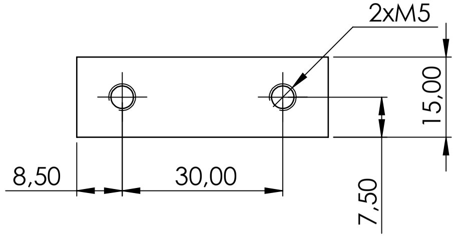

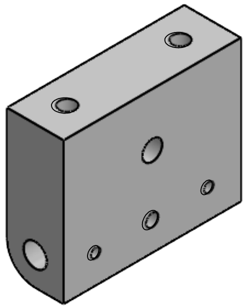

| | | | |
|---|---|---|---|
| Scale<br>2:1 | Geometrical Product Specifications ISO 8015<br>General Geometrical Tolerances ISO 2768-fH<br>ISO 13920<br>Surface Texture ISO 1302<br>Edges and Chamfers ISO 13715 | | Material:<br>6061 Alloy<br>Weight:62.40 g |
| | Date | Name | |
| Drawn | 07/04/2022 | João M.A. Pinto | |
| Checked | 07/04/2022 | Carlos M.C.G. Fernandes | Paper Size<br>A3 |
| Standard | | | |

| | | | |
|---|---|---|---|
| Responsible Dept.<br>DEMec | Technical Reference | Document Type<br>Part Drawing | Part Number<br>10 |
| Legal Owner | DEMec<br>CETRIB<br>João M.A. Pinto | Title<br>Load and Heat Application Tool | Sheet 1/1 |

| TAG | X LOC | Y LOC | SIZE |
|---|---|---|---|
| A1 | 1,20 | 1,73 | ∅0,60↧0,50 |
| A2 | 17,28 | 15,23 | ∅0,60↧0,50 |
| A3 | 18,92 | 19,73 | ∅0,60↧0,50 |
| A4 | 20,34 | 23,63 | ∅0,60↧0,50 |
| A5 | 22,07 | 23,63 | ∅0,60↧0,50 |
| A6 | 23,49 | 19,73 | ∅0,60↧0,50 |
| A7 | 25,13 | 15,23 | ∅0,60↧0,50 |
| A8 | 41,21 | 1,73 | ∅0,60↧0,50 |

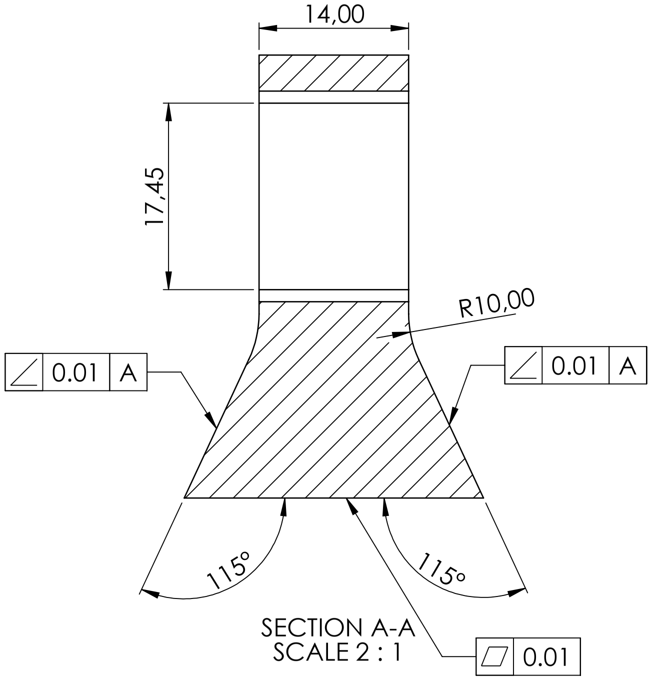

SECTION A-A
SCALE 2 : 1

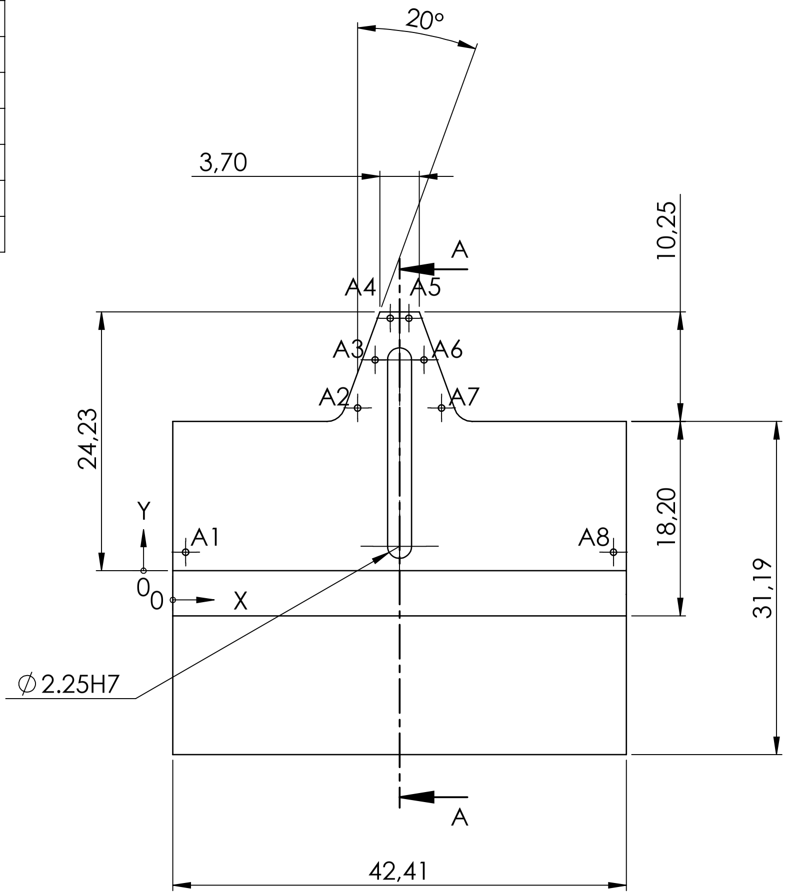

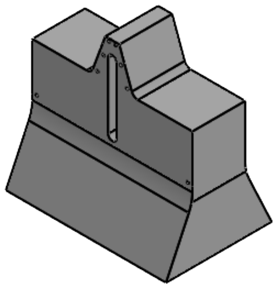

| Geometry | |
|---|---|
| Normal Module [mm], m | 4,5 |
| Normal Pressure angle, α | 2,0 |
| Root Radius Coefficient, rr | 0,38 |
| Fillet Radius [mm], rf=rr x m | 1,71 |

Scale
1:1

Geometrical Product Specifications ISO 8015
General Geometrical Tolerances ISO 2768-fH
ISO 13920
Surface Texture ISO 1302
Edges and Chamfers ISO 13715

Material:
POM Acetal
Copolymer

Weight:32.62 g

| | Date | Name |
|---|---|---|
| Drawn | 07/04/2022 | João M.A. Pinto |
| Checked | 07/04/2022 | Carlos M.C.G. Fernandes |
| Standard | | |

Paper Size
A3

Responsible Dept.
DEMec

Technical Reference

Document Type
Part Drawing

Part Number
11

Legal Owner

DEMec
CETRIB
João M.A. Pinto

Title
Hybrid Polymer Gear Tooth

Sheet 1/1

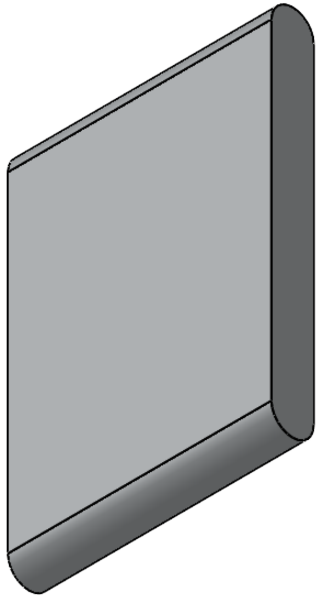

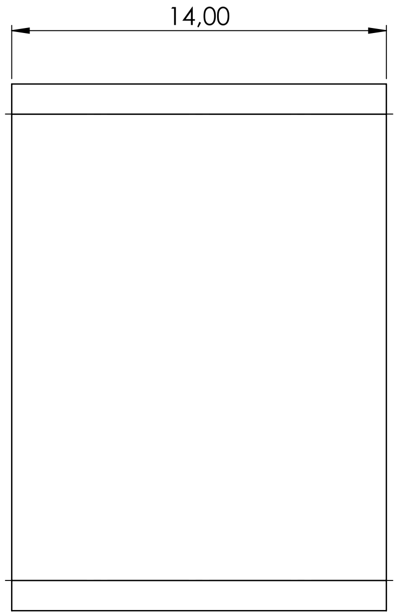

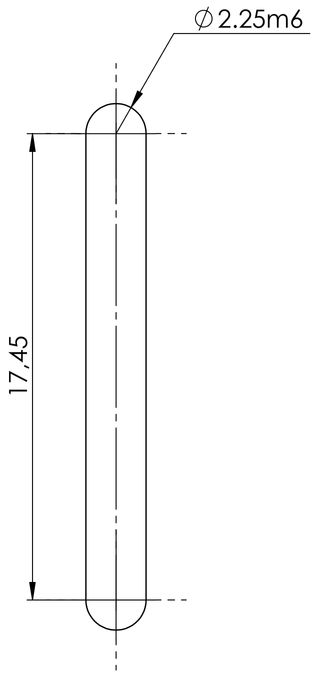

| | | | |
|---|---|---|---|
| Scale<br>5:1 | Geometrical Product Specifications ISO 8015<br>General Geometrical Tolerances ISO 2768-fH<br>ISO 13920<br>Surface Texture ISO 1302<br>Edges and Chamfers ISO 13715 | | Material:<br>6061 Alloy<br>Weight:1.63 g |
| | Date | Name | |
| Drawn | 07/04/2022 | João M.A. Pinto | |
| Checked | 07/04/2022 | Carlos M.C.G. Fernandes | Paper Size<br>A3 |
| Standard | | | |
| Responsible Dept.<br>DEMec | Technical Reference | Document Type<br>Part Drawing | Part Number |
| Legal Owner | DEMec<br>CETRIB<br>João M.A. Pinto | Title<br>Hybrid Tooth Insert | Sheet 1/1 |

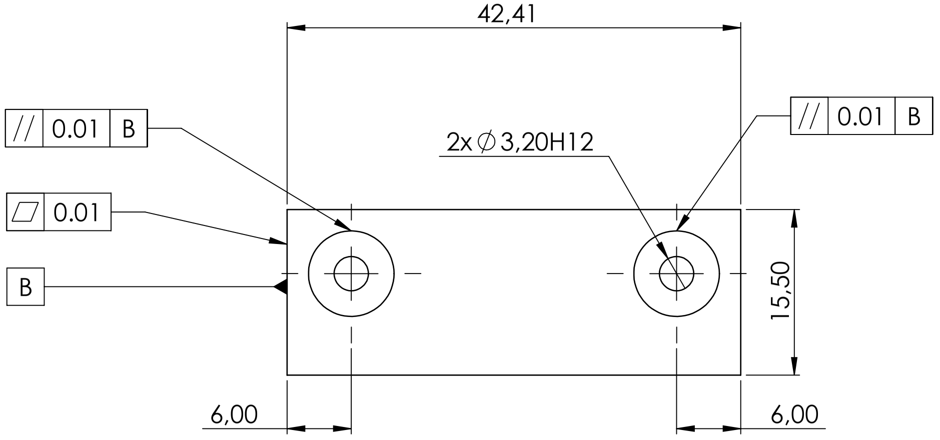

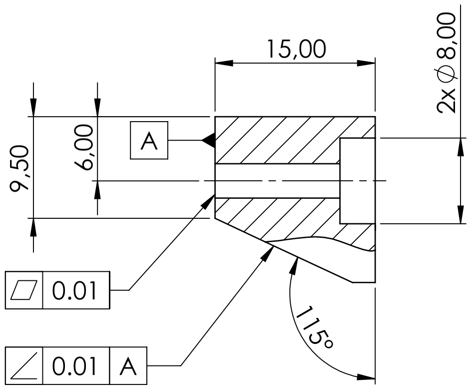

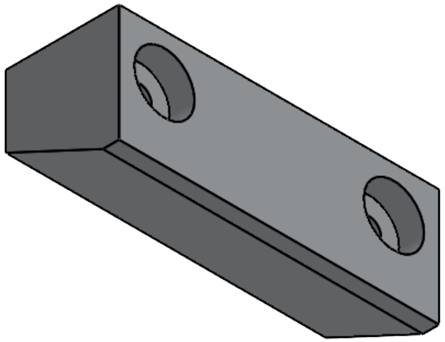

| | | | | |
|---|---|---|---|---|
| Scale<br>2:1 | Geometrical Product Specifications ISO 8015<br>General Geometrical Tolerances ISO 2768-fH<br>ISO 13920<br>Surface Texture ISO 1302<br>Edges and Chamfers ISO 13715 | | Material:<br>6061 Alloy<br>Weight:20.80 g | |
| | Date | Name | | |
| Drawn | 07/04/2022 | João M.A. Pinto | | |
| Checked | 07/04/2022 | Carlos M.C.G. Fernandes | Paper Size<br>A3 | |
| Standard | | | | |
| Responsible Dept.<br>DEMec | Technical Reference | Document Type<br>Part Drawing | | Part Number<br>12 |
| Legal Owner | DEMec<br>CETRIB<br>João M.A. Pinto | Title<br>Hybrid Polymer Gear Tooth Support | | Sheet 1/1 |

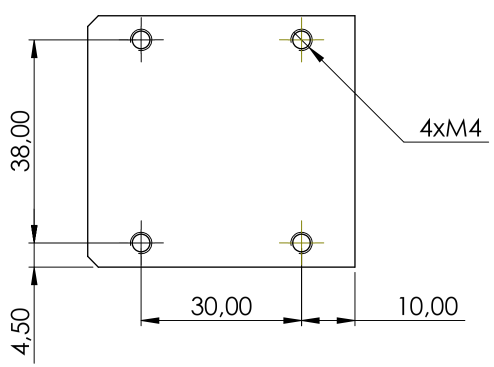

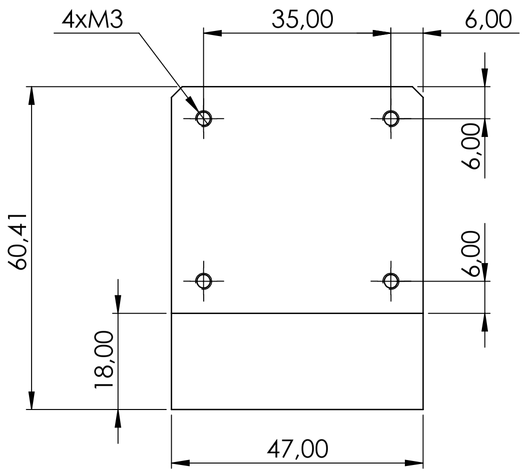

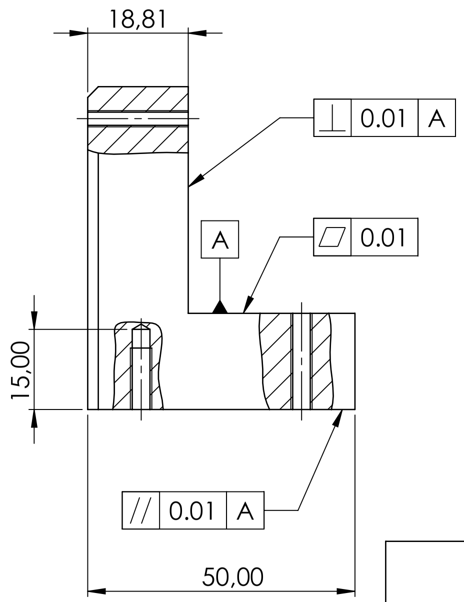

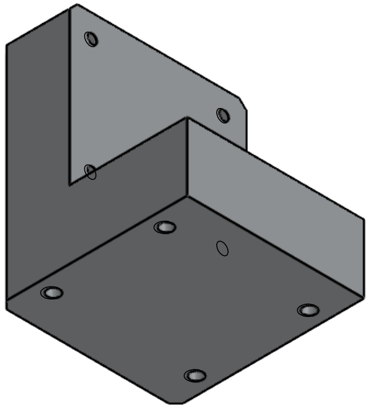

| | | | | |
|---|---|---|---|---|
| Scale<br>1:1 | Geometrical Product Specifications ISO 8015<br>General Geometrical Tolerances ISO 2768-fH<br>ISO 13920<br>Surface Texture ISO 1302<br>Edges and Chamfers ISO 13715 | | Material:<br>6061 Alloy<br>Weight:211.83 g | |
| | Date | Name | | |
| Drawn | 07/04/2022 | João M.A. Pinto | | |
| Checked | 07/04/2022 | Carlos M.C.G. Fernandes | Paper Size<br>A3 | |
| Standard | | | | |
| Responsible Dept.<br>DEMec | Technical Reference | Document Type<br>Part Drawing | Part Number<br>14 | |
| Legal Owner | DEMec<br>CETRIB<br>João M.A. Pinto | Title<br>Hybrid Polymer Gear Tooth Base | Sheet 1/1 | |

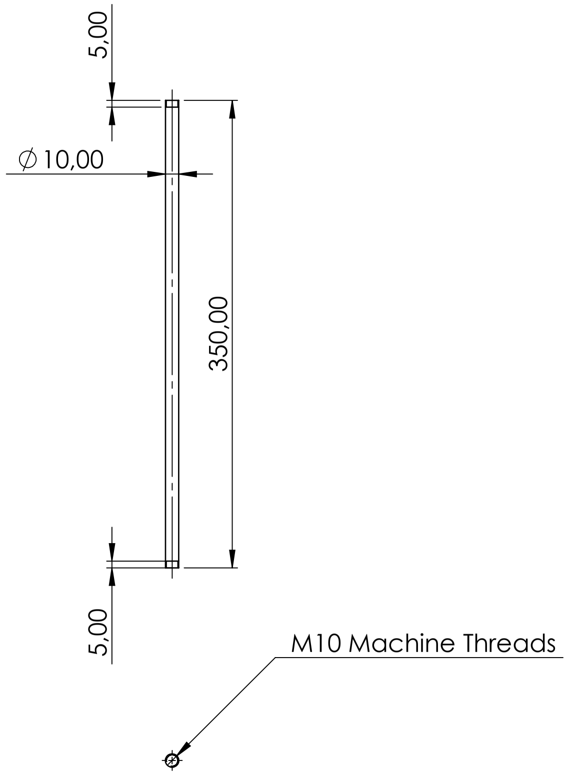

| | | | |
|---|---|---|---|
| Scale<br>1:4 | Geometrical Product Specifications ISO 8015<br>General Geometrical Tolerances ISO 2768-fH<br>ISO 13920<br>Surface Texture ISO 1302<br>Edges and Chamfers ISO 13715 | | Material:<br>AISI 316 Stainless<br>Steel Sheet (SS)<br>Weight:219.91 g |
| | Date | Name | |
| Drawn | 07/04/2022 | João M.A. Pinto | |
| Checked | 07/04/2022 | Carlos M.C.G. Fernandes | Paper Size<br>A3 |
| Standard | | | |

| | | | |
|---|---|---|---|
| Responsible Dept.<br>DEMec | Technical Reference | Document Type<br>Part Drawing | Part Number<br>16 |
| Legal Owner | DEMec<br>CETRIB<br>João M.A. Pinto | Title<br>Shaft | Sheet 1/1 |

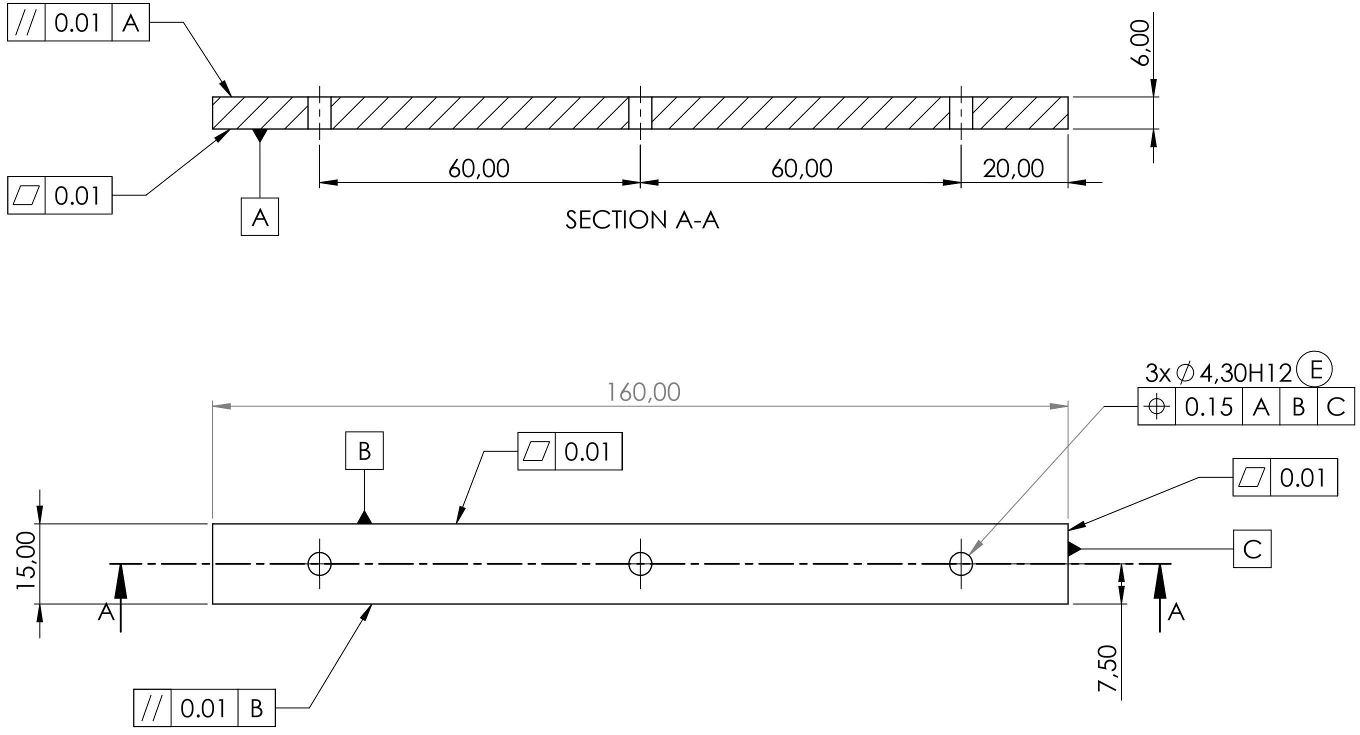

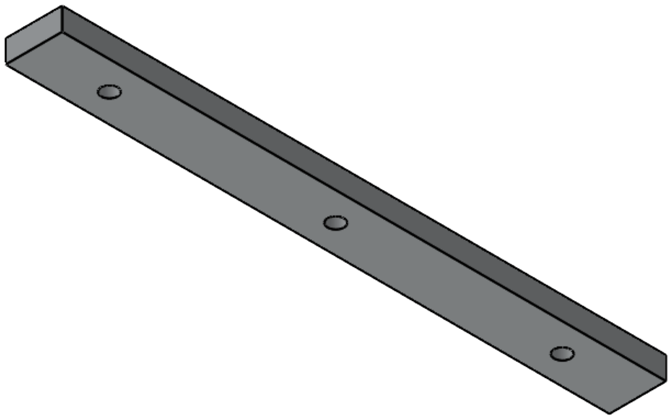

| | | | | |
|---|---|---|---|---|
| Scale<br>1:1 | Geometrical Product Specifications ISO 8015<br>General Geometrical Tolerances ISO 2768-fH<br>ISO 13920<br>Surface Texture ISO 1302<br>Edges and Chamfers ISO 13715 | | Material:<br>6061 Alloy<br>Weight:38.17 g | |
| | Date | Name | | |
| Drawn | 07/04/2022 | João M.A. Pinto | | |
| Checked | 07/04/2022 | Carlos M.C.G. Fernandes | Paper Size<br>A3 | |
| Standard | | | | |
| Responsible Dept.<br>DEMec | Technical Reference | Document Type<br>Part Drawing | Part Number<br>19 | |
| Legal Owner | DEMec<br>CETRIB<br>João M.A. Pinto | Title<br>Horizontal Linear Guide Support | Sheet 1/1 | |

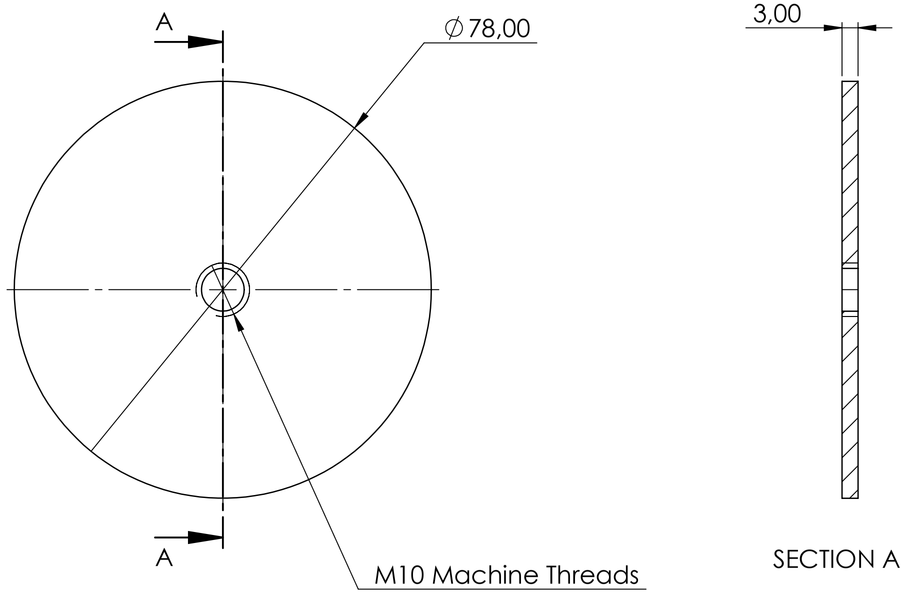

SECTION A-A

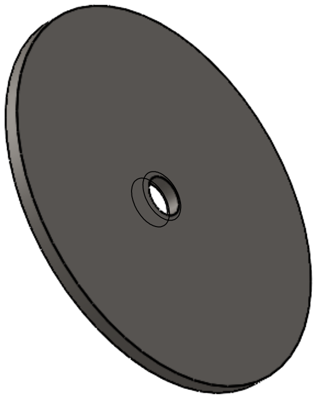

| | | | |
|---|---|---|---|
| Scale<br>1:1 | Geometrical Product Specifications ISO 8015<br>General Geometrical Tolerances ISO 2768-fH<br>ISO 13920<br>Surface Texture ISO 1302<br>Edges and Chamfers ISO 13715 | | Material:<br>AISI 316 Stainless Steel Sheet (SS)<br>Weight:113.47 g |
| | Date | Name | |
| Drawn | 07/04/2022 | João M.A. Pinto | |
| Checked | 07/04/2022 | Carlos M.C.G. Fernandes | Paper Size<br>A3 |
| Standard | | | |
| Responsible Dept.<br>DEMec | Technical Reference | Document Type<br>Part Drawing | Part Number<br>25 |
| Legal Owner | DEMec<br>CETRIB<br>João M.A. Pinto | Title<br>Weight Support Plate | Sheet 1/1 |

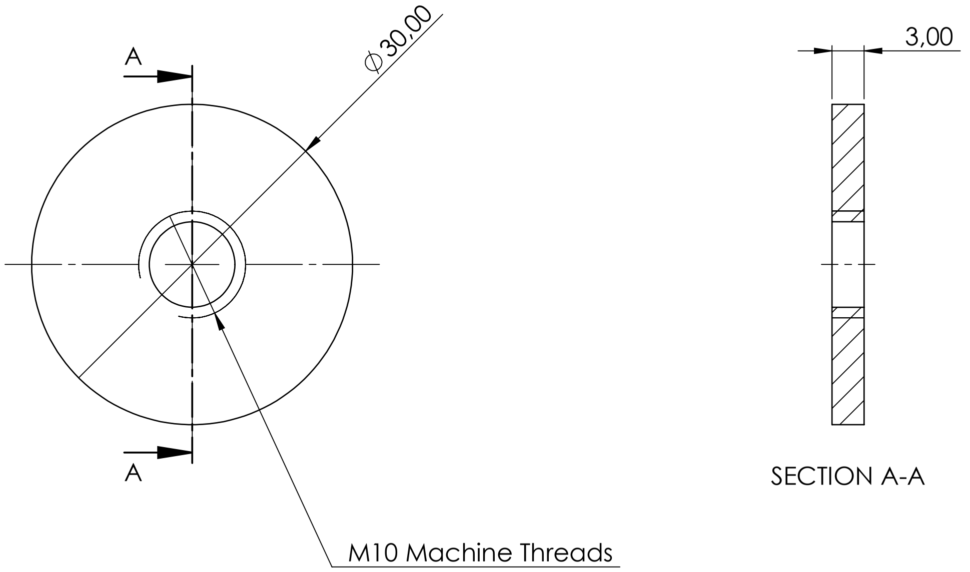

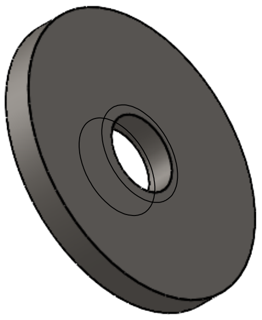

| | | | |
|---|---|---|---|
| Scale<br>2:1 | Geometrical Product Specifications ISO 8015<br>General Geometrical Tolerances ISO 2768-fH<br>ISO 13920<br>Surface Texture ISO 1302<br>Edges and Chamfers ISO 13715 | | Material:<br>AISI 316 Stainless<br>Steel Sheet (SS)<br>Weight:15.76 g |
| | Date | Name | |
| Drawn | 07/04/2022 | João M.A. Pinto | |
| Checked | 07/04/2022 | Carlos M.C.G. Fernandes | Paper Size<br>A3 |
| Standard | | | |

| | | | |
|---|---|---|---|
| Responsible Dept.<br>DEMec | Technical Reference | Document Type<br>Part Drawing | Part Number<br>27 |
| Legal Owner | DEMec<br>CETRIB<br>João M.A. Pinto | Title<br>Support Circular Plate | Sheet 1/1 |

| TAG | X LOC | Y LOC | SIZE |
|---|---|---|---|
| A1 | 1,20 | 1,73 | ∅0,60↧0,50 |
| A2 | 17,28 | 15,23 | ∅0,60↧0,50 |
| A3 | 18,92 | 19,73 | ∅0,60↧0,50 |
| A4 | 20,34 | 23,63 | ∅0,60↧0,50 |
| A5 | 21,21 | 10,73 | ∅0,60↧0,50 |
| A6 | 21,21 | 15,23 | ∅0,60↧0,50 |
| A7 | 21,21 | 19,73 | ∅0,60↧0,50 |
| A8 | 22,07 | 23,63 | ∅0,60↧0,50 |
| A9 | 23,49 | 19,73 | ∅0,60↧0,50 |
| A10 | 25,13 | 15,23 | ∅0,60↧0,50 |
| A11 | 41,21 | 1,73 | ∅0,60↧0,50 |

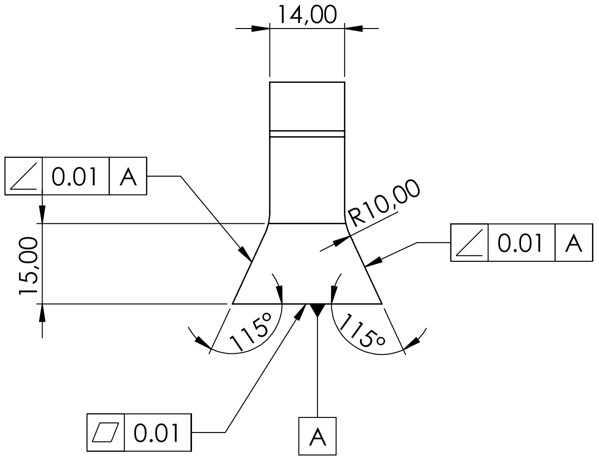

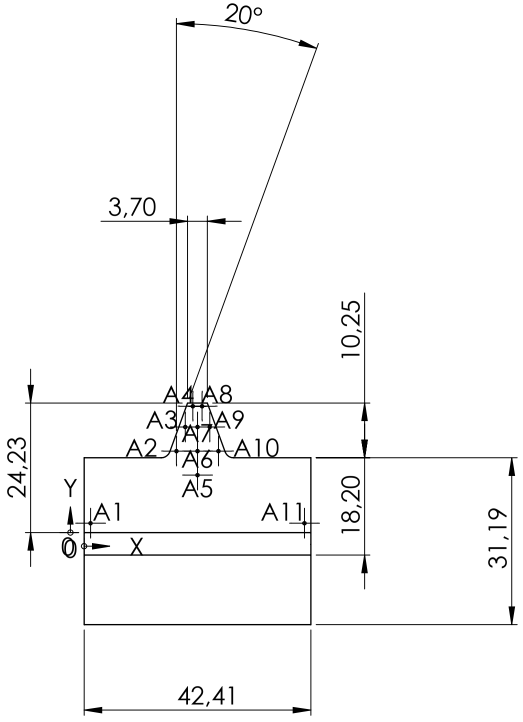

| Geometry | |
|---|---|
| Normal Module [mm], m | 4,5 |
| Normal Pressure angle, α | 2,0 |
| Root Radius Coefficient, rr | 0,38 |
| Fillet Radius [mm], rf=rr x m | 1,71 |

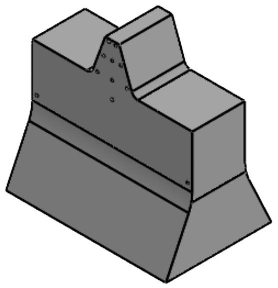

| | | | |
|---|---|---|---|
| Scale<br>1:1 | Geometrical Product Specifications ISO 8015<br>General Geometrical Tolerances ISO 2768-fH<br>ISO 13920<br>Surface Texture ISO 1302<br>Edges and Chamfers ISO 13715 | | Material:<br>POM Acetal<br>Copolymer<br><br>Weight:33,46 g |
| | Date | Name | |
| Drawn | 07/04/2022 | João M.A. Pinto | |
| Checked | 07/04/2022 | Carlos M.C.G. Fernandes | Paper Size<br>A3 |
| Standard | | | |

| | | | |
|---|---|---|---|
| Responsible Dept.<br>DEMec | Technical Reference | Document Type<br>Part Drawing | Part Number<br>11 |
| Legal Owner | DEMec<br>CETRIB<br>João M.A. Pinto | Title<br>Polymer Gear Tooth | Sheet 1/1 |

# Appendix B

# Thermal Results Evolution for the Points in Study

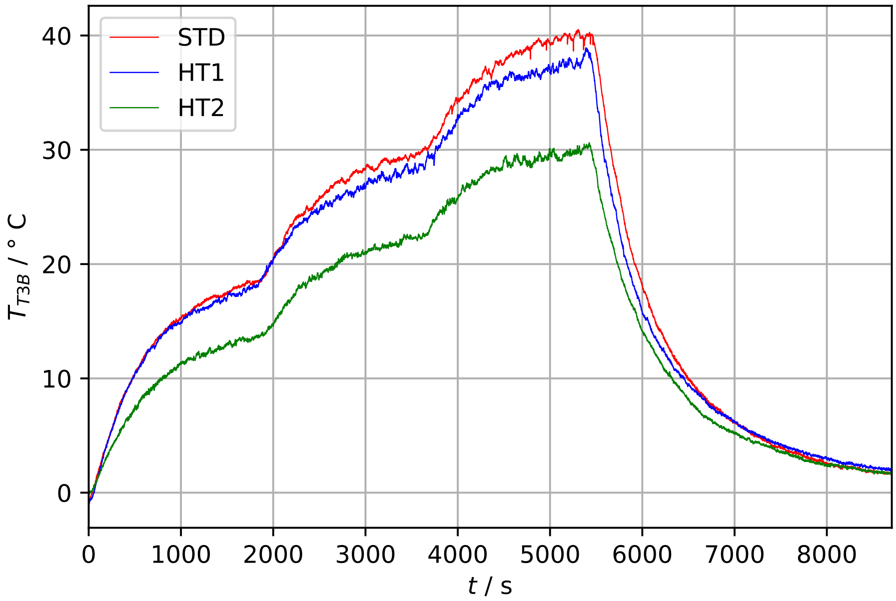

Figure B.1: Stabilized temperature evolution during the entire thermal test for point T3B.

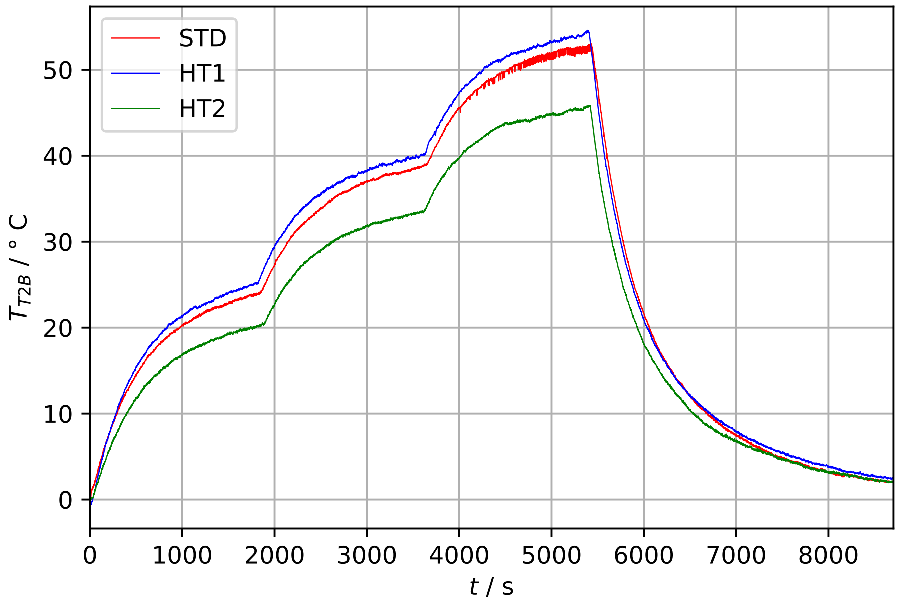

Figure B.2: Stabilized temperature evolution during the entire thermal test for point T2B.

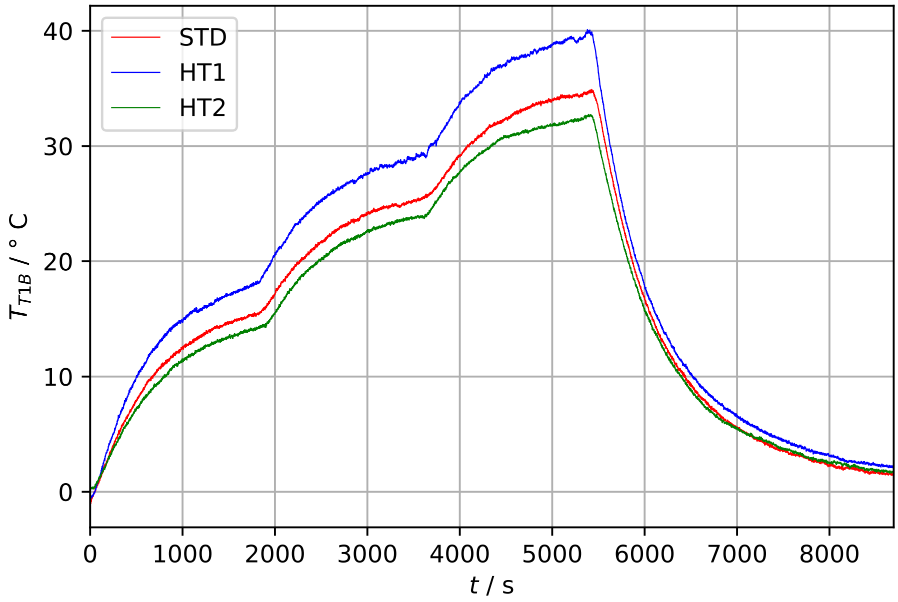

Figure B.3: Stabilized temperature evolution during the entire thermal test for point T1B.

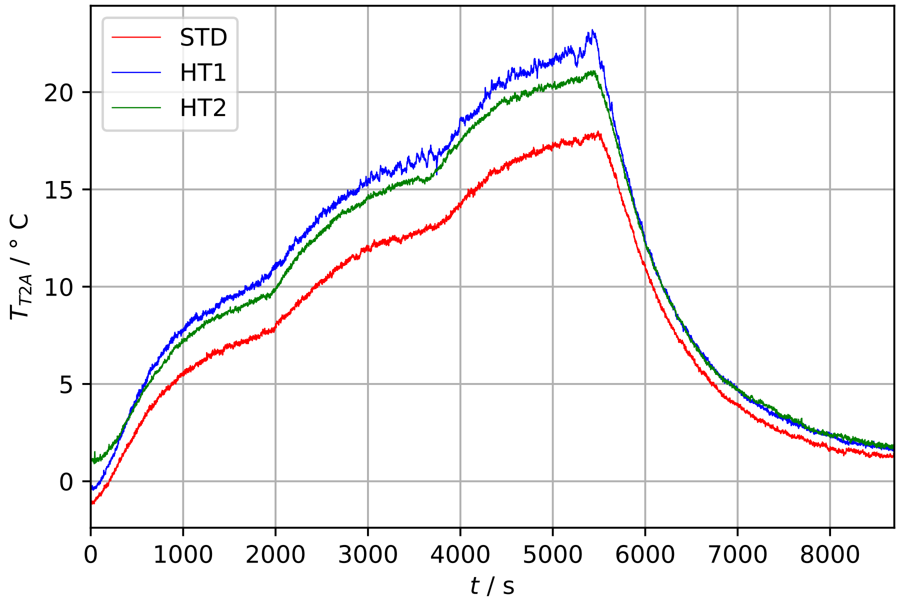

Figure B.4: Stabilized temperature evolution during the entire thermal test for point T2A.

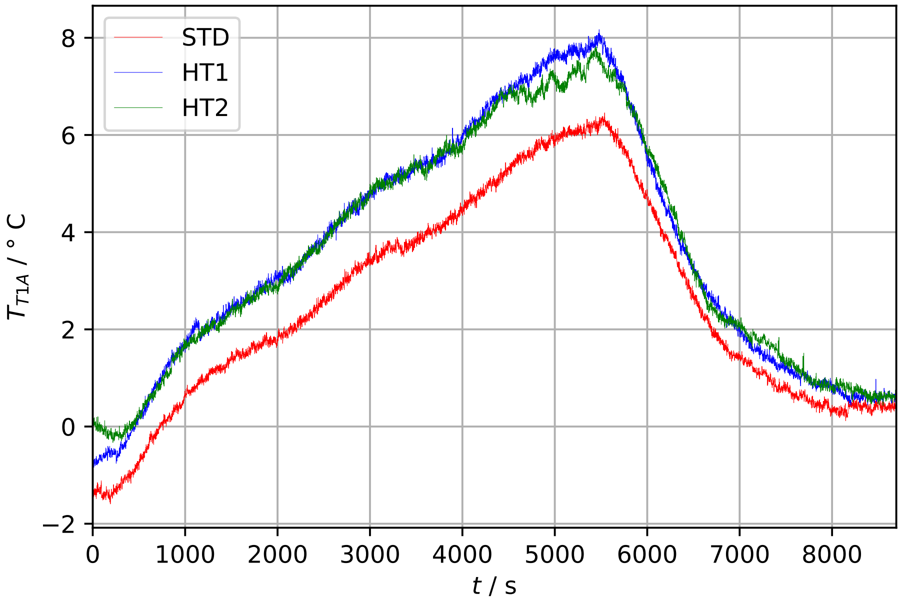

Figure B.5: Stabilized temperature evolution during the entire thermal test for point T1A.